Cone packing measurements from confocal and split-detector adaptive optics images in human eyes

By

Suman Adhikari

A dissertation submitted to the Physiological Optics and
Vision Sciences Graduate Program
College of Optometry
in partial fulfillment of the requirements for the degree of

DOCTOR OF PHILOSOPHY

in Physiological Optics

Chair of Committee: Jason Porter, Ph.D.

Committee Member: Laura J Frishman, Ph.D.

Committee Member: Nimesh Patel, OD, Ph.D.

Committee Member: Joseph Carroll, Ph.D.

University of Houston
August 2020

DEDICATION

This dissertation is whole-heartedly dedicated to my parents who were always a constant source of inspiration for me throughout, to my brother for his motivation and my wife for her support.

ACKNOWLEDGMENTS

First of all, I would like to thank Dr. Jason Porter for accepting me in his team and allowing me to work in his lab. I acknowledge him for his immense support and guidance in all my projects. I am thankful to him for all the guidance on writing proposals we submitted. His valuable comments and suggestions on my presentations have always helped me learn. I would also like to thank my other committee members: Dr. Frishman, Dr. Patel and Dr. Carroll for being very helpful in reviewing all the documents related to my projects. I am thankful to them for their helpful discussion and guidance to my projects in all the formal/informal meetings we've had over time.

I would like to thank Dr. Alex Schill for all his guidance in running the AO system, right from how to turn the system on safely, maintenance of the system, hands-on training on acquiring data, and much more. I would like to thank Hope for helping me with the codes for the simulated cones. I also thank her for helping me understand all other MATLAB and Python programs we use in the lab. Her valuable comments on all my writings and presentations always helped me.

I would not be able to acknowledge Hanieh, Gwen and Jakaria enough for their constant encouragement and support. Also, thanks to their help with the data collection and helpful discussion on the analysis. I am thankful to my batch mates, Ashutosh, Gareth, Laura, Mythri and Suraj for their friendship and making this long journey so wonderful. I am also thankful to all the senior and junior graduate students with whom I have spent many quality times.

I would like to acknowledge all the faculty members for their teachings in the core classes and modules, for all the helpful discussions in the seminar presentations and other

group discussions. Finally, I would also like to thank the library department, business office, graduate office and everyone who helped me and the projects directly and indirectly.

ABSTRACT

Purpose: Adaptive optics scanning laser ophthalmoscope (AOSLO) imaging has been used to calculate metrics of cone packing in healthy and diseased eyes. However, there is a lack of data comparing metric values obtained using different AOSLO imaging modalities, as well as the impact of different image analysis methods on these metrics. Here, we 1) calculate the longitudinal repeatability of confocal and split-detector AOSLO imaging, 2) compare cone density measurements made using different marking techniques, and 3) compare cone metrics calculated using different region of interest (ROI) sizes.

Methods: AOSLO imaging was performed in 10 healthy individuals from the foveal center to 10° in 4 major meridians at baseline and after 12 months. Cone metrics were quantified from confocal and split-detector images over the same retinal patches and compared. Next, cones extracted from simulated and in vivo images from 5 healthy subjects were marked using different techniques. Cone densities were calculated and compared with known densities for simulated data. Coefficients of variation (CVs) were calculated for in vivo data. Finally, square ROIs of different sizes were extracted from simulated and in vivo cone mosaics. Cone metrics were compared between ROI sizes.

Results: 1) The mean CVs of density for confocal and split-detector images were 8.4% and 6.2%, respectively. 2) Unbound densities when marking all cones fully inside and partially along the ROI borders were significantly greater ($P<0.05$) than bound densities. CVs for bound densities tended to be smaller than for unbound densities. 3) CVs for small ROIs were greater across all eccentricities and increased with increasing eccentricity for in vivo data. In simulated data, ROIs of 25µm x 25µm yielded values that were significantly lower than all larger ROI sizes and were closest to simulated values near the foveal center.

Conclusions: The intersession repeatability data in healthy human eyes may be used in future longitudinal studies examining diseased eyes. Computing bound cone density provides measurements with greatest accuracy and least variability. For eccentricities close to the fovea, a 25µm x 25µm ROI size provides measurements with greatest accuracy while larger ROI sizes provide lower variability in the periphery.

TABLE OF CONTENTS

LIST OF TABLES

LIST OF FIGURES

CHAPTER 1

General Introduction

1.1 Introduction

Many studies have calculated metrics describing the geometry of the cone mosaic (e.g., density, spacing, regularity) in healthy and diseased eyes from *in vivo* images (Chui et al., 2008; Genead et al., 2011; Randerson et al., 2015). While these studies have provided valuable information, there is a general lack of data that compares metric values obtained using different imaging modalities, as well as the impact of different image processing and analysis methods on these metrics. Consequently, it is challenging to compare measurements obtained using different techniques across studies. The overall goals of this project are to determine the repeatability of quantifying different cone photoreceptor packing metrics and to determine whether optimal procedures exist for quantifying cone photoreceptor packing in healthy eyes.

1.2 Structure and function of the human retina

The retina is a thin, delicate, semi-transparent neural tissue that lines the innermost layer of the eyeball. The main structures visible in the retina when viewed through a direct ophthalmoscope are the optic disc, fovea, and blood vessels (Figure 1-1).

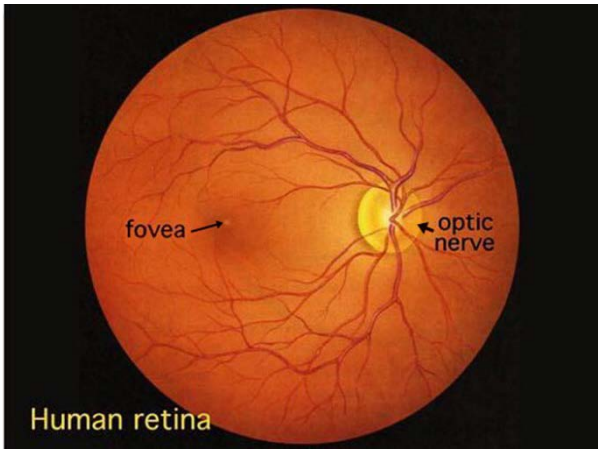

Figure 1-1. Ophthalmoscopic view of the human retina showing the optic nerve, fovea, and blood vessels. (Credit: Webvision, http://webvision.med.utah.edu/)

The optic nerve is the cranial nerve that transmits information from the retina to the brain. Slightly temporal to the optic nerve is the fovea, which is the central portion of the retina. The fovea is an indented region inside a densely pigmented area (called the macula) and is composed of multiple cell types (Figure 1-2).

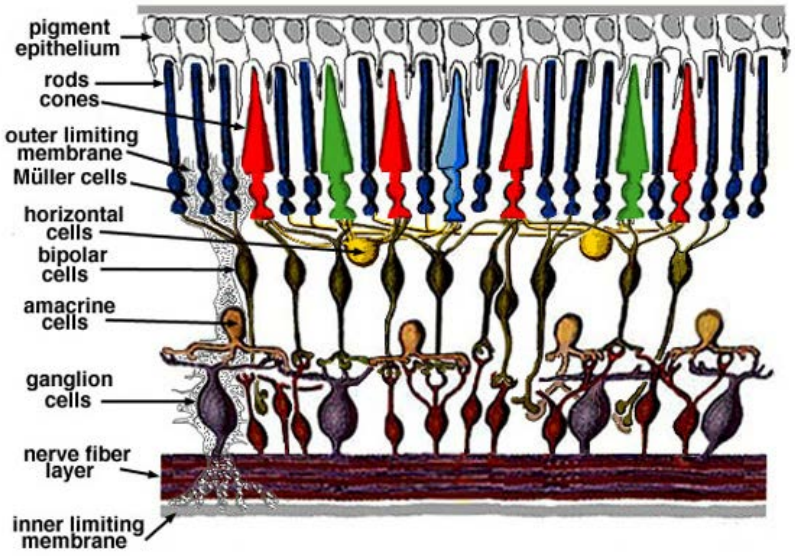

Figure 1-2. Schematic diagram of different cells in the retina and their connections. Light travels through the cornea and lens where it is incident on the anterior retina (at the bottom of the diagram). Light travels through multiple layers and cell types before it is absorbed by rod and cone photoreceptors in the outer retina (at the top of the picture). Signals are then fed forward through the retina to the nerve fiber layer where they exit the eye through the optic nerve. (Credit: Webvision, http://webvision.med.utah.edu/)

Light from the outside world travels through the pupil and propagates through all layers of the retina to reach the rods and cones, where it is absorbed and initiates the neural signal. The photoreceptors contact the bipolar cells and horizontal cells at the outer plexiform layer. The bipolar cells then relay signals to the ganglion cells and amacrine cells that form the inner plexiform layer. The axons of the ganglion cells form the nerve bundles that exit the eye through the optic nerve and transmit visual signals to the brain.

1.2.1 Photoreceptor structure and function in the healthy eye

Rods and cones constitute the photoreceptor layer of the human retina and received their names from the shape of their outer segments. In addition to outer segments, rods and cones have a connecting cilium, inner segment, nuclear region, axon, and synaptic terminal, as shown in Figure 1-3 below.

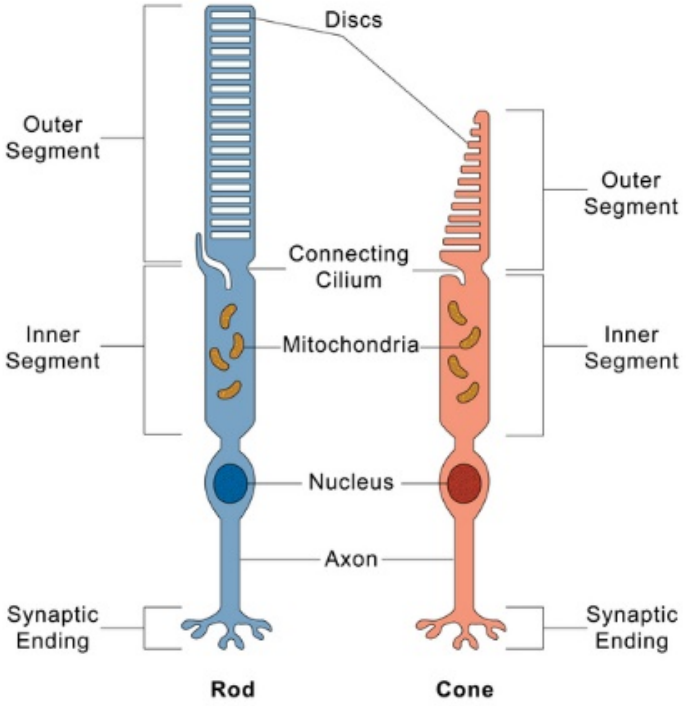

Figure 1-3. A simple schematic of individual rod and cone cells showing their constitutive components, including outer and inner segments, connecting cilia, nucleus, axon, and synaptic pedicle. (Image Credit: Mr. High Sky/Shutterstock.com)

Outer segments are the primary sites for capturing light and converting it into electric signals through a process called phototransduction. The connecting cilium is the major cytoskeletal structure for mature photoreceptors and connects the outer segment to the inner segment. The inner segment contains cell organelles, such as mitochondria, endoplasmic reticulum, etc. Synaptic terminals are the end structures that are involved in the transfer of neurotransmitters with other layers of cells, such as bipolar cells and horizontal cells. There is a continuous degeneration and regeneration of outer segments in rods and cones. The

degenerated outer segment tips are engulfed by the retinal pigment epithelium layer and new discs are added at the bases of the outer segments. Rods have thinner and longer outer segments compared to cones, except toward the foveal center. There are no rods within a small region at the central fovea (the foveola) and the cones there are slim and elongated.

Rods contain rhodopsin as their visual pigment, with a peak sensitivity at 500 nm. Rods are more sensitive than cones and can even detect a single photon of light (Baylor et al., 1979). Cones contain cone opsins as their visual pigment. There are 3 different classes of cones depending upon which opsin molecule they contain: long-wavelength sensitive cones (L cones, 560 nm peak sensitivity), medium-wavelength sensitive cones (M cones, 530 nm peak sensitivity), and short-wavelength sensitive cones (S cones, 420 nm peak sensitivity). The color opponent process between the 3 different classes of cones provides human eyes with trichromatic color vision (Baden & Osorio, 2019).

1.3 Distribution of photoreceptors in the human retina

Overall, there are 92 million rods and 4.6 million cones in an average human retina (Curcio et al., 1990). Cone photoreceptor density peaks at the foveal center, with an average value of 199,000 cones/mm^2 (range: 100,000–324,000 cones/mm^2) (Curcio et al., 1990), and decreases sharply with increasing eccentricity before leveling off at an eccentricity of 10-15° (Figure 1-4). Conversely, rod photoreceptors are absent at the very center of the fovea and increase to reach an average peak density of 176,200 rods/mm^2 (range: 158,000–189,000 rods/mm^2) at an eccentricity of approximately 20-25° (Wells-Gray et al., 2016).

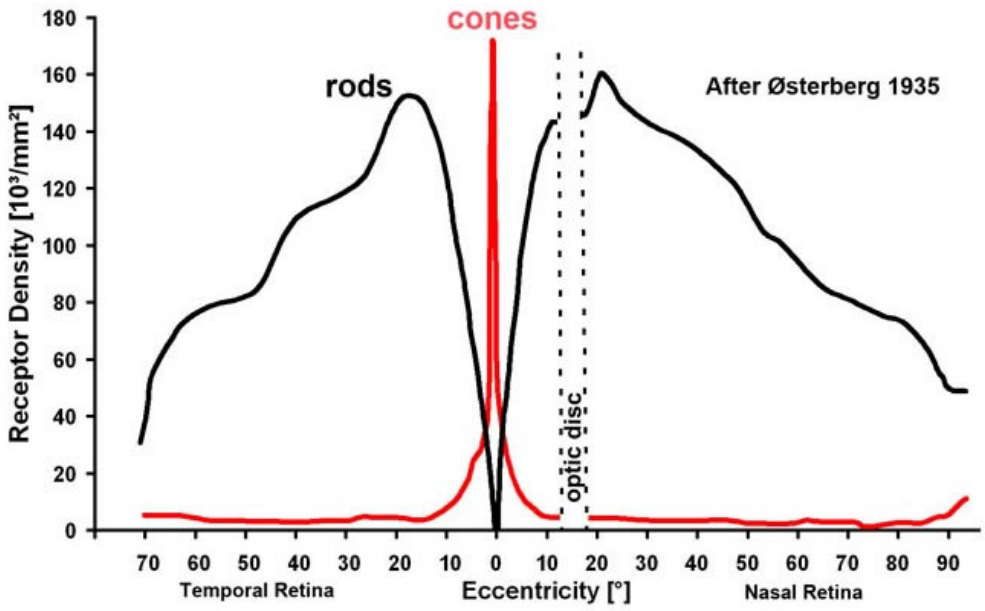

Figure 1-4. Change in the density of rods (black line) and cones (red line) with eccentricity in the temporal and nasal retina (Credit: Webvision, http://webvision.med.utah.edu/) (Osterberg, 1935).

Photoreceptor density has been shown to vary with meridian. At the same eccentricity, histological data has shown that cone density is 40-45% higher in the nasal retina compared to the temporal retina (Curcio et al., 1990). Density is also slightly higher in the inferior meridian compared to the superior meridian for more mid-peripheral eccentricities (Curcio et al., 1990). *In vivo* studies have confirmed histological measurements reporting higher values of cone density in the horizontal versus the vertical median (with differences ranging from 9 – 13%) (Chui et al., 2008; Feng et al., 2015; Song et al., 2011; Supriya et al., 2015). Somewhat similarly, rod density is higher in the superior and nasal meridians compared to the inferior and temporal meridians (Curcio et al., 1990). *In vivo* data on the distribution of rods are also consistent with histological findings (Dubra et al., 2011; Merino et al., 2011; Wells-Gray et al., 2016).

Previous studies have also reported a strong correlation between cone density and axial length. Chui et al. (2012) found a significant decrease in linear cone density (cones/mm^2) with increasing axial length at an eccentricity of 1 mm, and an increase in angular cone density

(cones/deg^2) with increasing axial length at an eccentricity of 3 mm. Building on an earlier study by Li et al. (2010), Wang et al. (2019) also observed significant decrease in linear cone density (cones/mm^2) and significant increase in angular cone density (cones/deg^2) with increase in axial length at closer eccentricities (Figure 1-5).

Few studies have looked at the effect of age on measures of cone density. Studies that have examined this topic report mixed results. A histological study by Panda-Jonas et al. (1995) and an *in vivo* study by Song et al. (2011) have reported significant differences in the cone density between different age groups. Song et al. (2011) showed that older subjects (50-65 years) had approximately 75% of the cone density found in younger subjects (22-35 years) at an eccentricity of 0.18 mm. Differences in density between these two age groups decreased with increasing eccentricity. Conversely, a handful of studies have found no significant differences in cone density between groups of subjects with different ages (Curcio et al., 1993; Jacob et al., 2017; Park et al., 2013).

1.4 Adaptive optics imaging

The roots of adaptive optics (AO) are grounded in the field of astronomy, for which the idea was originally introduced to allow ground-based astronomical telescopes to correct for aberrations introduced by atmospheric turbulence and distortions (Beckers, 1993). Since its first application for imaging the living human eye in a flood-illuminated system (Liang et al., 1997), AO has since been combined with multiple imaging modalities, including scanning laser ophthalmoscopes (SLOs) and optical coherence tomography (OCT), to study different ocular structures *in vivo* (e.g., cone photoreceptors, retinal nerve fiber layer, vasculature, lamina cribrosa, retinal pigment epithelium, ganglion cells) (Chui et al., 2012; Morgan et al., 2014; Rossi et al., 2017; Takayama et al., 2013; Vilupuru et al., 2007).

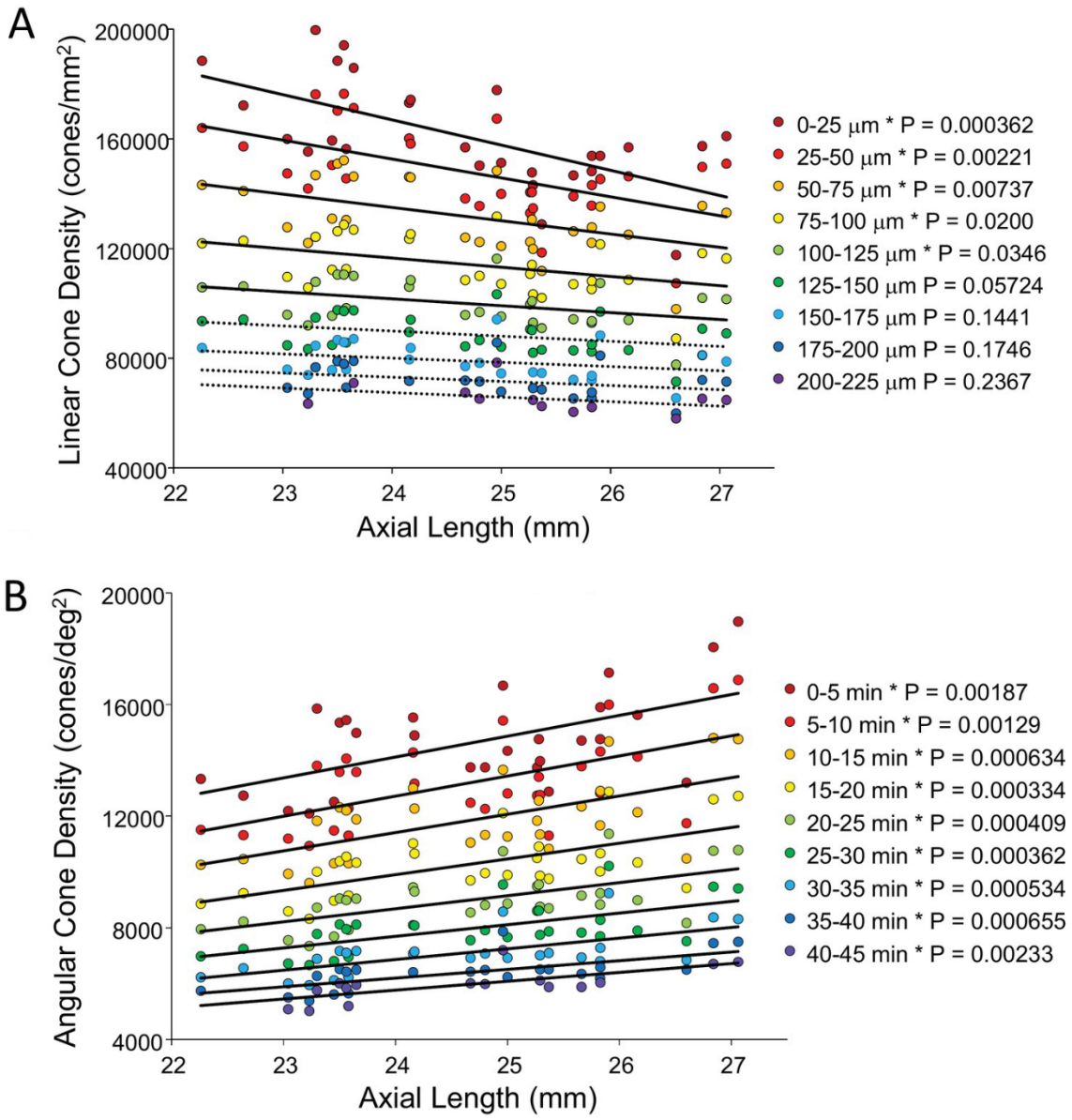

Figure 1-5. Change in cone density as a function of axial length. Different colored circles represent measurements taken at different retinal eccentricities from the foveal center in terms of (A) physical and (B) angular distances. (A) Linear cone density decreases with increasing axial length for eccentricities of 100-125 μm (light green) and closer to the foveal center. (B) Angular cone density increases with increasing axial length for all examined eccentricities. (* sign in the legend and solid lines in the graph indicate significant relationships; <0.05). Reprinted with permission. (Wang et al., 2019)

1.4.1 Principles of AO

Adaptive optics is used to measure and correct for aberrations that are present in an optical system. The main method that has historically been used to measure aberrations in the human eye is the Shack-Hartmann wavefront sensor (SHWS) (Liang et al., 1994; Liang et al., 1997). A SHWS consists of an array of very small, regularly spaced lenses (called a lenslet array) that is followed by an imaging sensor placed at the back focal length of the lenslets. When an unaberrated planar wavefront is incident on the lenslet array, each lens focuses a small portion of the wavefront to a spot along the lens' optical axis (Figure 1-6a). However, if the wavefront is aberrated, the focused spots will not lie on-axis, but will be displaced by an amount that is proportional to the local slope of the wavefront in front of the given lenslet (Figure 1-6b). The SHWS uses all of the spot displacements to calculate the total wavefront phase information (i.e., the shape of the aberrated wavefront). Once the shape of the wavefront error is known, commands can be sent to a deformable mirror to alter its shape such that the reflected wavefront is planar (Figure 1-7).

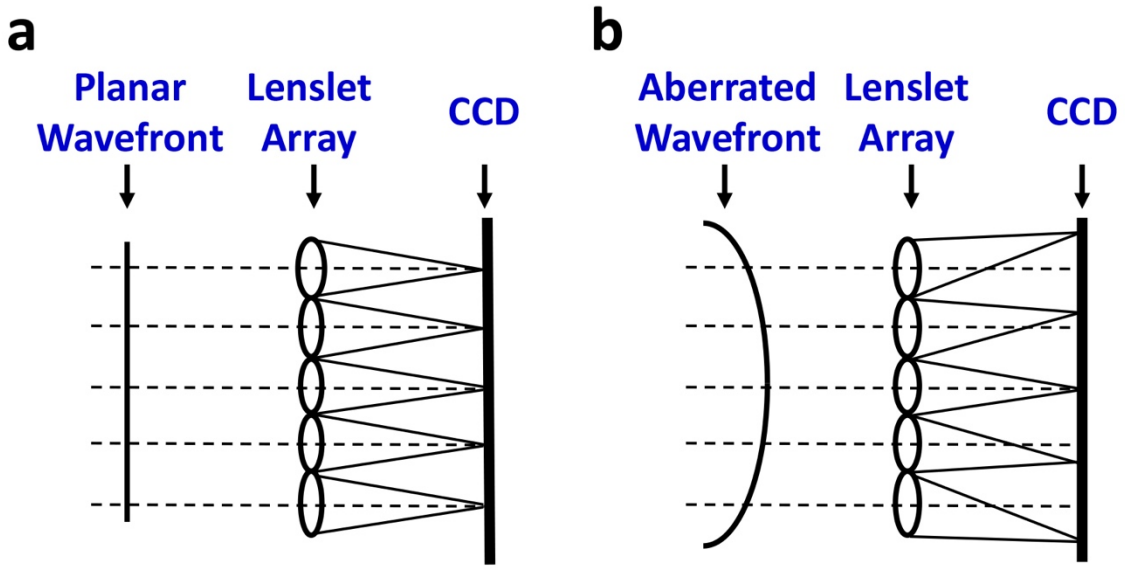

Figure 1-6. Shack-Hartmann wavefront sensor principle. (a) A planar wavefront incident on a lenslet array produces focused spots on-axis on the CCD camera. (b) An aberrated wavefront incident on the lenslet arrays causes spots to be deviated from their ideal on-axis focusing position.

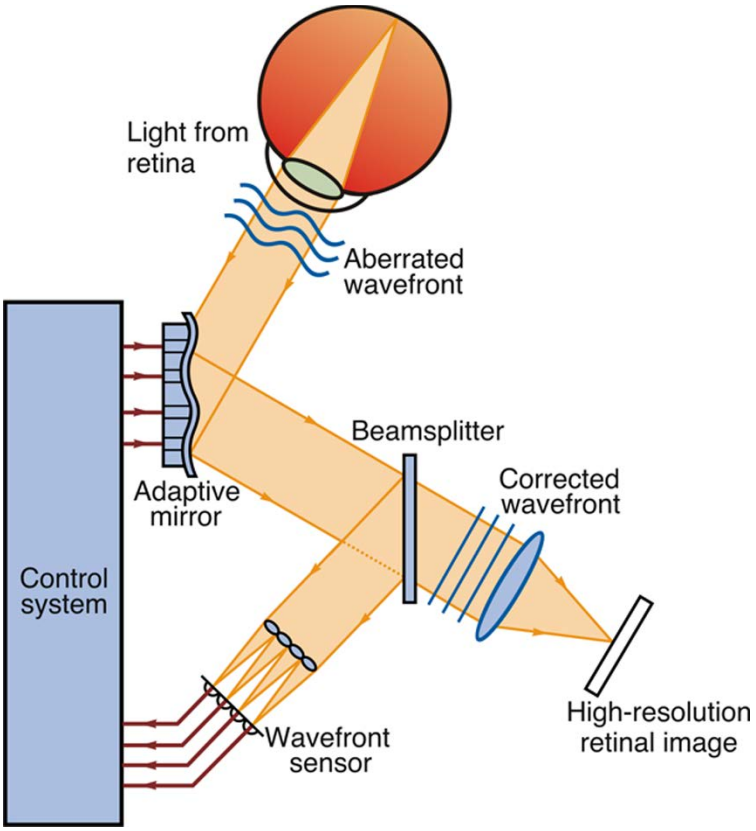

Figure 1-7. Schematic of the basic components of an adaptive optics system designed to image the human eye, including an adaptive (or deformable) mirror, a wavefront sensor, and an imaging path (Reprinted with permission from Chris Dainty, National University of Ireland, Galway).

1.4.2 In vivo adaptive optics (AO) imaging of photoreceptors

One of the primary uses of AO technology has been to visualize photoreceptors *in vivo* in healthy and diseased eyes. Liang et al. (1997) demonstrated one of the first images of a healthy human cone photoreceptor mosaic using an adaptive optics flood-illuminated system, shown in Figure 1-8. While the image nicely shows cones as bright spots and was very unique for its time, the image suffers from areas of non-uniform contrast.

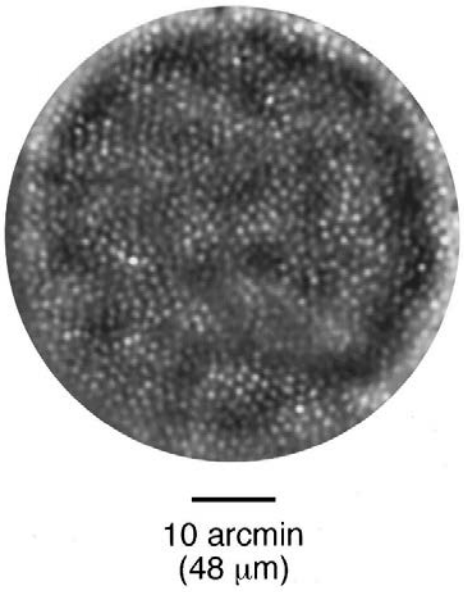

Figure 1-8. *in vivo* image of a human photoreceptor mosaic captured using an AO flood-illuminated system by the Williams Lab at the University of Rochester (Liang et al., 1997). Reprinted with permission.

In 2002, Roorda et al. (2002) combined AO with a confocal scanning laser ophthalmoscope (SLO) to create an adaptive optics scanning laser ophthalmoscope that was capable of acquiring real-time images of cone photoreceptors (Chui et al., 2008), rod photoreceptors (Dubra et al., 2011), retinal vasculature (including the flow of individual blood cells) (Tam et al., 2010), and nerve fiber bundles (Takayama et al., 2013). AOSLO imaging provides many advantages compared to the use of an AO flood-illuminated system. For example, AOSLOs record movies at video rates and traditionally use a confocal pinhole to increase the contrast of the retinal image by blocking light that is scattered from other retinal planes (Figure 1-9).

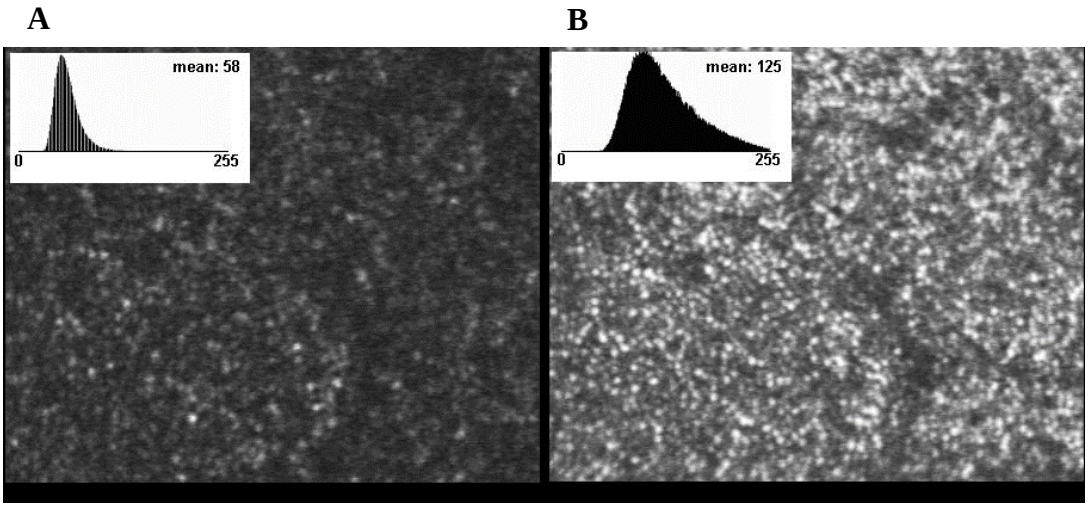

Figure 1-9. Image of a healthy human cone photoreceptor mosaic captured using an AOSLO by Roorda et al. (2002). (A) A registered and average image obtained prior to the correction of higher order aberrations using adaptive optics. (B) An image of the same patch of retina as in (A) following the correction of higher order aberrations using a confocal AOSLO. The AOSLO provides images with increased resolution, brightness and contrast. The small insets are displaying the histogram of the contrast in the corresponding images. Reprinted with permission.

1.4.3 Confocal AO imaging

A confocal imaging system places a confocal pinhole in a position that is optically conjugate with the retinal plane being imaged, thereby allowing only the light that is directed back-scattered from the layer of interest to pass through the pinhole and reach the detector (Figure 1-10). The pinhole also serves to directly block light that is multiply scattered from other retinal layers. These properties serve to not only increase the contrast of retinal images, but also provide increased optical sectioning capabilities to the system.

With the use of improved light sources and post-processing techniques, confocal AOSLOs have more recently been able to resolve rod photoreceptors to provide additional useful information (Dubra et al., 2011). These improvements have facilitated the examination of photoreceptor structure, types, and distribution in healthy eyes, as well as in diseased eyes (Figure 1-11) (Dubra et al., 2011; Hofer et al., 2005; Miao et al., 2014; Morgan et al., 2014; Park et al., 2013; Scoles et al., 2014; Song et al., 2011; Sun et al., 2016; Tanna et al., 2017).

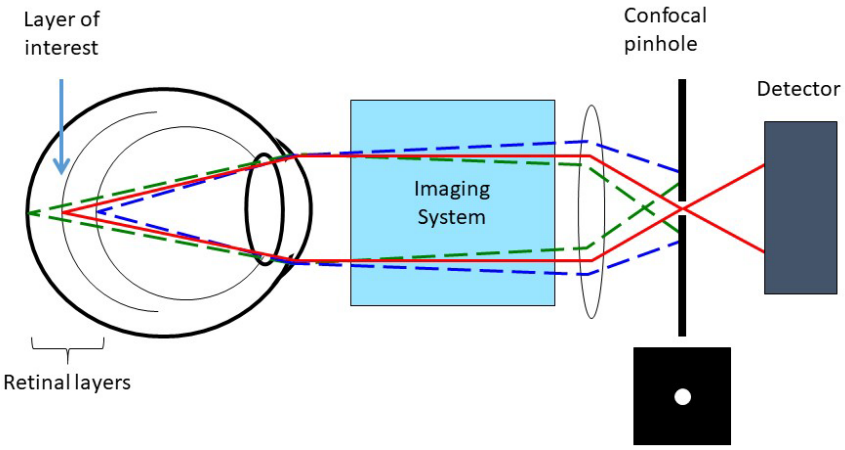

Figure 1-10. A schematic showing the principle of confocal imaging. Only light that is directly backscattered light from the layer of interest (red lines) can pass through the confocal pinhole and reach the detector. Light scattered from layers anterior to (blue lines) and posterior to (green lines) the layer of interest is blocked by the pinhole.

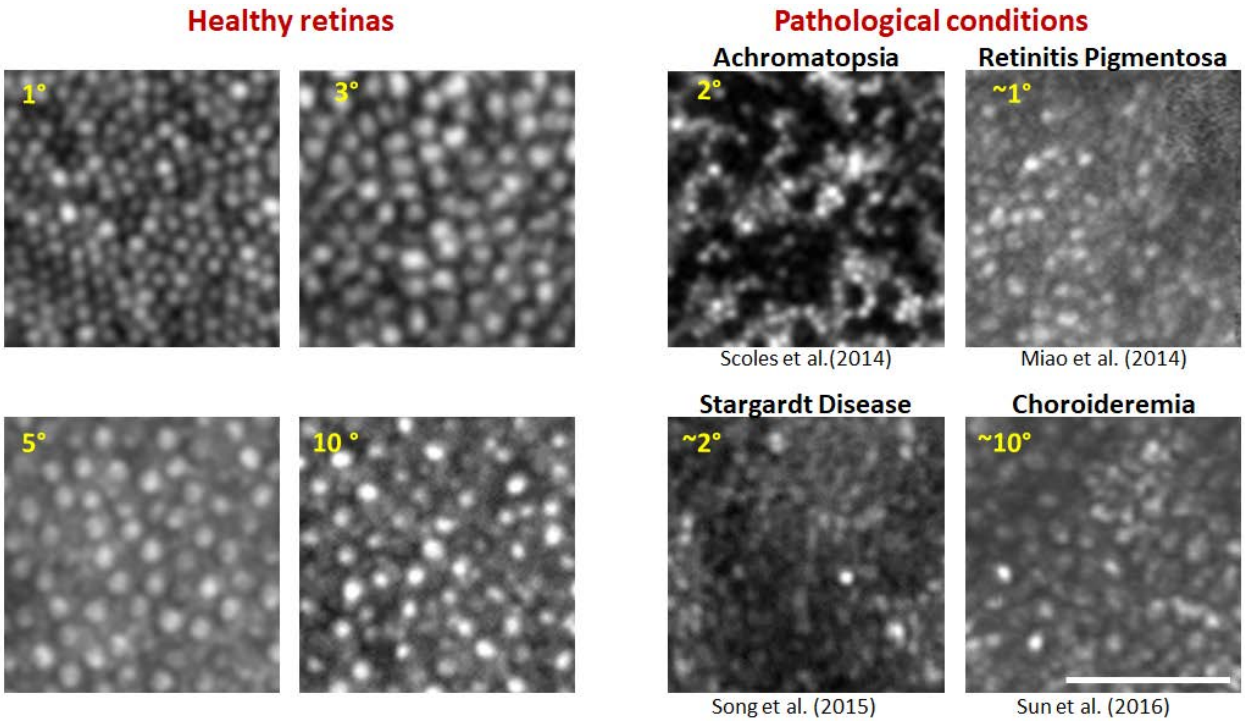

Figure 1-11. Photoreceptor mosaics from healthy and representative diseased eyes at different eccentricities. Scale bar for all images: 50 µm. Reprinted with permission. (Miao et al., 2014; Scoles et al., 2014; Song et al., 2015; Sun et al., 2016)

1.4.4 Challenges of confocal imaging

Confocal imaging is a very useful technique to visualize photoreceptors *in vivo*. However, it is now known that healthy photoreceptors can vary in their brightness over time (Jonnal et al., 2010; Pallikaris et al., 2003; Pircher et al., 2011), sometimes causing healthy cones to appear as dark "holes" in the photoreceptor mosaic, even after performing a logarithmic transform of the image to better visualize lower intensity features (as shown in Figure 1-12).

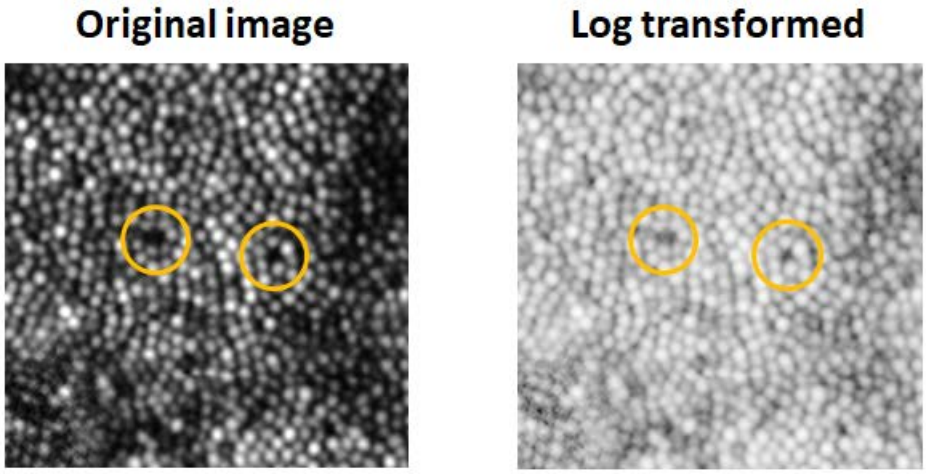

Figure 1-12. Dark "holes" that are present in the original confocal image acquired from a healthy human subject can still appear as dark "holes" after performing a log-transform to enhance lower intensities. These dark locations lead to uncertainties in whether a cone is actually present at the location of the "hole," even within healthy eyes.

The visualization of photoreceptors as bright spots in confocal AOSLO images depends on having (1) inner segments that directionally couple light into outer segments and (2) intact outer segments that allow light to backscatter and interfere (Jonnal et al., 2010). In diseased eyes, the presence of dark "holes" in the mosaic makes it particularly challenging to know whether the "hole" contains a healthy cone whose brightness happens to be reduced at that moment in time, a fragmented or non-healthy cone that does not waveguide as normal, or no cone at all. The presence of dark "holes," even in healthy photoreceptor mosaics, makes it challenging to know whether to mark the dark location as a cone for its quantification.

1.4.5 Split detector AO imaging

Split detector imaging is a recent AOSLO imaging modality introduced by Scoles et al. (2014) that makes use of multiply-scattered light to provide an alternative view of the structure being imaged (relative to traditional confocal imaging). The general principle for split detector imaging is shown in Figure 1-13. In this modality, multiply-scattered light is allowed to pass through to the detector, while the light directly back-scattered from the layer of interest is blocked with an anti-confocal pinhole.

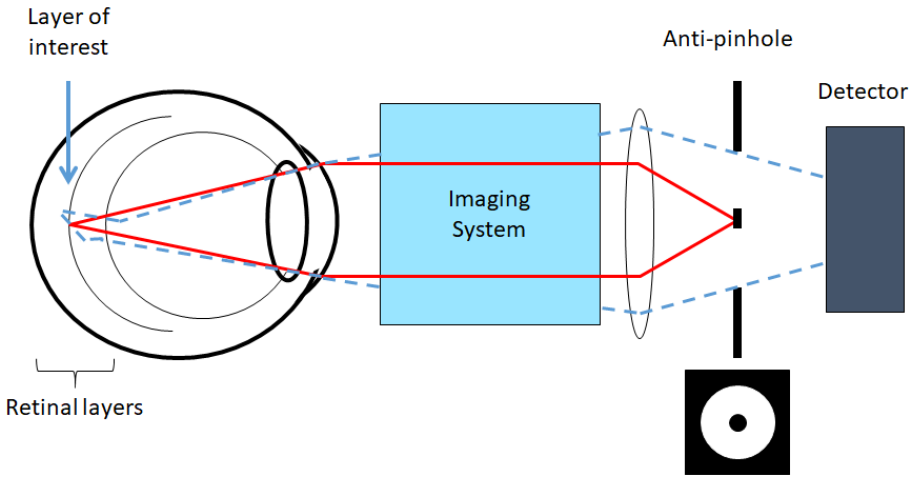

Figure 1-13. A schematic showing the general principle for split-detector imaging. An anti-pinhole is used to block the directly-backscattered light typically sent to the detector in confocal imaging (red lines), while allowed multiply scattered light to pass through a clear annulus region and reach the imaging detector.

Figure 1-14 provides a simplified schematic that shows confocal and split-detector channels in an AOSLO system (Scoles et al., 2014). In this configuration, an annular mirror (with a reflective central portion and a transparent annulus) acts as an anti-pinhole. Light that is directly backscattered from the layer of interest is reflected by the central reflective portion of the annular mirror to the confocal imaging detector (Detector 1). An additional mirror, known as the knife-edge, is used to evenly split the multiply-scattered light that passes through the transparent portion of the annular mirror into two halves that are directed to two different detectors (Detectors 2 and 3). Later, the difference between the signal intensities in the two detectors is divided by their sum to get the split-detector signal.

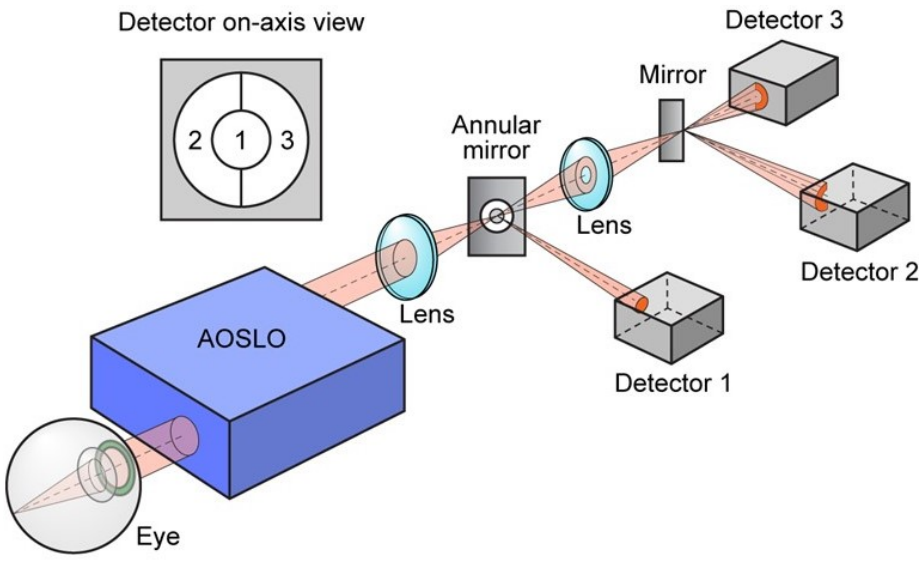

Figure 1-14. Schematic of confocal and split-detector set-up showing different mirrors and detectors (Scoles et al., 2014). For the confocal image, the central light from the beam is reflected by the annular mirror which reaches detector 1 whereas the peripheral light is split up by the special mirror (knife-edge) to detectors 2 and 3 as shown by the inset. Reprinted with permission.

In this arrangement, confocal and split-detector videos of the same patch of retina can be collected simultaneously. An example of confocal and split-detector images from the same retinal locations in a healthy human subject are shown for 2 different eccentricities in Figure 1-15. It is currently believed that the light used to generate split detector images of cone photoreceptors originates from each cone's inner segment. Scoles et al. (2014) found that the sizes of the cones in their split-detector images were comparable to the sizes of cone inner segments imaged *ex vivo* in a separate group of eyes. Moreover, using split detector imaging, it is now possible to more confidently determine whether locations that appear as dark "holes" in the confocal images actually contain cone inner segment structure (Figure 1-16). Many studies have now started to capitalize on the advantages conferred by simultaneous confocal and split detector AOSLO imaging to examine photoreceptors in different disease conditions (Gill et al., 2019; Patterson et al., 2018; Randerson et al., 2015; Scoles et al., 2017; Sun et al., 2016).

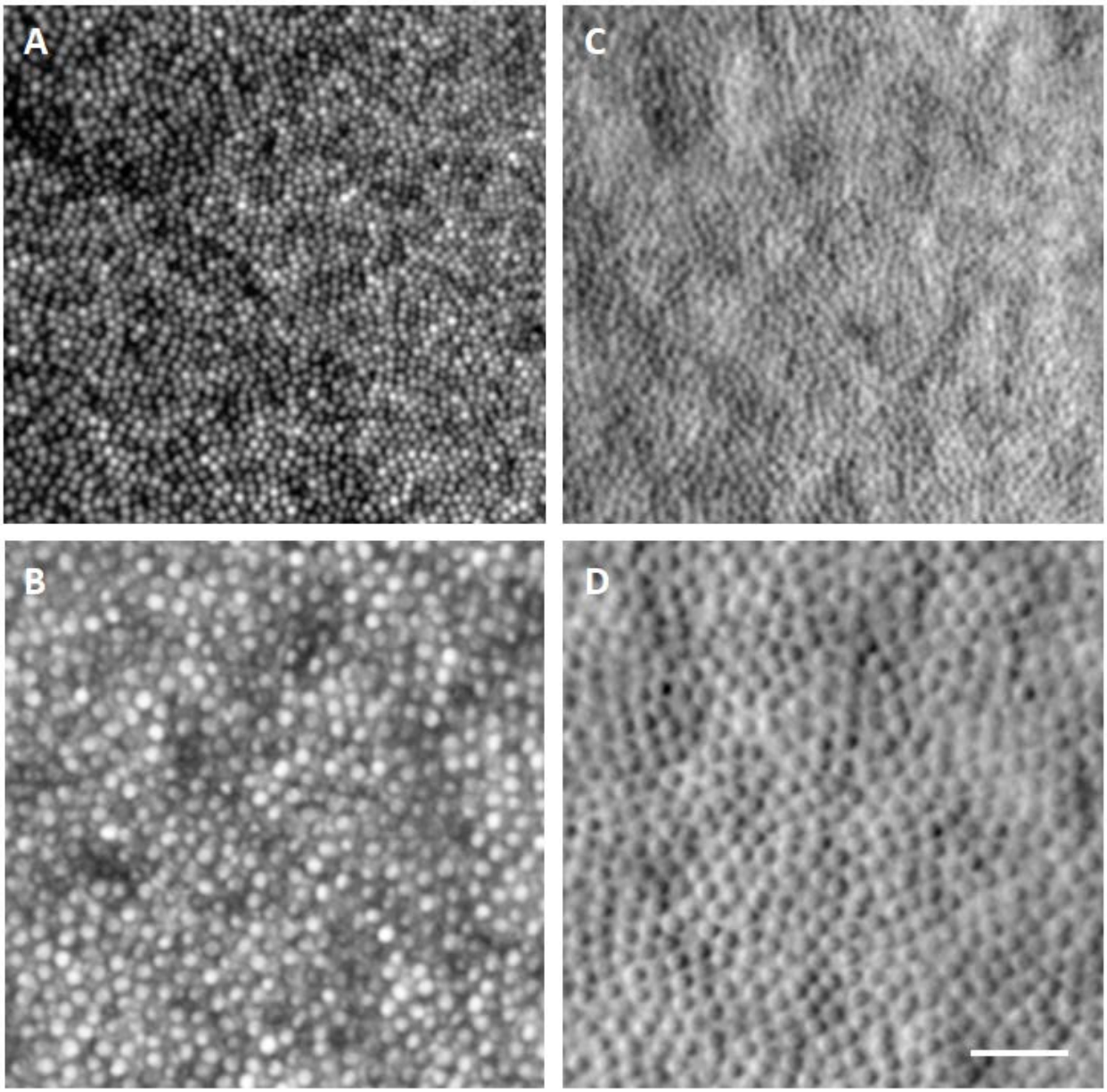

Figure 1-15. Confocal (A and B) and corresponding split-detector (C and D) images of photoreceptors at eccentricities of 1° (top row) and 5° (bottom row) from the foveal center in a healthy subject. (Scale bar: 50 µm)

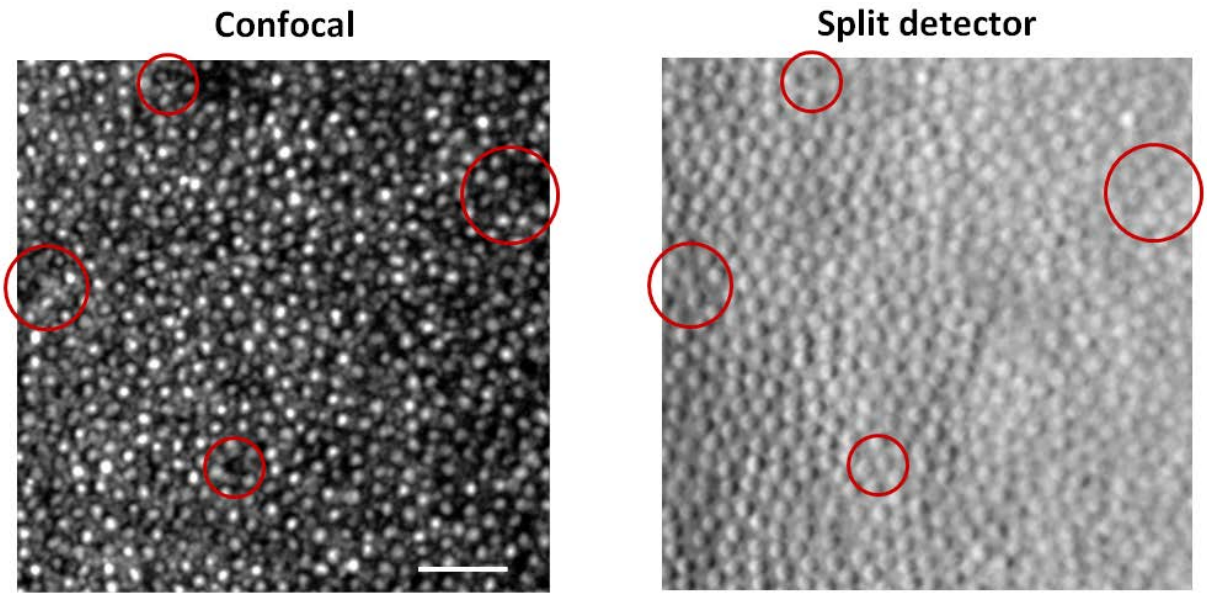

Figure 1-16. Confocal and split-detector images of the same retinal location showing cone photoreceptors in a healthy human subject (5° eccentricity). Locations circled in red in the confocal image represent areas with dark "holes" or areas where it is challenging to mark the locations of individual cone photoreceptors. Circles draw in the same corresponding locations in the split-detector image clearly show the presence and locations of cones. Scale bar: 25 µm.

1.4.6 Houston AOSLO

All of the *in vivo* imaging work described in this dissertation was performed using the Houston AOSLO. The Houston AOSLO uses a superluminescent diode (SLD) (S-Series Broadlighter, Superlum, Carrigtwohill, Ireland) with a central wavelength of 840 nm (full width at half maximum = 50 nm) for performing adaptive optics correction and imaging (Figure 1-17). Light from the SLD enters the system after reflecting off of a beam splitter (BS1) and reflects off of several afocal telescopes (spherical mirrors M1 through M8), horizontal and vertical scanners (HS and VS), deformable mirror (DM), and a dichoric mirror (DCM) before entering the eye. The light reflected back from the eye takes the opposite path to reach the second beam splitter (BS2), where a small portion of light is reflected to the wavefront sensor (WS) and the remaining light propagates to the imaging channels. Light reflected off of the annular mirror (AM) propagates to the confocal channel, while the light that passes through the transparent annulus

is split in half by a knife-edge mirror (KM) and is collected by the 2 photomultiplier tubes (PMTs) comprising the split detector channel (PMT 2, PMT 3).

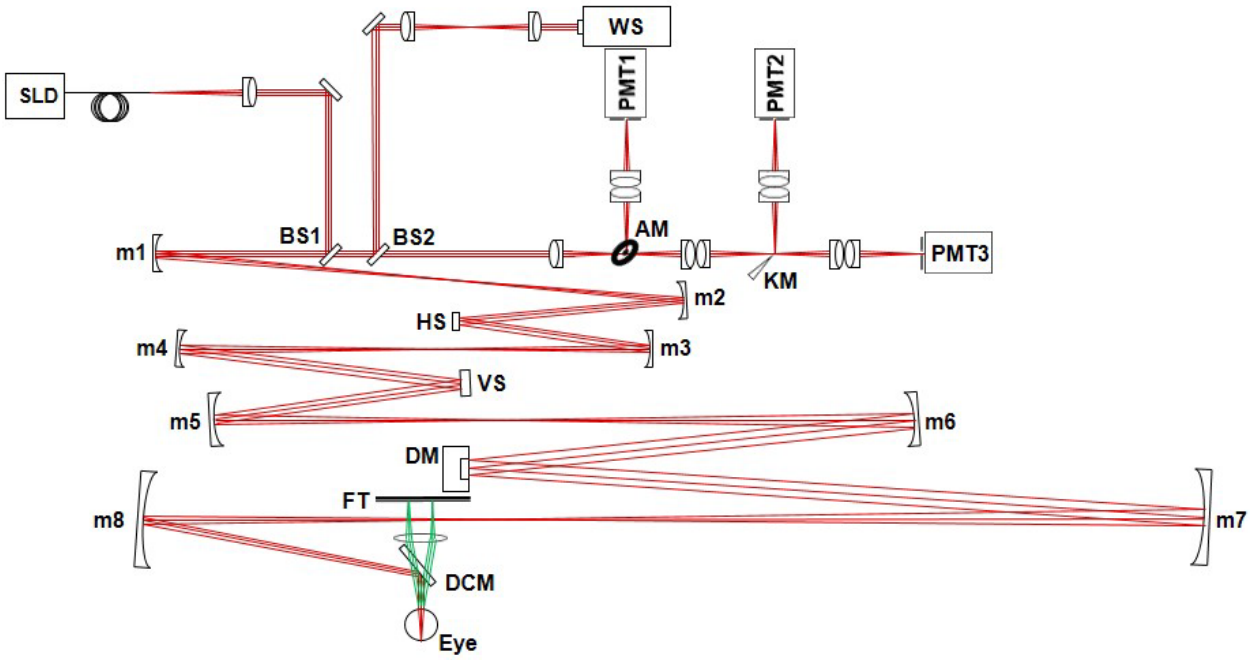

Figure 1-17. A schematic of the Houston AOSLO system, flattened for clarity. Light from a superluminescent diode (SLD) is projected into the system via beamsplitter 1 (BS1) and travels to the eye. Light reflected from the eye follows the reverse optical path. A portion of this light is diverted by beamsplitter 2 (BS2) to the wavefront sensor (WS) for aberration measurement and is corrected by a deformable mirror (DM; Alpao DM97-15). After passing through BS2, the central portion of the light is reflected by the annular mirror (AM) to the confocal channel (PMT1), while the multiply scattered light continues straight toware the split detector configuration (PMT2 and PMT3). SLD: Superluminescent diode; BS1, BS2: beam splitters; AM: annular mirror; KM: knife-edge mirror; HS: horizontal scanner; VS: Vertical scanner; DM: deformable mirror; WS: Shack-Hartmann wavefront sensor; PMT: photomultiplier tube; m1 to m8: spherical mirrors; DCM: dichroic mirror, reflects 750-850 nm and transmits 400-750 nm; FT: fixation target.

1.5 Quantification of AO photoreceptor images

1.5.1 Methods for marking cones

While the number of studies that quantify cone properties in healthy and diseased eyes continues to rise, it is rare for studies to explicitly mention their rules for determining how to mark cones within an image. In general, there is a lack of data detailing the impact of different marking techniques on the quantification of cone and/or rod photoreceptors from adaptive optics images. A very common method used for marking cones is a semi-automated approach in

which an algorithm first identifies the center of each cone automatically (usually based on an average spacing identified by the user), followed by a manual correction of erroneous markings and/or a manual addition of unmarked cones (Garrioch et al., 2012). Fully automated approaches developed to automatically detect cones can work well (Cooper et al., 2013; Li et al., 2010; Xue et al., 2007), but can also suffer from their own limitations (such as failing to identify partial cones that are always present at the edges of images). This dissertation attempts to clarify methods that can quantify cone properties with highest accuracy and least variability.

1.5.2 Methods for identifying regions of interest for quantifying cones

In order to quantify cone metrics at a particular eccentricity, one needs to define a certain area, or region of interest (ROI), over which the cones are to be analyzed. The size of this region of interest is a variable that can impact the calculated cone metric values. Studies have implemented a diversity of approaches for selecting the ROI size(s) used to analyze the cone mosaic. Some studies have used fixed ROI sizes equivalent to the sizes used by Curcio et al (1990) in order to better facilitate the comparison of *in vivo* values with Curcio's *ex vivo* data, while others have used variable sizes (Garrioch et al., 2012; Morgan et al., 2014; Song et al., 2011). Instead of keeping the ROI size fixed, other studies (Li et al., 2010) have examined ROIs that contain a fixed number of cones. The use of this latter method means that ROI size will change as a function of eccentricity due to changes in cone size and spacing in healthy eyes, and could vary considerably in diseased eyes, where cones may be lost in random ways.

To date, only a few studies have compared metrics quantified using different ROI sizes (Lombardo et al., 2014; Zhang et al., 2015). Lombardo et al. (2014) investigated different factors that could influence the variability of cone density measurements in AO images. However, their analysis was performed at a single eccentricity for 3 different ROI sizes. Their results showed that cone density decreases with decreasing ROI size and there is low agreement in density measurements between the ROI sizes they examined. Zhang et al. (2015) used different ROI

sizes (ranging from 2.5 μm to 40 μm) in 4 subjects to assess cone densities from the center of the retina to an eccentricity of 1.2 mm and found that cone densities at eccentricities greater than 0.3 mm are not affected by ROI size, while the use of smaller ROI sizes yields higher densities for eccentricities less than 0.03 mm.

1.5.3 Metrics for quantifying cones

Multiple metrics have been used to quantify the cone mosaic from *in vivo* images. The metrics that have been most commonly calculated to date are unbound and bound cone densities (Chui et al., 2008; Song et al., 2011). Unbound density is defined as the total number of cones within an ROI (regardless of a given cone is fully or partially within the ROI) divided by the total area of the ROI. Bound density examines the density of only those cones that are fully contained within an ROI and are "bound" by neighboring cones. To compute bound cone density, one must first determine the area of the Voronoi cell for each bound cone (Baraas et al., 2007). A Voronoi cell is defined as the area surrounding a given cone such that all of the points that lie within that area are closer to the given cone than to any other neighboring cone. Once the area of the Voronoi cell has been defined for each bound cone, one can calculate bound cone density as the ratio of the number of bound Voronoi cells in an ROI to the summed area of the bound Voronoi cells. While density is a valuable metric, it is not as sensitive to detect a diffuse cone loss as regularity metrics are. So, the robustness of the density metric may not detect a small change in the cones over time. Consequently, more recent studies have examined a myriad of metrics other than density, including spacing and regularity metrics (Legras et al., 2018; Park et al., 2013; Wang et al., 2019; Zayit-Soudry et al., 2015). Cooper et al. (2016) defined multiple density, spacing, and packing metrics and evaluated how these metrics change when randomly undersampling the cone mosaic. Their results showed that the metrics that are most sensitive to undersampling are regularity metrics, while the least sensitive metrics are spacing metrics. This

dissertation will discuss different factors that can further affect these metrics computed from AOSLO images.

1.5.4 Repeatability of quantifying cone packing

Multiple studies have investigated photoreceptor degeneration in retinal diseases and following therapeutic intervention (Birch et al., 2016; De Rojas et al., 2017; Scarinci et al., 2015). Adaptive optics imaging could play an important role in improving our understanding of disease progression and the effectiveness of therapies on a cellular level. As one example, AOSLO imaging was used by Talcott et al. (2011) to longitudinally examine eyes with retinitis pigmentosa after being treated with ciliary neurotrophic factor (CNTF). This study showed that cone density did not decrease in the eyes treated with CNTF, but did decrease by 9% to 24% in 8 of 9 different retinal locations in eyes that received no treatment over the course of 2 years.

In order to better assess the performance of future treatments, it is important to first understand the variability that is inherent in the imaging and image processing techniques within and across imaging sessions in healthy eyes. Garrioch et al. (2012) calculated the intrasession repeatability of *in vivo* parafoveal cone density in 21 normal subjects imaged at 4 locations with an eccentricity of 0.65°. They found an average coefficient of repeatability of 1,967 cones/mm^2 (2.7% of 75,528 cones/mm^2). In addition to studying intrasession repeatability, there is limited data describing the inter-session repeatability or variability in quantifying cones. A handful of reports have provided longitudinal repeatability data on single subjects. In the study by Talcott et al., one healthy subject was imaged at a single location at baseline and again after 4.5 years. It was found that only 0.4% of the cones that were imaged at baseline were not visualized at 4.5 years. Another study by Song et al. (2011) imaged one particular location of a healthy subject at baseline and again after 6 months and found that cone density varied by less than 2%. In a more comprehensive study, Jackson et al. (2019) imaged 14 eyes of 9 healthy subjects using a confocal AOSLO at 5 different eccentricities at baseline and again after 2 years to calculate

mean differences in a single metric (cone density) across subjects. They concluded that this variability must be considered while imaging cone photoreceptors longitudinally in diseased eyes.

1.6 Specific Aims

The goal of this dissertation research was to better understand the variability inherent in measurements of cone structure using current adaptive optics imaging and image processing techniques. We hope that the results from these studies will potentially provide more standardized methods for analyzing cone photoreceptor images in future studies and better facilitate the comparison of cone packing data across laboratories and experiments, and in clinical trials.

1.6.1 Specific Aim 1 - Determine the repeatability of quantifying cone photoreceptor packing metrics in confocal and split-detector AOSLO images from healthy eyes

The ability to assess whether changes in the photoreceptor mosaic have occurred over time (such as for diseased eyes or clinical trial-related applications) depends on the intrasession and longitudinal variabilities of the imaging and quantification techniques. While recent work has examined the intrasession variability in quantifying cone density and spacing (Garrioch et al., 2012) and the longitudinal variability in quantifying cone density from confocal AOSLO images (Jackson et al., 2019), there is a lack of data detailing the longitudinal variability in cone packing metrics (other than density) as measured from confocal *and* split detector images of the cone mosaic (particularly for peripheral retinal eccentricities), as well as the level of agreement between measurements obtained from the two modalities at the same retinal locations. We acquired confocal and split-detector images of cone photoreceptors from the fovea to 10° eccentricity in each of 4 major meridians using AOSLO imaging in eyes of 10 healthy subjects at 2 different time-points (baseline and 12 months from baseline). Cone packing metrics (including

density, spacing, and regularity metrics) were quantified at each retinal location and compared between time points in all eyes, as well as between imaging modalities. This experiment revealed the repeatability with which cone packing measurements can be made over time in the same eyes using confocal and split detector imaging.

1.6.2 Specific Aim 2 - Determine the impact of different cone marking techniques on the quantification of cone packing measurements in images of simulated and in vivo cone mosaics of healthy eyes

Currently, no standardized approach has been recommended for marking cones in AO images. Consequently, different methods have been used to identify and mark cones in AO images from living eyes (Li & Roorda, 2007; Song et al., 2011; Xue et al., 2007) with little knowledge of whether different marking techniques can result in different values. A very common method used to quantify cell packing in histological studies is to mark and include all cones that lie along two adjacent edges of the ROI (regardless of whether they reside completely within the ROI), and not mark cones along the other two edges. However, this method assumes a relatively uniform distribution of cells on each side of the ROI. Such an assumption could be problematic for analyzing cone packing in the retina, where it is known that cone density can change rapidly with eccentricity and could yield different cell counts on one side of an ROI versus another. Cones within different ROIs were randomly extracted from simulated cone mosaics with known, uniform densities and were marked using one of three techniques: marking all cones fully within the ROI and partially within the ROI along (1) all 4 borders, (2) the top and right borders only, and (3) the bottom and left borders only. Bound and unbound cone metrics were calculated and compared with known values for each marking technique and between different simulated densities. The same three techniques were used to mark cones in ROIs extracted from *in vivo* cone images acquired in 5 healthy subjects at different retinal eccentricities. Cone metrics were again calculated and compared between marking techniques. The study provides measures of

the variability in quantifying cone metrics using different marking techniques and recommends a method that provides the greatest accuracy with least variability.

1.6.3 Specific Aim 3 - Determine the impact of different ROI sizes on the quantification of cone packing measurements in images of simulated and in vivo cone mosaics from healthy eyes at different eccentricities

Multiple approaches have been used to select a region of interest (ROI) size for analyzing cone packing in living eyes, with many (but not all) studies using a fixed ROI size equivalent to the size used by Curcio et al. (1990) when analyzing receptor packing in excised retina (Lombardo, Lombardo, et al., 2013; Xue et al., 2007). While seemingly appealing, the use of a fixed ROI size to examine cone geometry at all eccentricities could result in variable and erroneous measurements of photoreceptor geometry. For example, selecting a large, fixed ROI that captures a sufficient number of widely spaced cones in the periphery could result in an oversampling of the mosaic near the fovea (i.e. include too many cones in a region where density changes very rapidly) and lead to erroneous measurements. Conversely, the selection of a small ROI size may work well to accurately quantify metrics near the fovea at the expense of potentially undersampling the mosaic in the periphery (where cones are widely spaced and decreased in their relative numbers per unit area). Few published studies have examined the impact of changing the size of the ROI used to calculate such metrics (Lombardo et al., 2014; Zhang et al., 2015). These studies have been limited in the packing metrics that were calculated, the retinal eccentricities examined, or the number of subjects included. A custom MATLAB program was written to generate simulated images of cone mosaics with gradient densities based on histological reports. Cone densities were quantified at different simulated eccentricities using 5 different square ROIs (25μm x 25μm to 100μm x 100μm) and compared with known densities. Confocal and split detector AOSLO images were acquired from the foveal center to ~10° eccentricity in 5 healthy eyes. Packing metrics were quantified using the same 5

ROI sizes at each eccentricity and compared across ROI sizes and with eccentricity. Also, the relative contributions of different factors on the total variability of the computed metrics were calculated. This experiment revealed whether significant differences in metric values exists due to the use of different ROI sizes use across different eccentricities.

CHAPTER 2

Longitudinal assessment of cone photoreceptor metrics in healthy adult eyes from *in vivo* confocal and split detector adaptive optics images

Contributing Authors:

Gwen Musial Ph.D., Alexander W. Schill Ph.D., Hanieh Mirhajianmoghadam M.S., Hope M. Queener M.S., Jason Porter Ph.D.

2.1 Introduction

The high resolution imaging capabilities afforded with the use of adaptive optics (AO) has enabled the visualization of individual cells in the living retina (Chui et al., 2008; Miller et al., 1996; Song et al., 2011). One cell type that has been studied predominantly in the human eye using AO is the cone photoreceptor (Chui et al., 2008; Liang et al., 1997; Roorda & Williams, 1999; Rossi & Roorda, 2010). An increasing number of studies have calculated metrics of cone photoreceptor packing (e.g., cone density and spacing) in healthy eyes from *in vivo* confocal adaptive optics scanning laser ophthalmoscope (AOSLO) images (Chui et al., 2008; Rossi & Roorda, 2010). More recently, AO imaging has been performed to characterize photoreceptor structure in diseased eyes, including eyes with inherited retinal degenerations (Talcott et al., 2011; Morgan et al., 2014; Zayit-Soudry et al., 2013; Tanna et al., 2017., Patterson et al 2018), opening the door for longitudinal studies that assess changes during disease or following therapeutic intervention.

The ability to assess whether changes in the photoreceptor mosaic have occurred over time depends on the intrasession and longitudinal variabilities of the imaging and quantification techniques. Garrioch et al (2012) examined the intrasession variability in quantifying cone density and spacing in a set of healthy eyes and found a repeatability of 6.4% using purely automated techniques that improved to 2.7% with manual correction. More recently, Jackson et al (2019) examined intersession differences in cone density from confocal AOSLO images taken around the fovea and along the temporal meridian to an eccentricity of 1.5 mm (~5 degrees) in healthy adult eyes over the course of 2 years. Despite these important advances, there is still a lack of data detailing the longitudinal variability in cone packing metrics other than density as measured from confocal and split detector images of the cone mosaic (particularly for peripheral retinal eccentricities). In addition, there is a need for increased clarity on the level of agreement between measurements obtained from confocal and split detector images at the same retinal locations.

The purpose of this study was to determine the repeatability of quantifying cone photoreceptor packing metrics from confocal and split-detector AOSLO images acquired in healthy, adult eyes over a 12 month period. Cone packing metrics (including density, spacing, and regularity metrics) were quantified at each retinal location (from the fovea to 10° eccentricity in each of 4 major meridians) and compared between time points in all eyes, as well as between imaging modalities. These experiments are expected to reveal the level of agreement between confocal and split-detector images, and the repeatability with which we can image and quantify cone photoreceptor packing over time.

2.2 Methods

The study was approved by the Institutional Review Board at the University of Houston and adhered to the tenets of the Declaration of Helsinki. Informed consent was obtained from all subjects prior to participating in the study and after explaining all procedures. The best-corrected visual acuity of each subject was at least 20/20 and subjects had no history of ocular trauma or disease. In order to calculate the lateral dimensions of retinal images, we measured and incorporated each subject's anterior chamber depth, anterior corneal curvature, lens thickness, and axial length (Lenstar; Haag-Streit, Koeniz, Switzerland) into a four-surface model eye to find the location of the eye's secondary nodal point and determine a scale factor (in terms of microns per degree). In the model, the posterior radius of curvature of the cornea was calculated as 0.8831 x (anterior radius of curvature of the cornea) (Williams, 1992). The refractive indices for the aqueous, lens, and vitreous were taken from LeGrand's Complete Theoretical eye (Le Grand & El Hage 1980) while the index of the cornea was assumed to be 1.38.

Each subject's pupil was dilated using phenylephrine hydrochloride (2.5%) and tropicamide (1%). A wide-field scanning laser ophthalmoscope (SLO) image of the fundus was taken using the Spectralis HRA+OCT (Heidelberg Engineering, Heidelberg, Germany). This

wide-field image was used to navigate through the retina and image the desired locations at different time points.

2.2.1 AOSLO imaging of subjects

A superluminescent diode with a central wavelength of 840 nm (S Series Broadlighter Superluminescent Diode, S-840-B-I-20, Superlum, Carrigtwohill, Ireland; Full Width at Half Maximum = 50 nm) was used for wavefront sensing and reflectance imaging. The power of the light at the corneal plane was 300 μW, which is 10 times below the maximum permissible exposure determined by the ANSI standards(ANSI, 2014; Delori et al., 2007). Aberrations were measured using a Shack-Hartmann wavefront sensor and corrected using a deformable mirror (Hi-Speed DM97-15, ALPAO, Montbonnot-Saint-Martin, France). Confocal and split detector videos of the retinal image are recorded simultaneously in a manner consistent with that described by Scoles et al. (2014).

The head of each subject was stabilized using a bite-bar prepared after taking the dental impression of the subject. This set up was attached to an XYZ translation stage in order to align the beam with the subject's pupil and place the subject's pupil in a pupil-conjugate plane. Confocal and split detector videos of cone photoreceptors were then acquired from the right eyes of all the subjects at a frame rate of 25Hz over a field size of 1.5°. Videos were acquired from the center of the retina (fovea) to approximately 10° from the fovea in all 4 major meridians (Superior, Inferior, Nasal, Temporal). During imaging, subjects were asked to look at a fixation target that was moved in 0.5° steps after acquiring ~200-300 frames from each location. Subjects were imaged at baseline and again at 12 months after the baseline.

2.2.2 Post-processing of AOSLO videos

All videos were first corrected for distortions created by the scanning mirrors using a customized program in MATLAB (Mathworks, Natick, Massachusetts, USA). Subsequently, a frame with

uniform brightness and no visible distortion was chosen manually as a reference frame from each confocal video. A strip registration process was performed using a customized program called Demotion (Dubra & Harvey, 2010; Stevenson & Roorda, 2005) to create stabilized confocal videos for each retinal location imaged. Approximately 50-100 frames were averaged from each stabilized video to produce registered confocal images. Averaged split-detector images of the same retinal locations were created after applying the alignments generated for each confocal strip to its corresponding split-detector strip that was acquired simultaneously over the same patch of retina. After generating registered confocal and split-detector images at each location, montages were constructed by manually stitching images together in Adobe Photoshop (Adobe Systems Inc., San Jose, CA USA) (Figure 2-1). The confocal montage was created first by aligning overlapping regions from consecutively acquired images; then, the corresponding split-detector montage was created by individually aligning the images and overlaying them on top of the corresponding confocal image acquired at the same location.

Due to difficulties in resolving the central-most foveal cones, the location of peak cone density was estimated using a custom MATLAB program based on the technique developed by Putnam et al. (2005), which estimates the location of peak cone density based on the density of resolved cones surrounding the fovea. This peak cone density location (corresponding to a retinal eccentricity of 0°) was then mapped from the confocal montage to the corresponding registered split-detector montage in the same eye.

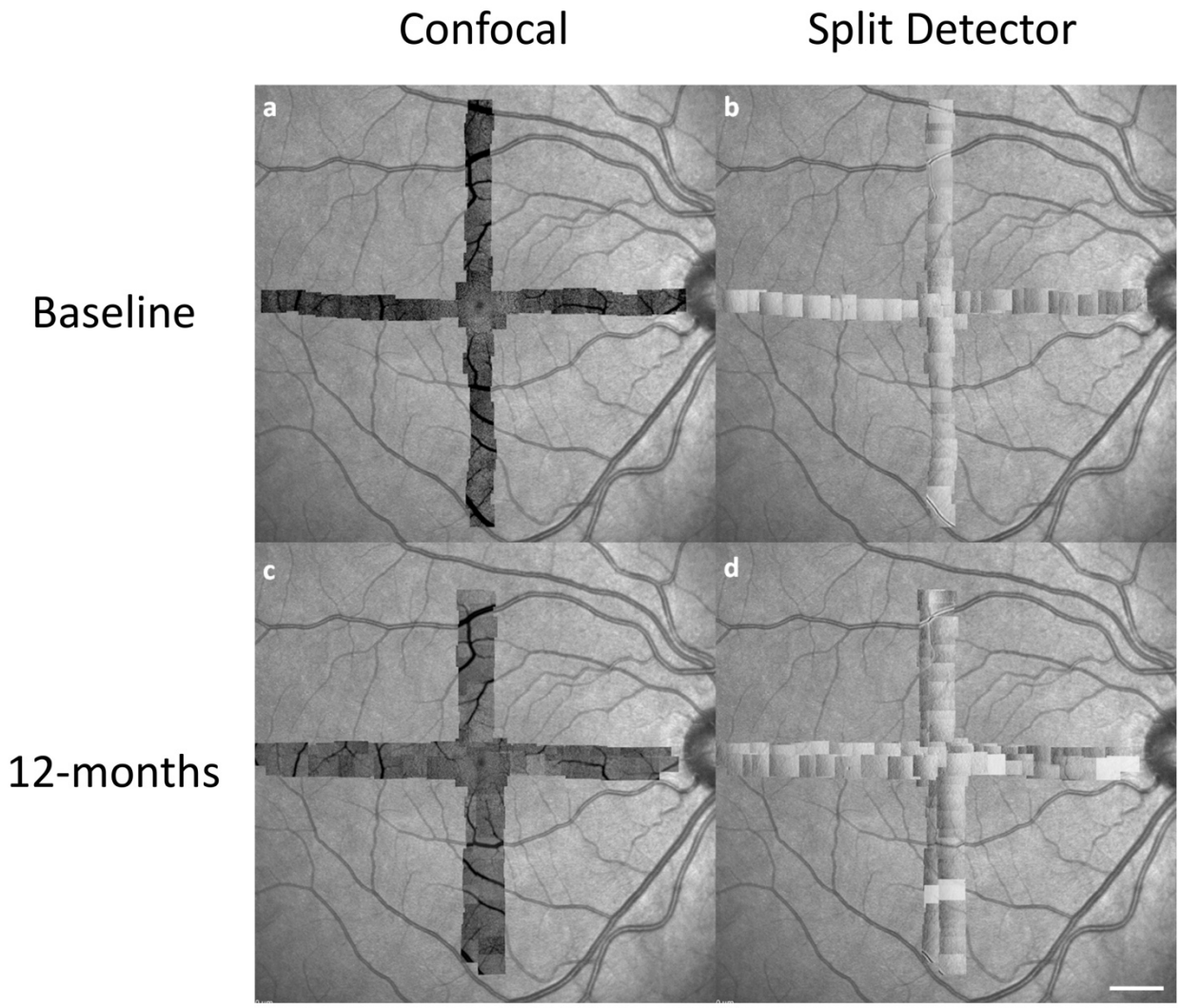

Figure 2-1. (a,c) Confocal montages of the cone photoreceptor mosaic acquired in a representative healthy adult eye at (a) baseline and (c) 12-month time points. (b,d) Corresponding split detector montages acquired simultaneously in the same eye at (b) baseline and (d) 12-month time points. Images were acquired from the fovea to an eccentricity of approximately 10° in each major meridian. AOSLO montages are overlaid on the Spectralis SLO image acquired in the eye of the same subject (Scale bar: 800 µm)

Concentric circles with radii from 0.3 mm to 3.0 mm (in 0.3 mm increments) were drawn on the montage such that their centers corresponded to the location of estimated peak cone density. Cone photoreceptor density, spacing, and regularity metrics were calculated in 0.3 mm increments within a square region of interest (ROI) along each major meridian for the registered confocal and split-detector montages in each subject. An ROI size of 37µm × 37µm was used for eccentricities between 0.3 mm and 1.2 mm, while an ROI size of 100µm × 100µm was used

for eccentricities of 1.5 mm and beyond. If the retinal location falling with the ROI being sampled at a given eccentricity included a region with a blood vessel shadow, the ROI was shifted radially along its corresponding concentric circle until the ROI contained only cone photoreceptors.

Cones were identified using a custom, semi-automated program called Mosaic Analytics (Translational Imaging Innovations, Hickory, NC USA). The algorithm, described by Cooper et al. (2016), applies a finite-impulse-response low pass filter to the retinal image, eliminating high-frequency noise, and then identifies a local maxima in the filtered image. For confocal images, cones were automatically detected by the program and, if needed, were manually modified to either add cones that were missed or remove misidentified cones. Due to the non-uniform appearance of cones in split detector images (i.e., one half of the cone appears bright while the other half appears dark), the previously described automated approach was inconsistent in its ability to properly identify cones. Consequently, cones in split detector images were manually marked. For this work, we present data on bound cone density (as cone density is the most commonly reported metric), as well as nearest neighbor distance (NND) and number of neighbors regularity (NoNR) (Cooper et al., 2016). To compute bound cone density, the algorithm first determines the area of the Voronoi cell for each bound cone (Baraas et al., 2007). A Voronoi cell is defined as the area surrounding a given cone such that all of the points that lie within that area are closer to the given cone than to any other neighboring cone. Once the area of the Voronoi cell has been defined for each bound cone, the algorithm calculates bound cone density as the ratio of the number of bound Voronoi cells in an ROI to the summed area of the bound Voronoi cells. NND is the mean of the linear distances between each bound cone and its closest neighbor inside the ROI. NoNR is the average number of neighbors for all the bound cones inside an ROI divided by the standard deviation of number of neighbors for all the bound cones. As reported by Cooper et al. (2016), NND and NoNR are the metrics which are the least

and most sensitive to a change in cones, respectively. The same procedures were used to analyze videos collected at baseline and at 12 months.

In order to assess the inter-observer reliability in the quantification of cone mosaic geometry metrics using mosaic analytics, a subset of 40 ROIs (both 37 µm × 37 µm and 100 µm × 100 µm) were chosen randomly from different eccentricities for different imaging modalities and were presented to an independent expert observer. After the second observer performed cone markings and quantification, the intraclass correlation coefficient (ICC) between the two observers was calculated for different cone metrics (Koo & Li, 2016).

2.2.3 Statistical analysis

All statistical analyses were done using Sigma Plot (Systat Software, Inc., San Jose, CA) and Microsoft Excel (2013). For the within-session analysis on the baseline data, we used a 3-way ANOVA to examine the effect of meridian, eccentricity, and imaging modality on cone metrics and determine whether differences existed between confocal and split-detector images. For the longitudinal analysis, cone metrics were compared between the two time-points (Baseline and 12-months) using a 3-way ANOVA to determine whether there were any significant effects of meridian, eccentricity, and time-point on cone metrics measured from confocal and split-detector images. Intersession repeatability was assessed using different metrics, including the within-subject standard deviation (S_w) and within-subject coefficient of variation (CV). In addition, we computed measurement error (ME) as the difference between the measured value and its true value (i.e., ME = $S_w \times 1.96$), and the Coefficient of Repeatability (CR = $S_w \times 2.77$) (Bland & Altman, 1999).

2.3 Results

Ten subjects (7 males and 3 females) participated in the study. The mean age was 29.4 ± 4.1 years (range: 26.2 – 40.1 years). Subjects had a mean axial length of 23.34 ± 0.78 mm (range:

22.34 mm-24.78 mm) with a mean spherical equivalent refractive error of -0.72 ± 1.13 D (range: +0.25 D to -3.25 D).

The average differences in density, NND, and NoNR between 2 observers and the differences as a percentage of mean values between the 2 observers are plotted in Figure 2-2. The mean percent differences in cone density (with the exception of an eccentricity of 1.2 mm) and in NND were less than ~4% of the mean value across eccentricities. Mean percent differences in NoNR were less than ~10% of the mean values across most eccentricites, with higher percent differences being noted at eccentricities of 0.6 mm, 0.9 mm, and 1.2 mm. The intraclass correlation coefficient, ICC(2,1), and associated confidence interval (CI) measures between 2 observers (Table 2-1) were excellent for density and NND and were good for NoNR, according to guidelines for the interpretation of ICC agreement measures (Domenic, 1994). On the basis of this generally good agreement between both observers, all markings were performed by a single observer, though the order of the eccentricities and imaging modalities that were marked were randomized.

Table 2-1. ICC and confidence interval values for different cone metrics quantified by 2 observers.

Variables	**ICC**	**Lower bound CI**	**Upper bound CI**
Density	0.99	0.99	1.00
NoNR	0.66	0.44	0.80
NND	0.99	0.96	0.99

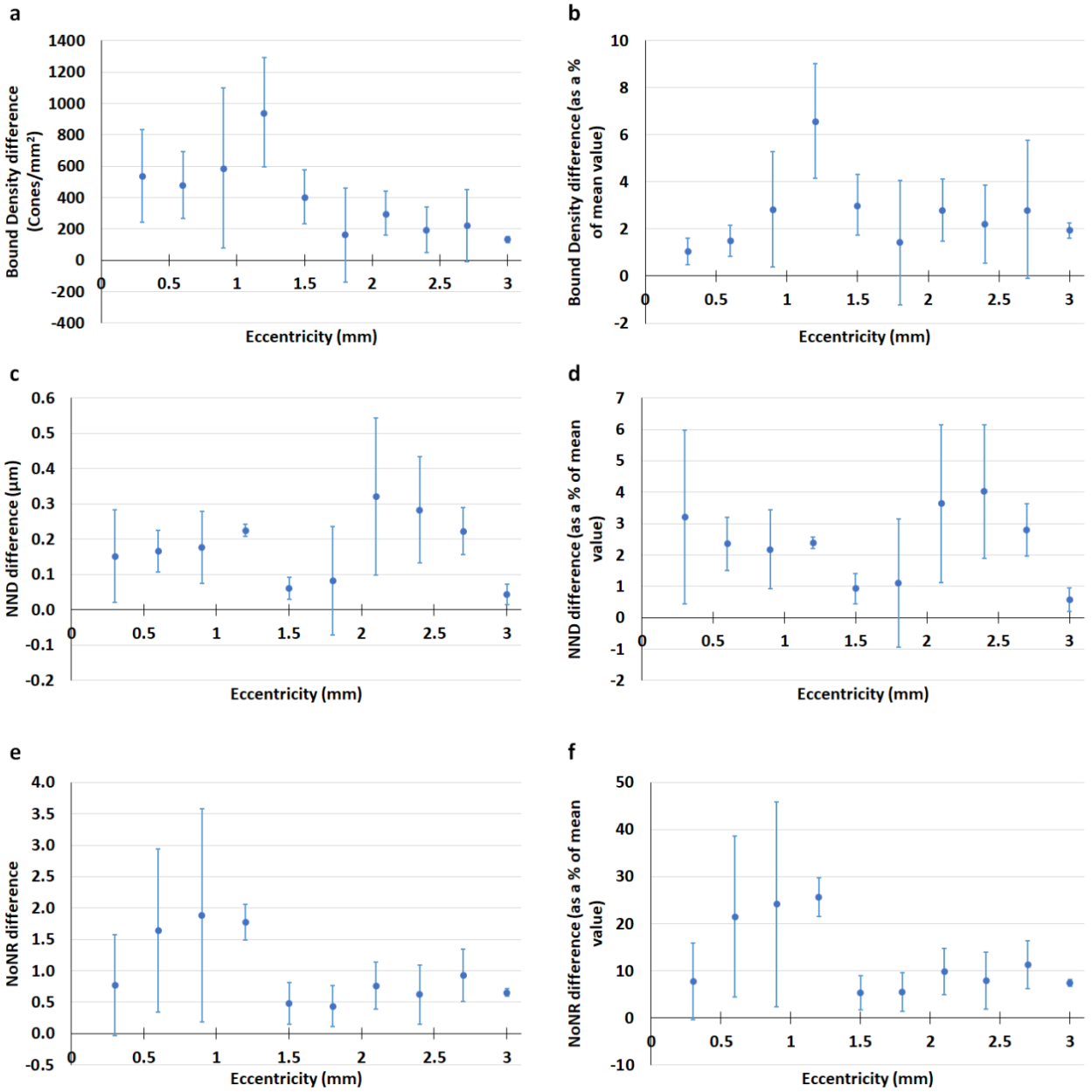

Figure 2-2. Differences in (a,b) Bound cone density, (c,d) nearest neighbor distance (NND), and (e,f) number of neighbors regularity (NoNR) as measured between 2 observers across different eccentricities. The differences are expressed as (a,c,e) actual differences (observer 1 – observer 2) and as (b,d,f) as a percentage of the mean of the values calculated by the 2 observers [(observer 1 – observer 2)/(mean of observer 1 and observer 2)]. Error bars represent ± 1 standard deviation.

2.3.1 Comparison between confocal and split detector images

There was excellent qualitative correspondence in cone structure between confocal and split-detector images at all locations (Figure 2-3). As expected, baseline cone density decreased (Figure 2-4) and cone spacing (i.e., nearest neighbor distance) increased (Figure 2-5) with increasing eccentricity from the location of estimated peak cone density. The regularity of the cone photoreceptors (assessed using number of neighbors regularity, NoNR) was relatively consistent with eccentricity, as shown in Figure 2-6.

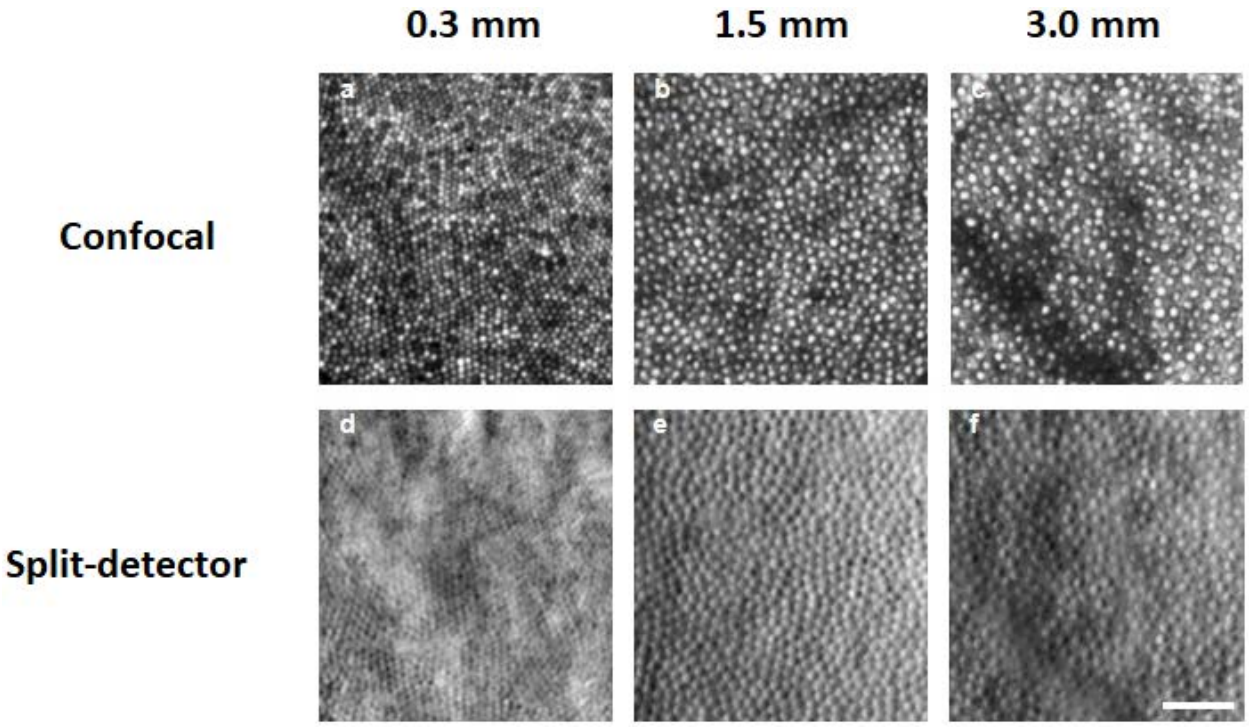

Figure 2-3. Representative images of cone photoreceptors acquired at different eccentricities using different AOSLO imaging modalities at baseline. (Top row) Confocal and (bottom row) split detector AOSLO images of the same retinal locations acquired at retinal eccentricities of (a, d) 0.3 mm, (b, e) 1.5 mm, and (c, f) 3.0 mm in a healthy 32-year old subject at baseline. Excellent agreement can be noted between corresponding confocal and split detector images. All images are presented at the same spatial scale. Scale bar: 50 µm

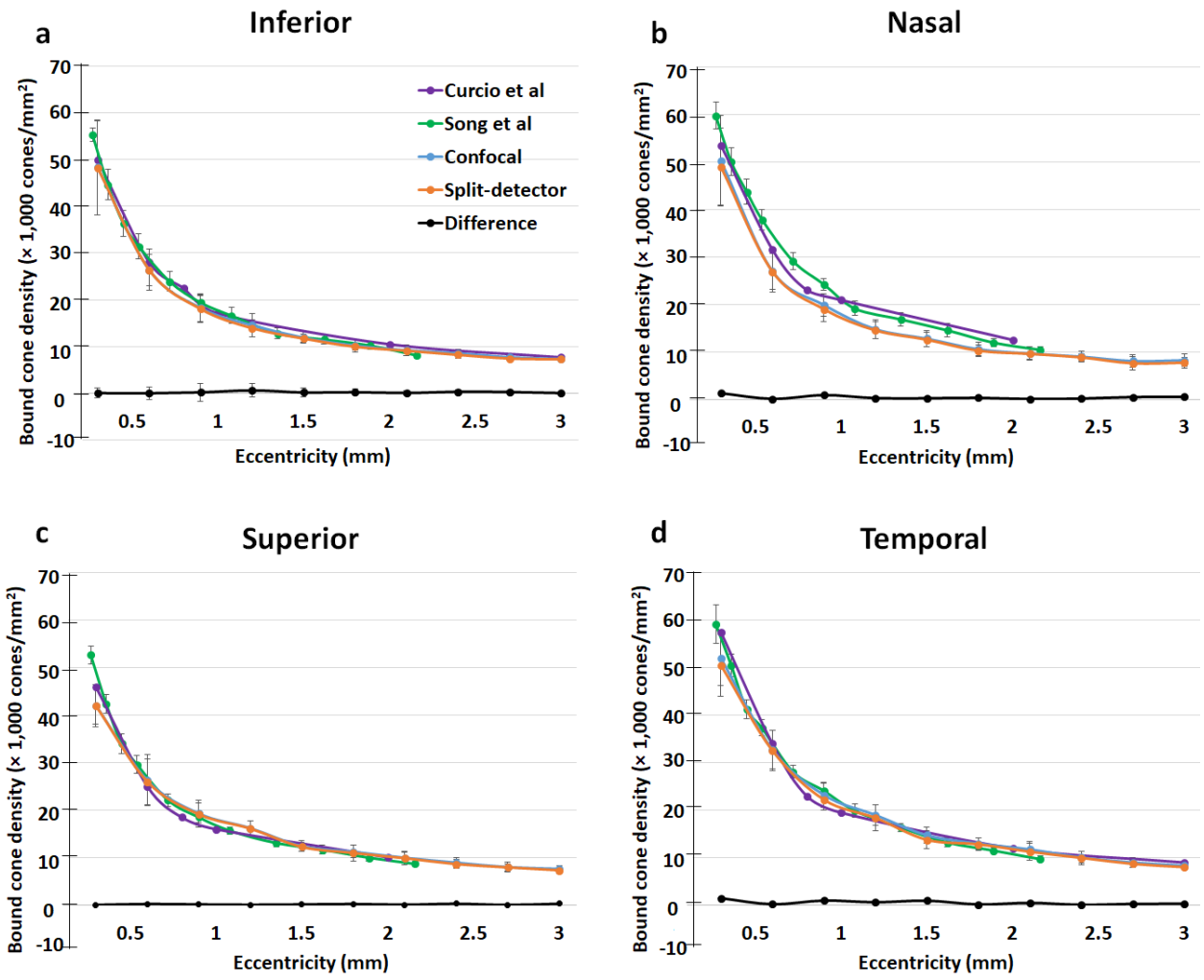

Figure 2-4. Bound cone density computed across all subjects for different eccentricities and different meridians at the baseline time point along with published in vivo and ex vivo data. Mean values of cone density for the (a) inferior, (b) nasal, (c) superior, and (d) temporal meridians obtained from confocal images (blue) and split detector images (orange) are presented as a function of eccentricity. Error bars represent ± 1 standard deviation. Cone density data are also compared with densities obtained from confocal AOSLO images in a separate group of adult subjects by Song et al. (2011) (green) and with values obtained histologically by Curcio et al. (1990) (purple). Mean differences between confocal and split detector cone densities (black) were approximately zero for all eccentricities.

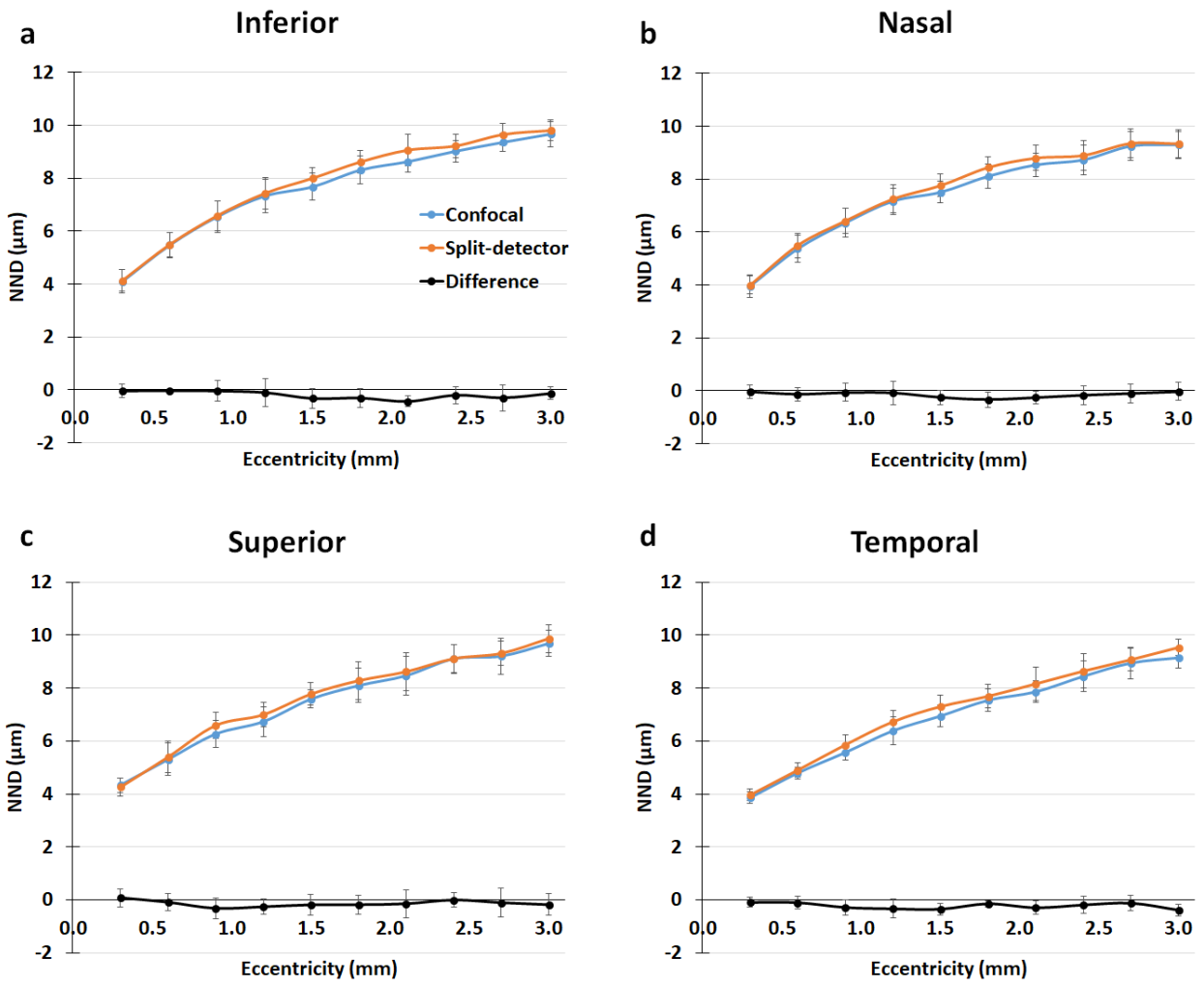

Figure 2-5. Nearest neighbor distance (NND) computed across all subjects for different eccentricities and different meridians at the baseline time point. Mean values of NND for the (a) inferior, (b) nasal, (c) superior, and (d) temporal meridians obtained from confocal images (blue) and split detector images (orange) are presented as a function of eccentricity. Error bars represent ± 1 standard deviation. Mean differences in NND between confocal and split detector images were approximately zero for all eccentricities.

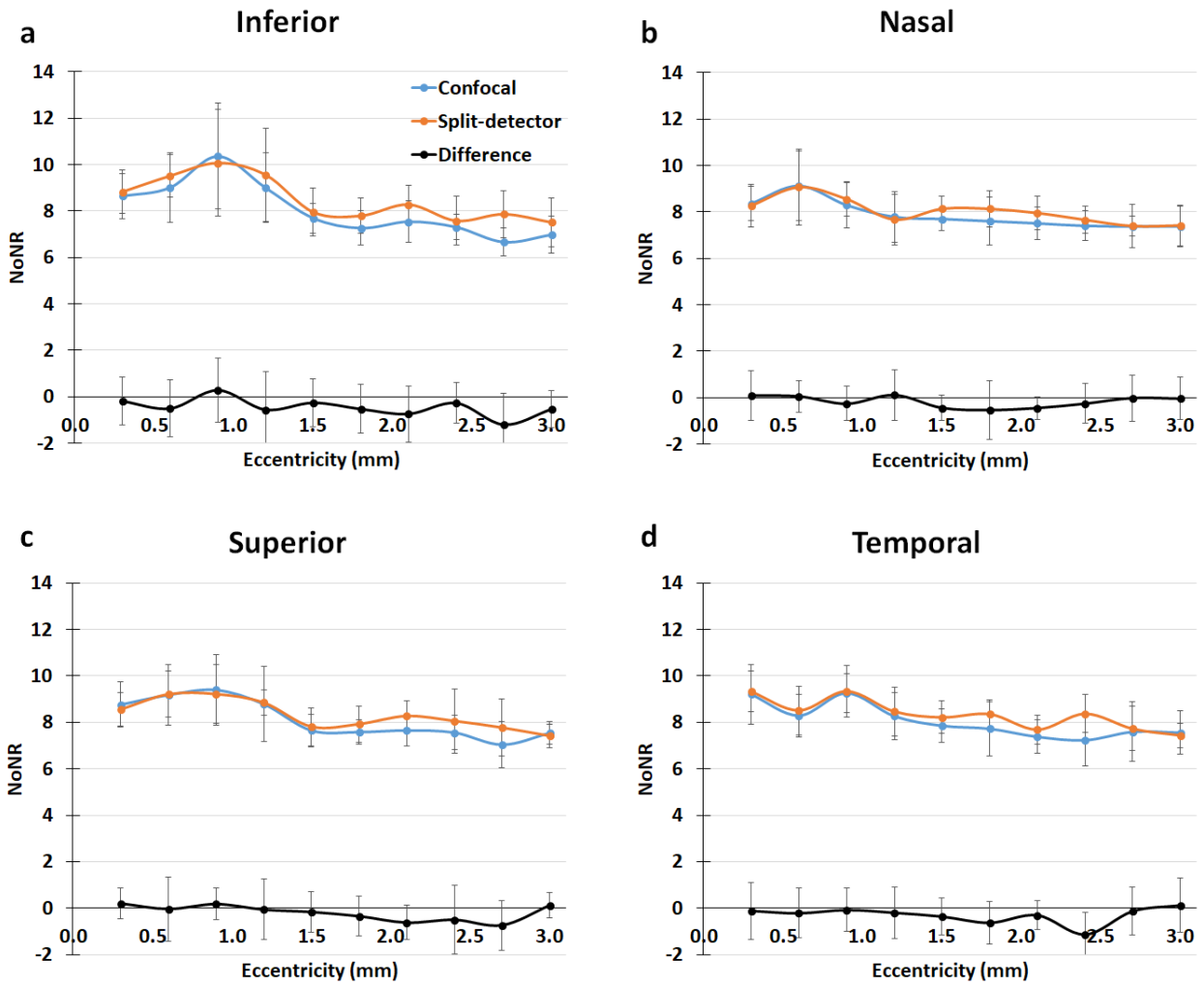

Figure 2-6. Number of neighbors regularity (NoNR) computed across all subjects for different eccentricities and different meridians at the baseline time point. Mean values of NoNR for the (a) inferior, (b) nasal, (c) superior, and (d) temporal meridians obtained from confocal images (blue) and split detector images (orange) are presented as a function of eccentricity. Error bars represent ± 1 standard deviation. Mean differences in NoNR between confocal and split detector images (black) were approximately zero for all eccentricities.

The mean differences in density, NND, and NoNR obtained between confocal and split-detector AOSLO images across all meridians ranged from 11 cones/mm^2 to 1,478 cones/mm^2, 0.01 µm to 0.44 µm, and 0.01 to 1.20, respectively. Within session analysis showed that for density and NND metrics, significant effects of eccentricity and meridian were observed ($P<0.05$ for each variable) with significant interactions between eccentricity and meridian ($P<0.001$ for density and $P<0.05$ for NND). The density decreased significantly with an increase in

eccentricity until 1.5 mm for inferior, superior and temporal meridian and until 1.2 mm for nasal meridian. Similarly, the NND increased significantly with an increase in eccentricity until 1.8 mm for inferior, nasal and superior meridian and until 2.4 mm for temporal meridian. No significant differences in cone density and NND were observed between confocal and split-detector modalities ($P>0.05$ for each variable). For NoNR, significant effects of eccentricity, meridian and modality were observed ($P<0.001$ for each variable) with significant interactions between eccentricity and meridian ($P<0.001$) and between eccentricity and modality ($P<0.001$). A post-hoc test revealed that NoNR values for eccentricities 1.8 mm, 2.1 mm, 2.4 mm and 2.7 mm were significantly different between confocal and split-detector modalities ($P = 0.02$, 0.001, 0.04, and <0.001 respectively).

2.3.2 Comparison between baseline and 12-month images

Representative confocal and split detector images of cone photoreceptors acquired at baseline and 12-month time points are shown in Figure 2-7 for different retinal eccentricities in 4 subjects. Figures 2-8 to 2-11 show a comparison of cone metrics measured at the 2 different time points as calculated from confocal and split-detector imaging modalities along different meridians.

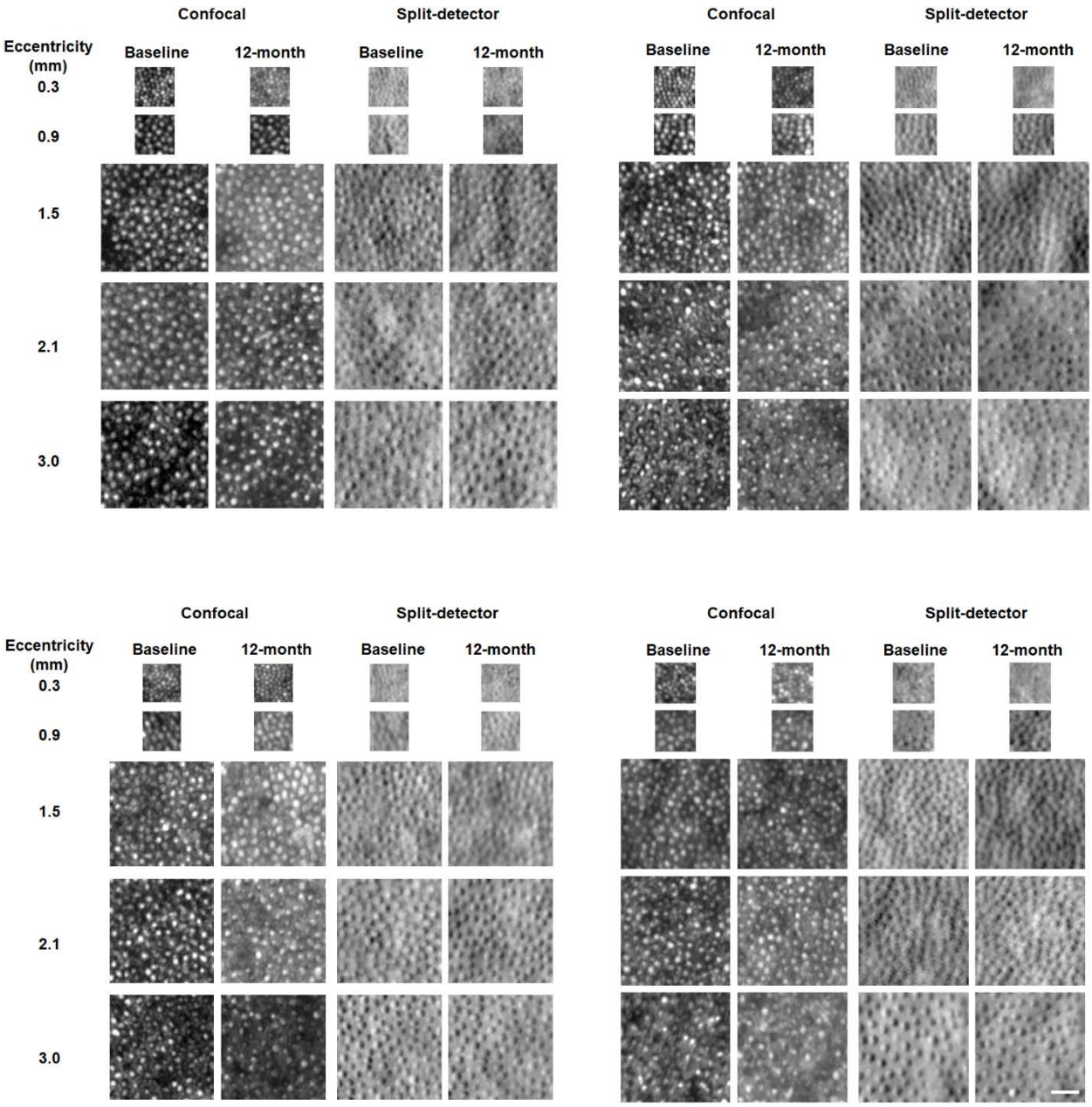

Figure 2-7. Corresponding confocal and split-detector images of cone photoreceptors from different eccentricities at baseline and 12-month follow-up time-points for 4 representative adult subjects. An ROI size of 37 µm × 37 µm was used for eccentricities between 0.3 and 1.2 mm, while an ROI size of 100 µm × 100 µm was used for eccentricities beyond 1.2 mm. Scale bar: 50 µm

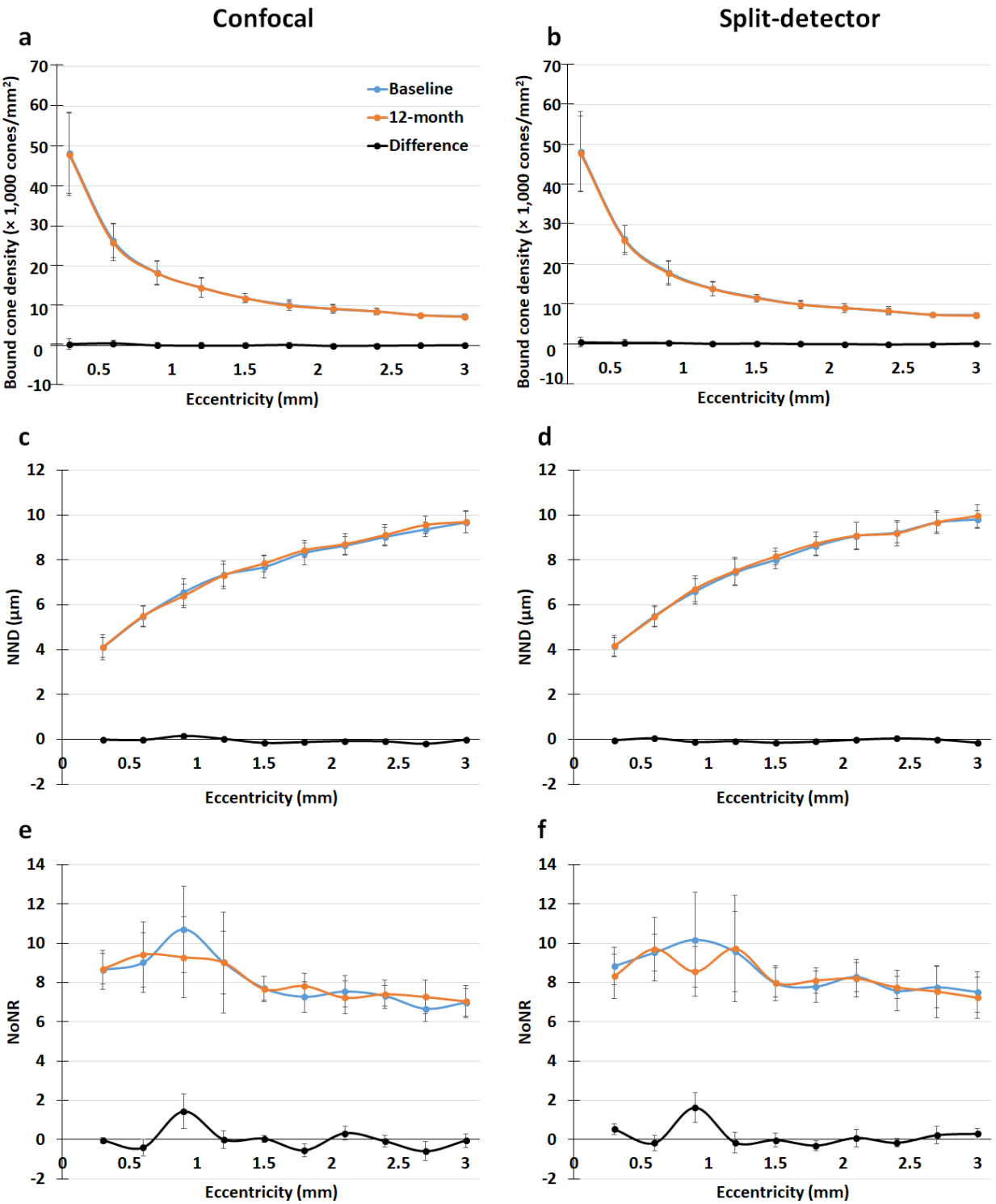

Figure 2-8. Differences in cone metrics between examined time-points across subjects. Mean values of (a,b) bound cone density, (c,d) nearest neighbor distance (NND), and (e,f) number of neighbors regularity (NoNR) obtained from (a,c,e) confocal images and (b,d,f) split detector images at baseline (blue) and 12-month (orange) time points as a function of eccentricity along the inferior meridian. Error bars represent ± 1 standard deviation. The mean differences in densities, spacings, and regularities between baseline and 12-month time points (black) were approximately zero for all eccentricities.

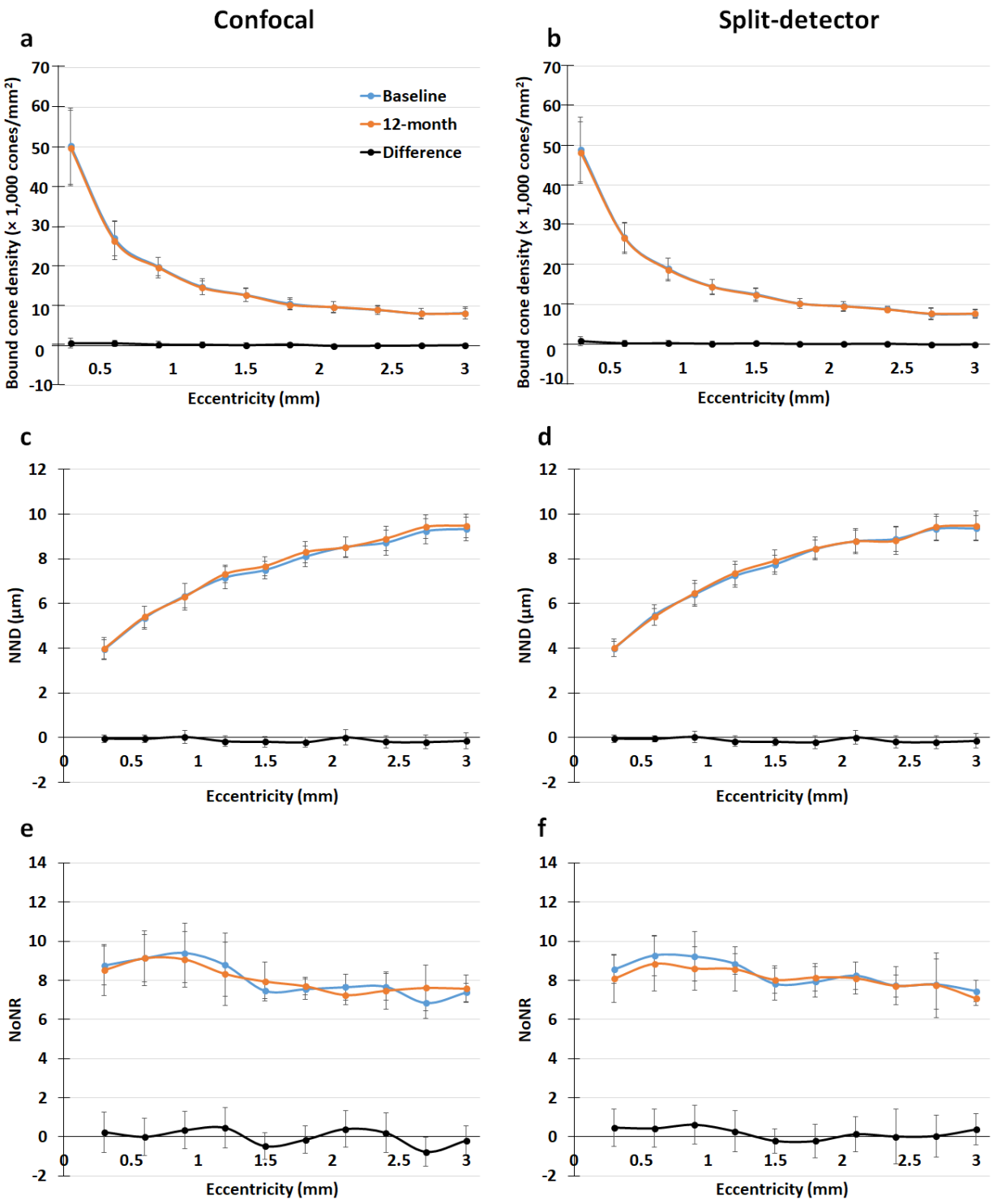

Figure 2-9. Differences in cone metrics between examined time-points across subjects. Mean values of (a,b) bound cone density, (c,d) nearest neighbor distance (NND), and (e,f) number of neighbors regularity (NoNR) obtained from (a,c,e) confocal images and (b,d,f) split detector images at baseline (blue) and 12-month (orange) time points as a function of eccentricity along the nasal meridian. Error bars represent ± 1 standard deviation. The mean differences in densities, spacings, and regularities between baseline and 12-month time points (black) were approximately zero for all eccentricities.

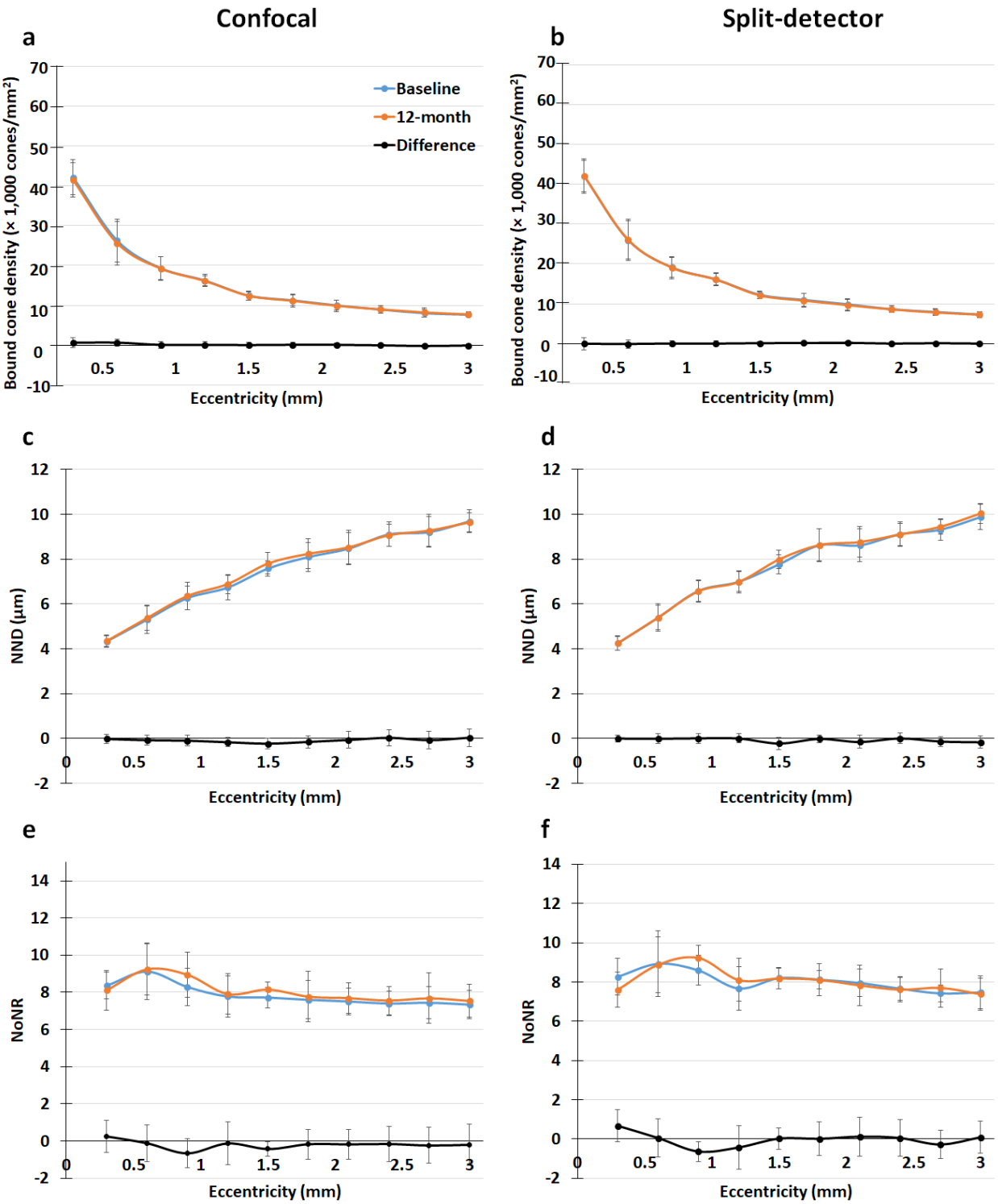

Figure 2-10. Differences in cone metrics between examined time-points across subjects. Mean values of (a,b) bound cone density, (c,d) nearest neighbor distance (NND), and (e,f) number of neighbors regularity (NoNR) obtained from (a,c,e) confocal images and (b,d,f) split detector images at baseline (blue) and 12-month (orange) time points as a function of eccentricity along the superior meridian. Error bars represent ± 1 standard deviation. The mean differences in densities, spacings, and regularities between baseline and 12-month time points (black) were approximately zero for all eccentricities.

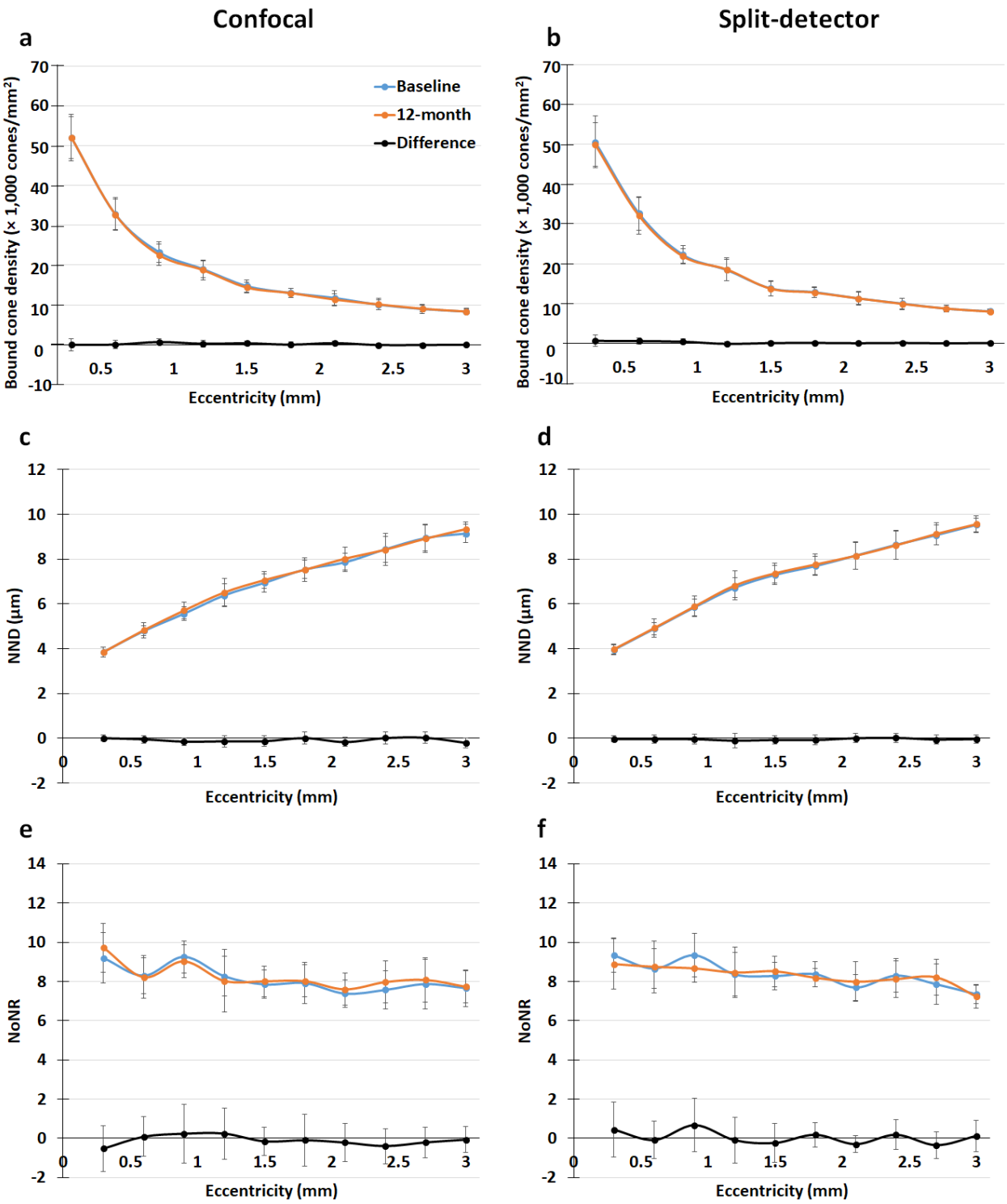

Figure 2-11. Differences in cone metrics between examined time-points across subjects. Mean values of (a,b) bound cone density, (c,d) nearest neighbor distance (NND), and (e,f) number of neighbors regularity (NoNR) obtained from (a,c,e) confocal images and (b,d,f) split detector images at baseline (blue) and 12-month (orange) time points as a function of eccentricity along the temporal meridian. Error bars represent ± 1 standard deviation. The mean differences in densities, spacings, and regularities between baseline and 12-month time points (black) were approximately zero for all eccentricities.

A three-way ANOVA was performed to investigate whether there were any significant effects of eccentricity, meridian, and time-point on cone metrics, and whether there were significant interactions between these variables. For density and NND metrics, significant effects of eccentricity and meridian were observed ($P<0.05$ for each variable) with significant interactions between eccentricity and meridian ($P<0.001$ for density and $P<0.05$ for NND). No significant differences in cone density and NND were observed between baseline and 12-month time points ($P>0.05$ for each variable). For NoNR, significant effects of eccentricity, meridian and time-point were observed ($P<0.05$ for each variable) with significant interactions between eccentricity and meridian ($P<0.001$) and between eccentricity and time-point ($P=0.002$). A post-hoc test revealed that there was a significant difference between NoNR at baseline and 12-month time points at an eccentricity of 2.7 mm ($P<0.001$). At all other eccentricities, there were no significant differences in NoNR between baseline and 12-month time points ($P>0.05$).

Measures of repeatability made for different cone metrics in different meridians using confocal and split detector imaging are shown in Tables 2-2 to 2-9. The average coefficient of repeatability of cone density measurements across all eccentricities and meridians was 8.42% (1,309 cones/mm^2) for confocal images and 6.29% (1,046 cones/mm^2) for split-detector images. Similarly, the average coefficient of repeatability of NND across all eccentricities and meridians was 7.17% (0.53 µm) for confocal images and 6.10% (0.45 µm) for split-detector images. For NoNR, the average coefficient of repeatability across all locations was 21.86% (1.77) for confocal images and 21.07% (1.74) for split-detector images.

Table 2-2. Repeatability of cone density, nearest neighbor distance (NND), and number of neighbors regularity (NoNR) for different eccentricities computed along the inferior meridian for confocal images

	Density				NND				NoNR			
Eccentricity (mm)	**S_w (%)**	**CV (%)**	**ME (%)**	**CR (%)**	**S_w (%)**	**CV (%)**	**ME (%)**	**CR (%)**	**S_w (%)**	**CV (%)**	**ME (%)**	**CR (%)**
0.3	2.0	2.1	3.9	5.6	2.6	2.1	5.1	7.3	7.5	7.3	14.6	20.7
0.6	2.4	2.4	4.7	6.6	2.4	2.2	4.8	6.7	8.0	6.6	15.6	22.0
0.9	2.4	2.3	4.8	6.7	2.8	2.4	5.5	7.7	9.7	8.3	19.0	26.9
1.2	3.1	3.1	6.1	8.7	3.2	2.5	6.2	8.8	10.0	9.1	19.7	27.8
1.5	3.7	3.3	7.2	10.1	2.6	2.3	5.1	7.1	7.2	6.8	14.2	20.0
1.8	3.6	3.0	7.1	10.0	2.5	2.0	4.9	7.0	8.3	7.0	16.2	22.9
2.1	3.3	3.1	6.4	9.1	2.0	1.7	3.9	5.6	7.5	6.1	14.6	20.7
2.4	2.9	2.7	5.8	8.1	1.9	1.6	3.8	5.4	9.5	8.8	18.7	26.4
2.7	2.7	2.7	5.4	7.6	2.2	1.8	4.4	6.2	9.2	8.1	18.0	25.4
3.0	2.8	2.5	5.5	7.8	2.1	1.8	4.1	5.8	7.2	5.2	14.1	19.9

Table 2-3. Repeatability of cone density, nearest neighbor distance (NND), and number of neighbors regularity (NoNR) for different eccentricities computed along the inferior meridian for split-detector images

	Density				NND				NoNR			
Eccentricity (mm)	**S_w (%)**	**CV (%)**	**ME (%)**	**CR (%)**	**S_w (%)**	**CV (%)**	**ME (%)**	**CR (%)**	**S_w (%)**	**CV (%)**	**ME (%)**	**CR (%)**
0.3	1.9	1.7	3.8	5.3	2.8	2.1	5.50	7.8	7.9	7.5	15.5	21.9
0.6	2.4	2.1	4.7	6.6	2.4	1.9	4.6	6.5	8.1	7.5	15.9	22.5
0.9	2.3	2.2	4.5	6.3	2.5	1.9	4.8	6.8	8.6	7.9	16.9	23.9
1.2	2.6	2.5	5.1	7.2	2.8	2.5	5.4	7.6	8.6	6.7	16.9	23.9
1.5	2.3	2.0	4.5	6.3	2.2	1.9	4.4	6.2	6.0	5.9	11.8	16.7
1.8	2.1	2.0	4.2	5.9	1.9	1.6	3.8	5.4	6.6	5.8	12.9	18.3
2.1	2.0	1.6	3.9	5.6	1.8	1.8	3.6	5.1	7.8	6.4	15.3	21.6
2.4	2.5	2.3	4.9	6.9	1.9	1.5	3.7	5.3	8.1	7.7	15.8	22.3
2.7	1.9	1.6	3.7	5.2	2.3	2.0	4.5	6.4	8.4	5.9	16.5	23.4
3.0	2.3	1.8	4.4	6.3	1.8	1.6	3.6	5.1	6.5	5.6	12.7	17.9

Table 2-4. Repeatability of cone density, nearest neighbor distance (NND), and number of neighbors regularity (NoNR) for different eccentricities computed along the nasal meridian for confocal images

	Density				NND				NoNR			
Eccentricity (mm)	**S_w (%)**	**CV (%)**	**ME (%)**	**CR (%)**	**S_w (%)**	**CV (%)**	**ME (%)**	**CR (%)**	**S_w (%)**	**CV (%)**	**ME (%)**	**CR (%)**
0.3	1.8	1.5	3.6	5.1	3.0	2.6	5.9	8.3	8.3	7.6	16.2	22.9
0.6	2.4	2.3	4.8	6.7	2.1	2.1	4.2	5.9	7.3	6.6	14.4	20.3
0.9	2.9	2.7	5.6	7.9	3.0	2.8	5.9	8.4	7.3	5.5	14.4	20.3
1.2	3.1	2.9	6.1	8.6	2.8	2.4	5.6	7.9	8.8	7.5	17.2	24.3
1.5	3.0	2.9	5.9	8.3	2.6	2.3	5.2	7.3	6.6	5.2	12.9	18.2
1.8	3.2	2.8	6.3	8.9	2.5	1.9	4.8	6.8	6.6	5.8	13.0	18.4
2.1	3.3	2.9	6.4	9.1	2.6	2.0	5.2	7.3	9.1	7.9	17.9	25.3
2.4	4.0	3.2	7.9	11.2	2.6	2.3	5.1	7.3	7.7	6.6	15.0	21.2
2.7	2.9	2.9	5.8	8.2	2.8	2.3	5.5	7.7	8.7	8.0	17.1	24.1
3.0	2.8	2.7	5.5	7.7	2.7	2.5	5.4	7.6	5.2	4.3	10.2	14.5

Table 2-5. Repeatability of cone density, nearest neighbor distance (NND), and number of neighbors regularity (NoNR) for different eccentricities computed along the nasal meridian for split-detector images

	Density				NND				NoNR			
Eccentricity (mm)	**S_w (%)**	**CV (%)**	**ME (%)**	**CR (%)**	**S_w (%)**	**CV (%)**	**ME (%)**	**CR (%)**	**S_w (%)**	**CV (%)**	**ME (%)**	**CR (%)**
0.3	1.9	1.9	3.7	5.2	2.9	2.2	5.8	8.2	8.7	8.1	17.0	24.0
0.6	2.0	1.9	3.9	5.6	2.1	1.6	4.0	5.7	7.8	6.9	15.2	21.5
0.9	2.6	2.5	5.1	7.2	2.6	2.0	5.2	7.3	8.1	6.8	15.9	22.5
1.2	2.5	2.4	4.9	7.0	2.5	1.9	4.9	6.9	8.3	6.4	16.4	23.1
1.5	2.2	1.9	4.3	6.1	2.1	1.8	4.1	5.8	5.6	4.4	10.9	15.4
1.8	2.3	2.1	4.5	6.4	2.3	1.8	4.5	6.4	7.4	6.6	14.5	20.5
2.1	2.3	2.2	4.5	6.4	2.3	1.9	4.5	6.4	7.0	5.9	13.8	19.5
2.4	2.3	1.9	4.6	6.4	2.4	1.5	4.6	6.5	6.8	6.2	13.4	18.9
2.7	1.9	1.8	3.9	5.5	2.2	1.9	4.3	6.0	8.3	5.9	16.2	22.9
3.0	1.8	1.5	3.6	5.1	2.3	2.0	4.6	6.5	5.6	4.2	11.0	15.6

Table 2-6. Repeatability of cone density, nearest neighbor distance (NND), and number of neighbors regularity (NoNR) for different eccentricities computed along the superior meridian for confocal images

	Density				NND				NoNR			
Eccentricity (mm)	**S_w (%)**	**CV (%)**	**ME (%)**	**CR (%)**	**S_w (%)**	**CV (%)**	**ME (%)**	**CR (%)**	**S_w (%)**	**CV (%)**	**ME (%)**	**CR (%)**
0.3	2.4	2.2	4.6	6.5	2.9	2.2	5.8	8.2	7.5	6.2	14.7	20.8
0.6	2.7	2.5	5.4	7.6	2.8	2.2	5.5	7.7	7.2	6.6	14.1	19.9
0.9	3.0	2.8	5.9	8.4	2.7	2.3	5.3	7.5	8.1	8.0	15.8	22.4
1.2	3.0	2.7	5.9	8.5	2.6	2.5	5.1	7.2	9.9	8.9	19.5	27.6
1.5	3.9	2.9	7.8	10.9	2.5	1.9	4.9	6.9	4.9	4.6	9.6	13.6
1.8	4.1	3.3	8.1	11.5	2.6	2.4	5.1	7.2	7.1	5.8	14.0	19.6
2.1	3.3	3.3	6.6	9.3	2.9	2.6	5.8	8.1	7.2	5.2	14.2	20.0
2.4	3.2	2.7	6.3	8.9	2.7	2.6	5.2	7.4	8.6	7.5	16.8	23.7
2.7	2.9	2.8	5.8	8.1	3.0	2.1	5.9	8.4	6.5	5.5	12.8	18.1
3.0	3.4	3.0	6.7	9.5	2.8	2.3	5.6	7.9	9.1	7.2	17.9	25.3

Table 2-7. Repeatability of cone density, nearest neighbor distance (NND), and number of neighbors regularity (NoNR) for different eccentricities computed along the superior meridian for split-detector images

	Density				NND				NoNR			
Eccentricity (mm)	**S_w (%)**	**CV (%)**	**ME (%)**	**CR (%)**	**S_w (%)**	**CV (%)**	**ME (%)**	**CR (%)**	**S_w (%)**	**CV (%)**	**ME (%)**	**CR (%)**
0.3	2.4	2.3	4.8	6.7	2.3	2.0	4.6	6.5	8.7	8.2	17.1	24.2
0.6	2.7	2.6	5.3	7.5	2.6	1.9	5.1	7.2	7.8	6.9	15.3	21.6
0.9	2.5	2.1	4.8	6.8	2.2	2.0	4.4	6.2	6.7	5.56	13.2	18.7
1.2	2.7	2.4	5.3	7.5	1.7	1.6	3.3	4.7	10.7	10.1	21.0	29.7
1.5	2.3	2.2	4.6	6.5	2.2	1.6	4.4	6.2	4.5	4.0	8.8	12.5
1.8	2.2	1.7	4.3	6.1	2.0	1.7	3.9	5.6	7.4	5.7	14.5	20.5
2.1	2.4	1.9	4.7	6.6	2.3	1.9	4.4	6.3	8.6	7.7	16.9	23.8
2.4	2.4	1.9	4.7	6.6	1.8	1.6	3.5	4.9	8.3	6.8	16.2	22.9
2.7	2.4	2.4	4.6	6.5	1.9	1.6	3.7	5.2	7.2	6.3	14.2	20.0
3.0	2.8	2.6	5.5	7.8	2.3	2.2	4.5	6.3	8.8	8.1	17.3	24.4

Table 2-8. Repeatability of cone density, nearest neighbor distance (NND), and number of neighbors regularity (NoNR) for different eccentricities computed along the temporal meridian for confocal images

	Density				NND				NoNR			
Eccentricity (mm)	**S_w (%)**	**CV (%)**	**ME (%)**	**CR (%)**	**S_w (%)**	**CV (%)**	**ME (%)**	**CR (%)**	**S_w (%)**	**CV (%)**	**ME (%)**	**CR (%)**
0.3	2.0	1.8	4.0	5.7	2.5	1.9	4.9	7.0	9.5	7.7	18.6	26.3
0.6	2.1	1.9	4.2	5.9	2.5	1.7	4.9	6.9	8.2	6.7	16.2	22.9
0.9	2.9	2.5	5.8	8.3	2.7	2.3	5.3	7.5	11.0	10.2	21.6	30.6
1.2	3.3	2.9	6.4	9.1	3.0	2.6	5.9	8.4	10.9	9.7	21.5	30.4
1.5	3.2	2.9	6.2	8.8	2.6	2.1	5.1	7.2	6.2	5.0	12.2	17.2
1.8	3.5	3.1	6.8	9.6	2.5	2.4	4.9	6.9	5.8	4.8	11.4	16.1
2.1	3.9	3.1	7.8	10.9	2.3	1.9	4.5	6.3	8.9	7.3	17.5	24.7
2.4	3.3	3.2	6.5	9.1	2.3	1.9	4.4	6.2	7.3	5.2	14.4	20.3
2.7	3.2	3.0	6.2	8.8	1.9	1.2	3.7	5.2	5.4	4.1	10.6	14.9
3.0	3.2	2.9	6.3	8.9	2.2	2.0	4.2	6.0	6.2	5.4	12.2	17.2

Table 2-9. Repeatability of cone density, nearest neighbor distance (NND), and number of neighbors regularity (NoNR) for different eccentricities computed along the temporal meridian for split-detector images

	Density				NND				NoNR			
Eccentricity (mm)	**S_w (%)**	**CV (%)**	**ME (%)**	**CR (%)**	**S_w (%)**	**CV (%)**	**ME (%)**	**CR (%)**	**S_w (%)**	**CV (%)**	**ME (%)**	**CR (%)**
0.3	2.1	1.7	4.1	5.8	2.4	2.1	4.7	6.6	10.9	9.2	21.3	30.0
0.6	2.0	1.7	4.0	5.7	2.5	1.8	4.8	6.8	8.1	7.1	15.8	22.3
0.9	2.4	1.9	4.7	6.6	2.6	2.3	5.0	7.1	11.4	10.4	22.3	31.6
1.2	2.0	1.9	3.9	5.6	2.7	2.3	5.3	7.4	9.5	7.9	18.6	26.3
1.5	2.2	1.8	4.2	5.9	1.9	1.7	3.8	5.4	6.7	5.9	13.1	18.5
1.8	1.9	1.3	3.7	5.3	1.9	1.5	3.9	5.5	4.8	3.7	9.4	13.3
2.1	2.4	1.8	4.7	6.6	1.7	1.4	3.4	4.8	5.5	4.6	10.8	15.3
2.4	2.2	2.1	4.3	6.0	1.6	1.4	3.2	4.6	5.8	4.8	11.4	16.1
2.7	2.4	2.6	4.6	6.5	1.6	1.4	3.1	4.4	5.4	4.4	10.6	15.0
3.0	2.1	1.9	4.1	5.8	1.4	1.1	2.7	3.8	6.9	5.5	13.6	19.2

2.4 Discussion

The main purpose of this study was to determine the repeatability of quantifying cone photoreceptor packing metrics from confocal and split-detector AOSLO images acquired in healthy, adult eyes over a 12 month period. We also sought to better describe the level of agreement between confocal and split detector images of the same patch of retina. The data from baseline images showed that there were no significant differences in values of cone density and NND generated from corresponding confocal and split-detector images. However, NoNR was significantly different between these 2 modalities for peripheral eccentricities. For the longitudinal analysis, cone density and NND were not significantly different between baseline and 12-month time points for any eccentricity, whereas NoNR was significantly different for one peripheral eccentricity. The average coefficients of repeatability for cone density, NND, and NoNR were 8.42%, 7.17%, and 21.86% for confocal images and 6.29%, 6.10% and 21.07% for split-detector images.

Very good structural correspondence was observed between confocal and split detector images of the same retinal locations across eccentricities. Bright structures in the confocal images often corresponded well with the 'mound-like' structures in the split detector images. While no significant differences were noted in cone metrics between confocal and split detector images across eccentricities, density measurements tended to be higher and spacing measurements tended to be lower in confocal images relative to measurements over the same areas in the corresponding split detector images. The contrast of the cones in the confocal images is higher in locations closer to the foveal center, making it easier to identify and mark cones at these eccentricities relative to the split detector images. At more peripheral locations, possibly due to the multi-modal nature of cones and the presence of other structures like rods and RPE, there is increased variability in the appearance of light that is directly back-scattered from cones in the confocal signal (Figure 2-12). Given the large infiltration of rods in the periphery, this increased variability in the confocal signal can make it challenging to properly

distinguish cones from rods and increase the variability in measurements of cone metrics using confocal images. None of these phenomena are present in split detector images, resulting in more consistent identification and marking of cones which, in turn, results in decreased variability in cone metric measurements. As seen in our data (Tables 2-9), the average measures of repeatability for cone density were higher for confocal images compared to the split detector images for more peripheral eccentricities (1.5mm – 3.0mm). These repeatability values for confocal images were also higher at these more eccentric locations compared to more central locations.

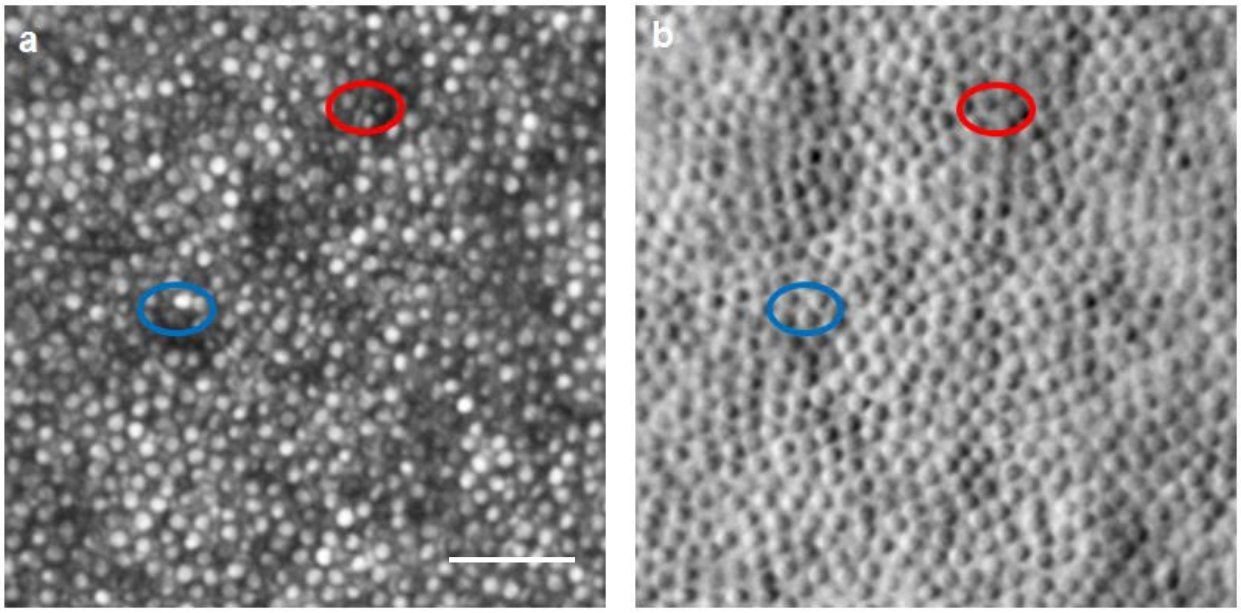

Figure 2-12. Cones can be clearly resolved in AOSLO split detector images at locations that are challenging to interpret in AOSLO confocal images. (a) Cones in an AOSLO confocal registered image taken at an eccentricity of 2.1 mm. Locations can be noted in the confocal image where it is unclear whether the structure being observed contains rods or cones (red circle). In addition, cones can vary substantially in their brightness and uniformity (blue circle), making it challenging to identify and mark cones in confocal images, particularly at more peripheral locations. (b) AOSLO split detector image of the same retinal patch is in (a). Cones can clearly be resolved in locations that are challenging to identify as cones in the confocal image. (Scale: 50 μm)

Of the three cone metrics analyzed in this study, repeatability was the best for NND and was worst for NoNR. Also, density and NND were not significantly different between the two modalities or between the two time-points. However, NoNR was significantly different between confocal and split-detector modalities and between the baseline and 12-month time points. These results are consistent with those published by Cooper et al. (2016) who showed that NND is a robust metric that is least sensitive to change, while NoNR is a metric that is very sensitive to change**.** Therefore, undersampling the cone mosaic within an ROI will have a larger effect on NoNR than on density and NND. The average coefficient of repeatability value of NND found in this study was 7.17%, which is greater than expected, potentially due to our manual intervention in marking cones. NND can be sensitive to the location at which the cone centroid is marked and manual markings may not precisely coincide with the very center of a cone. The average NND across all locations is approximately 7µm, 7% of which is 0.5 µm, or approximately 0.64 pixels. Therefore, a manual change in the marking of the center of a cone by 1 pixel relative to where it was marked at baseline would be larger than this mean value and alter the repeatability measurement.

The measures of repeatability found in this study potentially represent an upper bound on what one might expect to see for longitudinal imaging in healthy eyes. In this study, full frame images were aligned between time points using simple linear shifts in the lateral dimensions (i.e., moving the image from one time point up/down and left/right with respect to the image from the other time point). We did not account for any other differences between images, such as those due to cyclotorsion or shear. More refined registration and alignment techniques could be employed to improve upon the accuracy with which images were co-registered between time points in this study. For example, a strip registration technique could be employed to more finely align strips of an image from one-time point with the image from a different time point, thereby minimizing differences that could occur between image due to shear or the selection of a slightly difference reference frame between time points. One could also apply an affine transformation

on images from one time point, as done by Jackson et al (2019), to minimize differences due to effect such as shear, cyclotorsion, or image magnification between time points. Finer refinements would likely lead to improved values for repeatability and could be the topic of future examination.

We chose to use two different ROI sizes for analyzing cone metrics. Though many studies have used different ROI sizes and varying strategies for defining the size of an ROI (Morgan et al., 2014; Song et al., 2011; Li et al., 2010), we used ROI sizes with areas that were equivalent to those used by Curcio et al. (1990) for easier comparison to histological data. A smaller ROI size (37 μm × 37 μm) was used for eccentricities closest to the foveal center (0.3mm to 1.2mm) where cones are known to change most rapidly, as the use of a large ROI size would include cones with a large gradient in their density and spacing and potentially lead to decreased accuracy. Conversely, a larger ROI size (100 μm × 100 μm) was used at more eccentric locations (i.e., eccentricities of 1.5 mm and beyond) as cones tend to have increased spacing. The use of too small an ROI size could lead to an undersampling of cones within the ROI that would subsequently result in increased variability in the measurements of cone geometry.

One potential source of error and variability when quantifying cone metrics across a large range of eccentricities could result from scaling differences due to changes in the eye's axial length. Axial length is not constant for all angles and retinal eccentricities. An ideal approach would be to measure axial length for each retinal eccentricity and laterally scale each retinal image based on its specific axial length. While not exact, we do not believe that the use of a single axial length measurement for all eccentricities in this study (1° to 10°, or approximately 0.3 mm to 3 mm) significantly impacted our measurements. Based on work performed by Mallen & Kashyap (2007), there is only a 0.4% mean difference between the axial length measured at 0.6˚ compared to that measured at 12° in healthy adult eyes. This mean

difference represents a 0.10 mm difference across 12° of eccentricity for an eye with an axial length of 24 mm.

The program we used to automatically mark the centers of the cones was more accurate and efficient for confocal images at more central locations (relative to more peripheral locations). Consequently, increased manual intervention was needed for more peripherally-located ROIs. In addition, the program (at this time) was not developed to work for split-detector images. Therefore, despite our best efforts to acquire automated cone markings for split detector images, we had to manually mark most of the split detector images. This increased manual marking could lead to increased variability in cone metrics relative to the use of an algorithm that was developed to be robust for analyzing for split detector images.

Other factors can also contribute to small differences in cone metrics within the same eyes over time. Cones in confocal images change in their brightness over time, even in healthy eyes. A study by Pallikaris et al. (2003) that examined changes in the reflectance of cones over a 24-hour period illustrated that cones can vary quite considerably in the rate at which their brightness changes over time, with some having short time constants and others having long time constants. Therefore, a cone that appears bright in a confocal image for one imaging session is likely to have a much different intensity at a subsequent imaging session, making it challenging to follow the same cone over time in a healthy eye. In addition, the selection of a reference frame that serves as the basis for generating a registered image is very important for yielding consistent images between imaging sessions. Selecting a reference frame that contains any form of sheer or eye motion will compromise the integrity of the cone mosaic and lead to a different appearance of a particular set of cones. Also, our algorithm does not currently take into account the fact that the eye can undergo small amounts of cyclotorsion between time points. Currently, the program we use to compensate for eye motion within and between imaging frames only corrects for translational movements (x and y directions), but cannot correct for the

rotational movements. Increased variability could be noted in a measurement taken at a subsequent time point if an ROI is slightly rotated with respect to the initial time point.

The use of split detector imaging in conjunction with confocal imaging is very valuable and provides additional information. Quantifying multiple metrics (in addition to cone density) is necessary to provide a more complete picture of photoreceptor packing. The repeatability data quantified for both modalities and different metrics can serve as a baseline data for future studies in healthy and diseased eyes. To better quantify the cone mosaic geometry metrics we recommend using confocal images for the central locations and split detector images for more eccentric locations. Other factors, including the size of the ROIs used or the technique for marking cones within an ROI, may also affect cone quantification and will be explored in subsequent chapters.

2.5 Acknowledgements

This work was supported by Student Vision Research Support Grant (sVRSG) from the University of Houston College of Optometry. The authors would also like to thank Dr. Julia Benoit for helpful discussion on statistics.

CHAPTER 3

Evaluating methods for marking cones in simulated and *in vivo* retinal images

Contributing Authors:

Hope M. Queener M.S., Gwen Musial Ph.D., Hanieh Mirhajianmoghadam M.S., Joseph Carroll PhD., Jason Porter Ph.D.

3.1 Introduction

Adaptive optics (AO) imaging is a powerful tool used to noninvasively examine the retina *in vivo* on a cellular scale. An increasing number of studies have calculated metrics of cone photoreceptor packing (e.g., cone density and spacing) in healthy and diseased eyes from *in vivo* AO images (Chui et al., 2008; Hofer et al., 2005; Rossi & Roorda, 2010; Li et al., 2010; Talcott et al., 2011). However, no standardized approach has yet been recommended for marking cones in AO images. Consequently, different methods have been used to identify and mark cones in AO images from living eyes (Li & Roorda, 2007; Song et al., 2011; Xue et al., 2007) with little knowledge of whether different marking techniques can result in different values of cone metrics. It is important to better understand the impact of different image processing and analysis methods on the accuracy of cone packing measurements. Such information could also better facilitate the comparison of measurements made across different studies.

A very common method used to quantify cell packing in histological studies is to mark and include all cells that lie along two adjacent edges of a square bounding the area, or region of interest (ROI), being analyzed, regardless of whether they are completely within the ROI, and not mark cells along the other two edges. However, this method assumes a relatively uniform distribution of cells on each side of the ROI. Such an assumption could be problematic for analyzing cone packing in the retina, where it is well-known that cone density can change rapidly with eccentricity near the fovea (Curcio et al., 1990) and could yield different cell counts on one side of an ROI versus another. Some studies have marked all cones within an ROI regardless of whether a cone is completely contained within the ROI (Liu et al., 2014), while others have marked only cones that are fully contained within the ROI (Lombardo et al., 2013). Many other published studies do not detail their marking criteria. Consequently, the impact of different marking methods on measures of cone packing is not clear.

The purpose of this study was to determine the accuracy of and variability in measurements of cone packing resulting from different cone marking techniques performed on

simulated data with uniform and known densities. A similar analysis was also performed on *in vivo* images of cone photoreceptors acquired at multiple eccentricities in 5 healthy adult eyes using adaptive optics. The findings of this study yield an improved understanding of the impact of marking techniques on cone metrics that can be used to standardize such measurements in future studies, thereby helping to facilitate the comparison of cone packing data across experiments and assist in the development of AO as a clinical tool.

3.2 Methods

Three different techniques were used to mark cone photoreceptors in both simulated images and *in vivo* retinal images. The same algorithm was subsequently used to quantify cone metrics based on the marked cone locations.

3.2.1 Marking simulated images

Marking techniques were first evaluated on simulated cone mosaics with known density and spacing. A custom program (courtesy of Drs. Robert Cooper and Joseph Carroll) was used to create simulated cone mosaics of uniform densities ranging from 10,000 to 200,000 cones/mm^2 (in increments of 10,000 cones/mm^2). The program converted the numerical density value input by the user into a set of circular cones of regular size that were hexagonally packed in a triangular lattice. The relationship between cone spacing (s) and density (D) was calculated as:

$$s = \sqrt{\frac{1}{D \times \cos(30)}} \quad (1)$$

Each simulated cone mosaic had a size of 200 μm × 200 μm. Five square ROIs with a side dimension of 37 μm (Figure 3-1a, red squares) and five square ROIs with a side dimension of 100 μm (Figure 3-1a, yellow squares) were placed at random locations with random orientations within the 200 μm × 200 μm mosaic. ROIs were subsequently extracted from each mosaic.

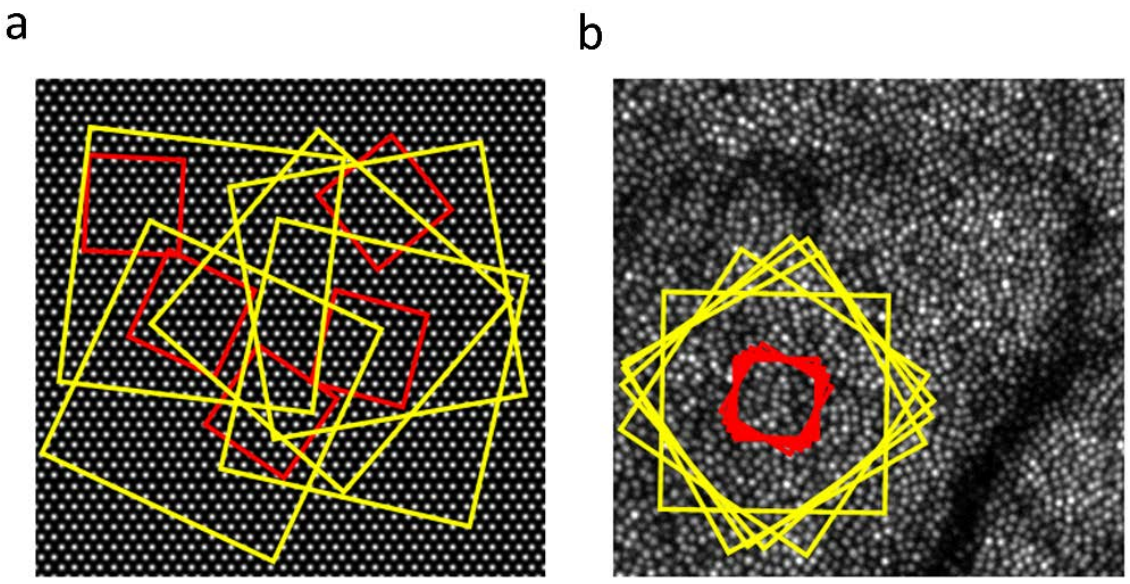

Figure 3-1. Illustration of the process for extracting regions of interest (ROIs) from (a) simulated and (b) *in vivo* human cone mosaics for subsequent analysis. (a) Five 37 µm x 37 µm square ROIs (red squares) and five 100 µm x 100 µm square ROIs (yellow squares) of random orientation were randomly extracted from all simulated mosaics and used to test three methods for marking cones. (b) Five 37 µm x 37 µm square ROIs (red squares) and five 100 µm x 100 µm square ROIs (yellow squares) of random orientation were centered on a given eccentricity and extracted from all *in vivo* human cone mosaics for subsequent examination.

Cones were marked using 3 techniques (Figure 3-2). For each ROI, we marked all cones located fully within the ROI and those that were partially within the ROI along all 4 borders (ALL), along the top and right borders only (TR), and along the bottom and left borders only (BL). A custom, semi-automated program (Mosaic Analytics; Translational Imaging Innovations, Hickory, NC USA) calculated bound and unbound linear cone densities (Cooper et al., 2016) for all ROIs and marking methods:

$$\text{Unbound cone density} = \frac{\text{Number of cones}}{\text{Area of the ROI}} \quad (2)$$

$$\text{Bound cone density} = \frac{\text{Number of bound Voronoi cones}}{\text{Summed area of bound Voronoi cones}} \quad (3)$$

Bound density is defined as the ratio of the number of bound Voronoi cells in an ROI to the summed area of the bound Voronoi cells within the ROI. Unbound density is defined as the total number of cones inside an ROI (regardless of whether a cone is located fully or partially within

the ROI) divided by the total area of the ROI. For each simulated mosaic, density values were averaged across the 5 randomly placed ROIs for both ROI sizes and all marking methods. Calculated values were compared with each other a using 2-way ANOVA that examined the main effects of marking methods and simulated densities, and with known values for each simulated density using a 2-way ANOVA on mean percent error. In addition, mean coefficients of variation (CVs) in cone densities were calculated for each method and ROI size. A P value < 0.05 was considered to be statistically significant.

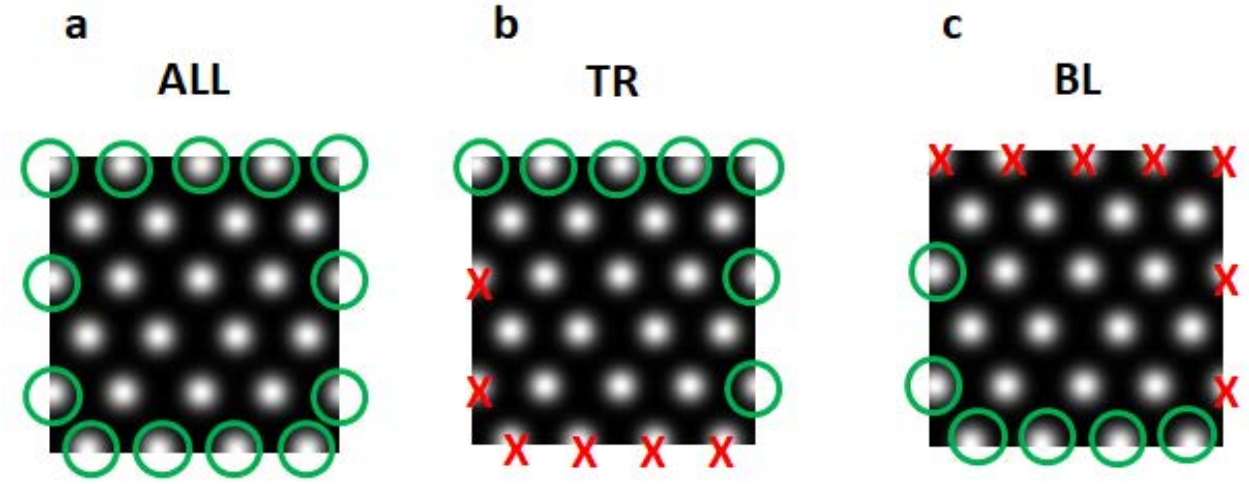

Figure 3-2. Illustration of the three methods used for marking cones in this study. Cones that were partially contained along the border and included in the analysis for the given method are shown using green circles, while excluded cones are shown using a red "x". (a) ALL – All cones located fully or partially within the ROI were marked and included for analysis. (b) TR – Cones located fully within the ROI and those located partially within the ROI along the top and right borders were marked and included for analysis. (c) BL – Cones located fully within the ROI and those located partially within the ROI along the bottom and left borders were marked and included for analysis.

3.2.2 Acquiring and marking in vivo retinal images

Each cone marking technique was also evaluated using *in vivo* data acquired from 5 healthy adult eyes. All study procedures were approved by the Institution Review Board at the University of Houston and adhered to the tenets of the Declaration of Helsinki. Subjects provided informed consent prior to willingly participating in the study after learning about the experimental procedures. The best-corrected visual acuity of each subject was at least 20/20

and subjects had no history of ocular trauma or disease. As described in Chapter 2, measures of ocular biometry were acquired in all eyes (Lenstar; Haag-Streit, Koeniz, Switzerland) and incorporated into a 4-surface model eye to laterally scale adaptive optics scanning laser ophthalmoscope (AOSLO) images.

After being dilating with 1 drop of phenylephrine hydrochloride (2.5%) and 1 drop of tropicamide (1%), the right pupil of each subject was aligned with the optical axis of the adaptive optics scanning laser ophthalmoscope for imaging. A superluminescent diode with a central wavelength of 840 nm (S Series Broadlighter Superluminescent Diode, S-840-B-I-20, Superlum, Carrigtwohill, Ireland; Full Width at Half Maximum = 50 nm) was used for wavefront sensing and reflectance imaging. Aberrations were measured using a Shack-Hartmann wavefront sensor and corrected using a deformable mirror (Hi-Speed DM97-15, ALPAO, Montbonnot-Saint-Martin, France). Confocal and split detector videos of cone photoreceptors were then acquired from the right eyes of all the subjects at a frame rate of 25Hz over a field size of 1.5°. Videos were acquired from the center of the retina (fovea) to approximately 10° from the fovea in all 4 major meridians (Superior, Inferior, Nasal, Temporal). A strip registration process (Stevenson & Roorda, 2005; Dubra & Harvey, 2010) was used to remove eye motion and create registered confocal and split detector images. Montages were constructed by manually stitching images together in Adobe Photoshop (Adobe Systems Inc., San Jose, CA USA).

Five square ROIs with a side dimension of 37 μm (Figure 3-1b, red squares) and five square ROIs with a side dimension of 100 μm (Figure 3-1b, yellow squares) were placed on the real cone mosaics. ROIs were centered at retinal eccentricities of 0.3 mm, 0.6 mm, 0.9 mm, 1.2 mm, and 2.4 mm from the fovea with random orientation and extracted. Cones were marked in each ROI using the same 3 methods previously described and cone packing metrics were calculated using Mosaic Analytics.

3.3 Results

Mean unbound and bound cone density values calculated from simulated cone mosaics using all marking techniques are shown as a function of simulated density for ROI sizes of 37 μm x 37 μm (Figure 3-3a) and 100 μm x 100 μm (Figure 3-3b). The results of a 2-way ANOVA showed that there was a significant interaction between the main effects of simulated density and marking method. For the smaller ROI size of 37 μm x 37 μm, a post-hoc analysis revealed no significant differences in unbound or bound densities between the 3 marking methods for simulated densities of 10,000 and 20,000 cones/mm^2. However, for simulated densities of 30,000 cones/mm^2 and beyond, values of unbound density obtained after marking all cones that were fully and partially contained within the ROI (All) were significantly different ($P<0.05$) than all other bound and unbound density values and marking techniques. For the larger ROI size of 100 μm x 100 μm, a post-hoc analysis revealed no significant differences in unbound or bound densities between the 3 marking methods for simulated densities of 10,000, 20,000, and 30,000 cones/mm^2. For simulated densities of 40,000 cones/mm^2 and beyond, values of unbound density obtained after marking all cones that were fully and partially contained within the ROI (All) were significantly different ($P<0.05$) than all other bound and unbound density values and marking techniques.

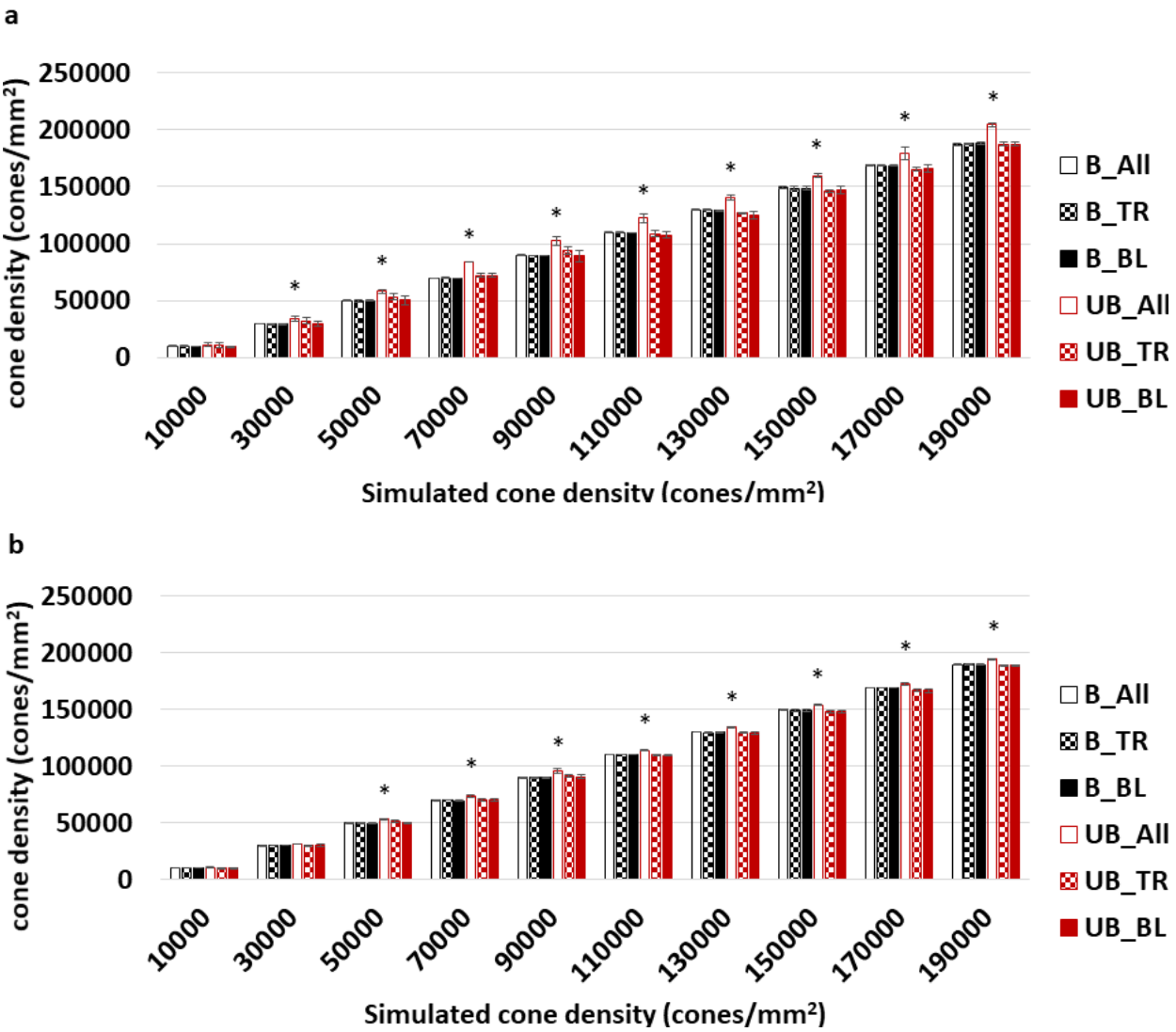

Figure 3-3. Mean values of bound (black) and unbound (red) cone densities for all marking techniques when analyzing simulated mosaics within an ROI size of (a) 37 µm x 37 µm and (b) 100 µm x 100 µm. Error bars represent ± 1 standard deviation. The three techniques consisted of marking all cones completely within the ROI and cones contained partially (1) along all borders (All, open symbol), (2) along only the top and right borders (TR, hatched symbol), and (3) along the bottom and left borders (BL, filled symbol). (a) Unbound cone density values calculated when marking all cones within and along all borders (All, red open symbols) were significantly elevated relative to all other densities and marking techniques for densities above (a) 20,000 cones/mm^2 (*, P<0.05) and (b) 30,000 cones/mm^2 (*, P<0.05) for ROIs with sizes of 37 µm x 37 µm and 100 µm x 100 µm, respectively.

In addition to comparing density values between marking techniques, we compared density values calculated using each technique with known simulated densities. The mean

percent error of the measured density relative to the simulated density was calculated for each simulated density and plotted in Figure 3-4a for an ROI size of 37 μm x 37 μm and in Figure 3-4b for an ROI size of 100 μm x 100 μm.

$$\text{Mean percent error} = \left(\frac{\text{Simulated density} - \text{Measured density}}{\text{simulated density}}\right) * 100 \quad (4)$$

A 2-way ANOVA performed on the mean percent errors for all marking methods across all simulated densities revealed a significant interaction between the main effects of marking method and simulated density ($P<0.001$). For all but the highest simulated density of 200,000 cones/mm^2, the mean percent errors calculated for unbound densities after marking all cones fully and partially contained within the ROI (ALL) were significantly different than the mean percent errors calculated for bound densities ($P<0.05$ for both ROI sizes). A one sample t-test showed that the mean percent errors calculated for unbound densities after marking all cones fully and partially contained within the ROI (ALL) were significantly different from zero for all simulated densities, while the mean percent errors for theunbound densities after marking all cones within and partially along the TR and BL borders were significantly different from zero for most simulated densities ($P<0.05$ for both ROI sizes). The mean percent errors tended to be smaller and less variable when marking cones using any of the three methods and calculating bound cone density compared to calculating unbound density (Table 3-1).

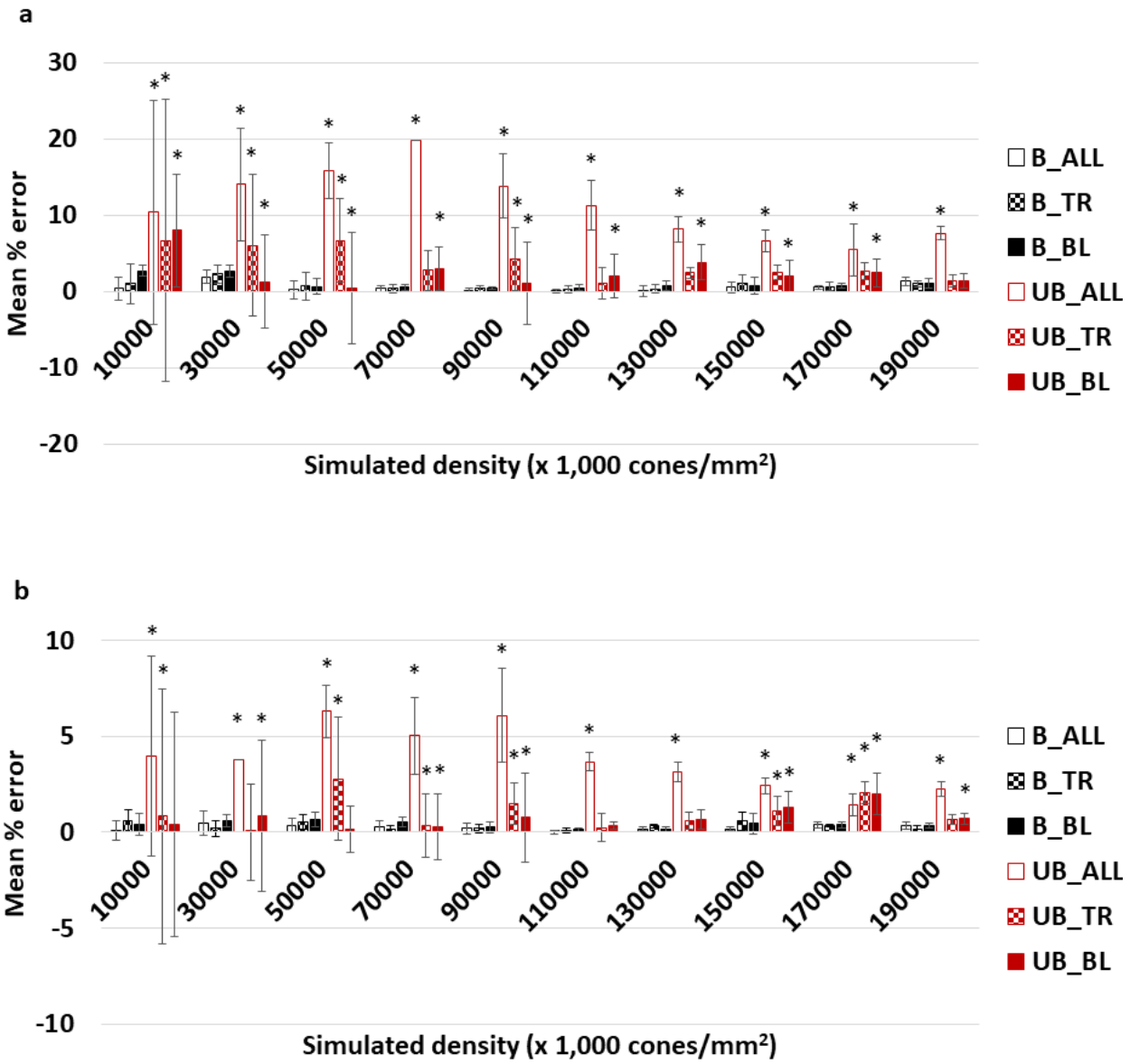

Figure 3-4. (a) Mean percent error in bound (black) and unbound (red) cone density measurements relative to known, simulated values for all marking techniques when analyzing simulated mosaics within an ROI size of (a) 37 µm x 37 µm and (b) 100 µm x 100 µm. Error bars represent ± 1 standard deviation. The three techniques consisted of marking all cones completely within the ROI and cones contained partially (1) along all borders (All, open symbol), (2) along only the top and right borders (TR, hatched symbol), and (3) along the bottom and left borders (BL, filled symbol). Unbound cone density values calculated when marking all cones within and partially along all borders (All, red open symbols) were significantly different from simulated values at nearly all values for both ROI sizes (*, P<0.05).

Table 3-1. Average of mean percent errors across all simulated densities when using different marking methods to assess bound and unbound cone densities from simulated data

	37 μm x 37 μm			100 μm x 100 μm		
	All	TR	BL	All	TR	BL
Bound	0.6 ± 0.5%	0.8 ± 0.5%	1.0 ± 0.6%	0.3 ± 0.2%	0.3 ± 0.2%	0.4 ± 0.2%
Unbound	11.3 ± 4.3%	3.0 ± 2.2%	2.6 ± 1.8%	3.6 ± 1.5%	0.9 ± 0.7%	0.8 ± 0.5%

Bound and unbound cone densities were also calculated from real cone mosaics for each of the three marking methods and compared using a 2-way ANOVA (Figure 3-5). For the smaller ROI size of 37 μm x 37 μm (Figure 3-5a), the results show that there was a significant interaction between the main effects of eccentricity and marking method ($P<0.001$). For an eccentricity of 0.3 mm, unbound density measurements calculated after marking all cones located fully and partially within the ROI (ALL) were significantly higher ($P<0.05$) compared to all other density measurements. Unbound density measurements calculated after marking all cones located fully inside and partially along the top and right borders (TR) or partially along the bottom and left (BL) borders were also significantly different from each other at this eccentricity ($P=0.04$). For all other eccentricities examined, unbound density measurements calculated after marking cones after marking all cones located fully and partially within the ROI (ALL) were significantly higher ($P<0.05$) than all other density measurements and marking techniques.

For the larger ROI size of 100 μm x 100 μm (Figure 3-5b), the interaction between the main effects of eccentricity and marking method was not significant ($P=0.09$). The result also showed that the effect of marking method on density values was significant ($P<0.001$), namely that the unbound density measurements calculated after marking all cones located fully and partially within the ROI (ALL) were significantly higher ($P<0.001$) than all other density measurements and marking techniques.

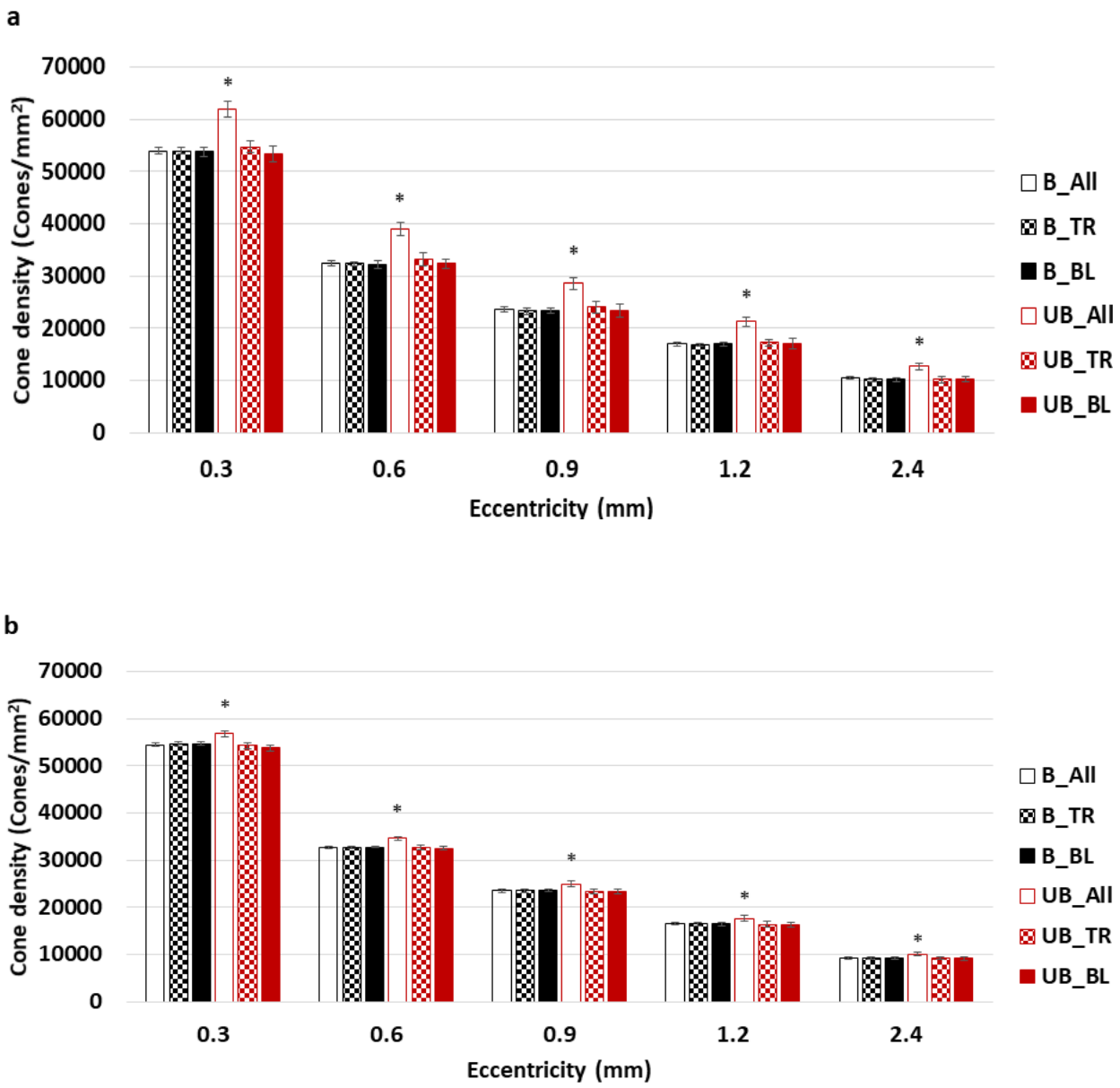

Figure 3-5. Mean values of bound (black) and unbound (red) cone densities for all marking techniques when analyzing *in vivo* cone mosaics within an ROI size of (a) 37 µm x 37 µm and (b) 100 µm x 100 µm. Error bars represent ± 1 standard deviation. The three techniques consisted of marking all cones completely within the ROI and cones contained partially (1) along all borders (All, open symbol), (2) along only the top and right borders (TR, hatched symbol), and (3) along the bottom and left borders (BL, filled symbol). Unbound cone density values calculated when marking all cones within and partially along all borders (All, red open symbols) were significantly elevated relative to all other densities and marking techniques for both ROI sizes across all examined eccentricities (*, $P<0.05$).

The mean coefficients of variation (CVs) in measurements of cone density were also calculated from simulated data (Figure 3-6) and real cone mosaics (Figure 3-7). A one-way ANOVA performed on the coefficient of variation values from the simulated data showed that unbound values were significantly different from bound values across all simulated densities and ROI sizes ($P<0.05$). For in vivo data, a 2-way ANOVA performed on the coefficient of variation values showed that there was no interaction between the main effects of eccentricity and marking method ($P>0.05$). However, there was a significant impact of the marking method on the CV ($P<0.05$). Namely, for *in vivo* data, the CVs for the unbound densities were significantly different than the bound values for both ROI sizes. The CVs in cone density calculated from simulated and *in vivo* images using all marking methods were smaller for bound densities than for unbound densities for both ROI sizes (Tables 3-2 and 3-3).

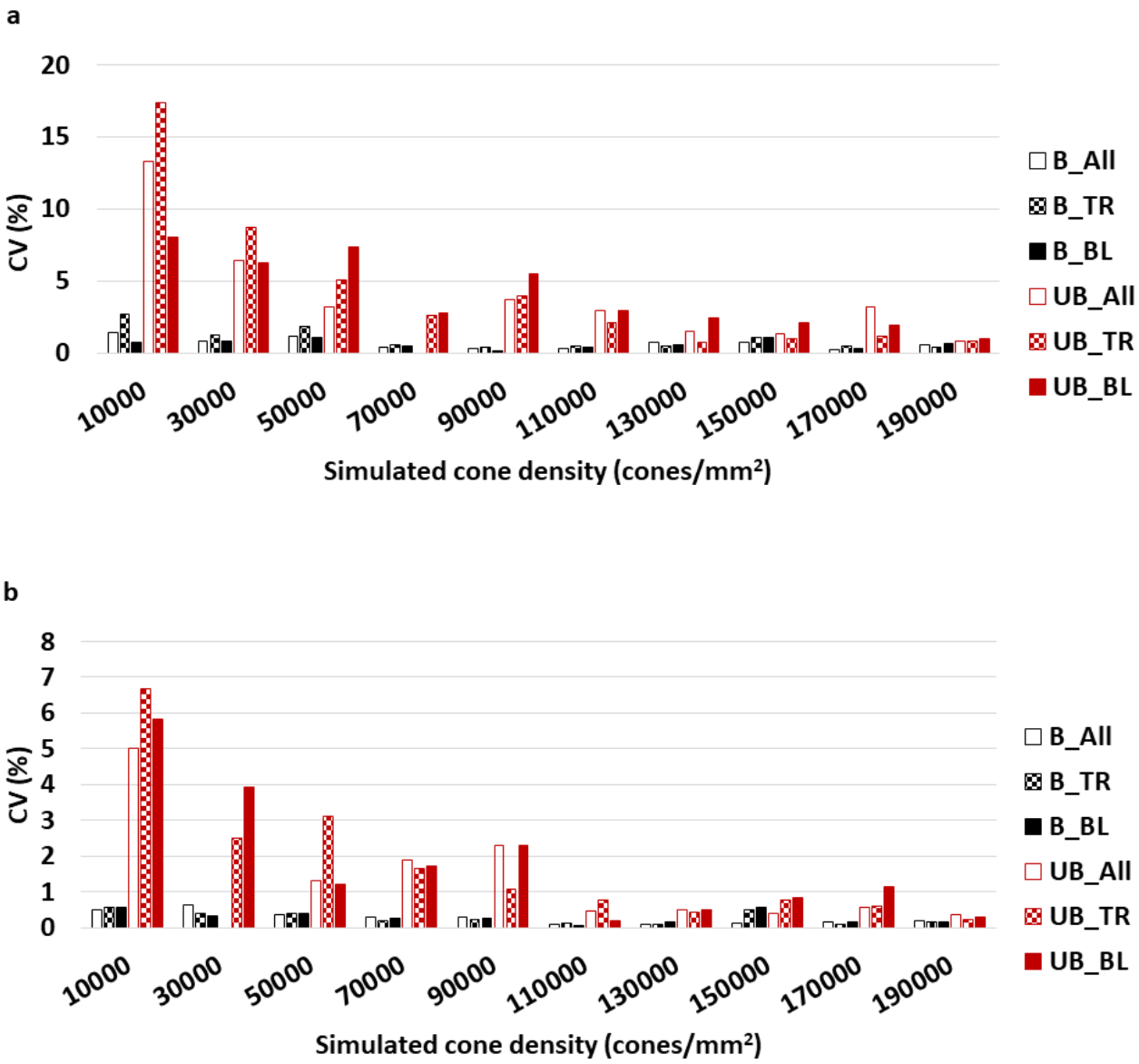

Figure 3-6. Coefficients of Variation (CV) for measurements of bound (black) and unbound (red) cone densities for all marking techniques when analyzing simulated mosaics within an ROI size of (a) 37 µm x 37 µm and (b) 100 µm x 100 µm. CVs are presented as a percentage of the known, simulated density. The three techniques consisted of marking all cones completely within the ROI and cones contained partially (1) along all borders (All, open symbol), (2) along only the top and right borders (TR, hatched symbol), and (3) along the bottom and left borders (BL, filled symbol). CVs for unbound cone densities were significantly different than bound densities across all examined eccentricities, and tended to decrease with increasing simulated density for both ROI sizes (*, $P<0.05$).

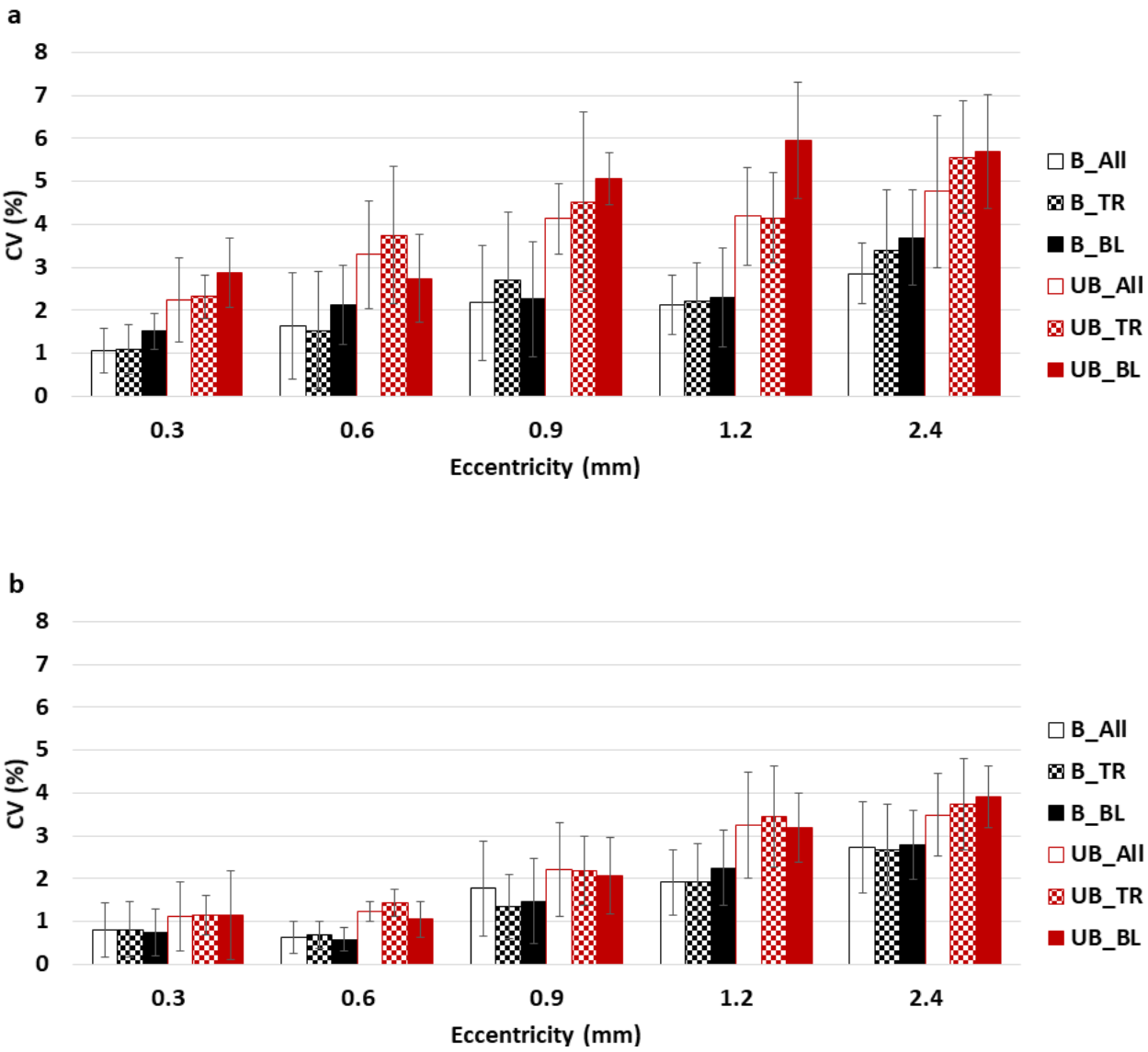

Figure 3-7. Coefficients of Variation (CVs) for measurements of bound (black) and unbound (red) cone densities for all marking techniques when analyzing *in vivo* cone mosaics within an ROI size of (a) 37 µm x 37 µm and (b) 100 µm x 100 µm. CVs are presented as a percentage of the mean density for a given eccentricity. The three techniques consisted of marking all cones completely within the ROI and cones contained partially (1) along all borders (All, open symbol), (2) along only the top and right borders (TR, hatched symbol), and (3) along the bottom and left borders (BL, filled symbol). CVs for unbound cone densities were significantly different from bound densities across all examined eccentricities, and tended to increase with increasing eccentricity for both ROIs (*, $P<0.05$).

Table 3-2. Mean CVs across all simulated densities when using different marking methods to assess bound and unbound cone densities from simulated data

	37 μm x 37 μm			100 μm x 100 μm		
	All	TR	BL	All	TR	BL
Bound	0.7 ± 0.3%	0.8 ± 0.6%	0.7 ± 0.3%	0.2 ± 0.1%	0.2 ± 0.1%	0.2 ± 0.1%
Unbound	3.1 ± 3.0%	3.8 ± 3.9%	3.9 ± 2.4%	1.0 ± 1.1%	1.5 ± 1.5%	1.2 ± 1.4%

Table 3-3. Mean CVs across all analyzed eccentricities when using different marking methods to assess bound and unbound cone densities from *in vivo* data

	37 μm x 37 μm			100 μm x 100 μm		
	All	TR	BL	All	TR	BL
Bound	1.9 ± 0.6%	2.2 ± 0.8%	2.4 ± 0.7%	1.6 ± 0.8%	1.5 ± 0.7%	1.6 ± 0.8%
Unbound	3.7 ± 0.9%	4.1 ± 1.1%	4.5 ± 1.4%	2.3 ± 1.0%	2.4 ± 1.0%	2.3 ± 1.1%

3.4 Discussion

The purpose of this study was to determine the accuracy of and variability in measurements of cone packing resulting from different cone marking techniques performed on simulated data with uniform and known densities and on *in vivo* data from healthy adult subjects. Unbound density measurements for marking all cones located fully within the ROI and those that were partially within the ROI along all 4 borders (ALL) were significantly different ($P<0.05$) from those of bound density measurements. Mean percent errors of unbound densities relative to known, simuluated data when marking all cones located within and partially along all borders of the ROI (ALL) were significantly different ($P<0.05$) from those of bound density measurements. The coefficients of variation for bound densities tended to be smaller than for unbound densities for all marking techniques.

One challenge to establishing adaptive optics as a viable clinical tool is the potential variability of data between studies and across laboratories due to differences in instrumentation and methods for quantification. One specific source of variability could arise from differences in technical procedures used to quantify descriptive metrics, including techniques for marking

cones. Currently, there is a lack of data discussing the potential impact of cone marking techniques on the quantification of cone metrics. We found that metric values can vary substantially, even when analyzed using the same ROI, depending on the metrics being quantified and the methods used for marking cones. Across the marking techniques explored in this study, bound cone density measurements tended to produce values that were most accurate (for simulated data) with the least variability (for both simulated and *in vivo* data).

One difficulty with testing image processing and quantification methods on images of real cone mosaics is the lack of known metric values. Given this difficulty, we first worked with simulated images that had known values of cone density. This approach enabled an estimate of the accuracy and variability of different marking methods before seeing whether the trends observed with the simulated data were also present with the *in vivo* data.

Multiple studies have demonstrated that linear cone density decreases with increasing eccentricity from the foveal center in the healthy retina (Chui et al., 2008; Legras et al., 2018; Song et al., 2011). Given the possibility of needing to measure cone densities over a very wide range of values, we simulated cone mosaics whose densities varied from 200,000 cones/mm^2 (to approximate values that one might expect to measure close to the foveal center) to 10,000 cones/mm^2 (which is a value one might expect to measure at eccentricities of approximately 7-8 degrees). For *in vivo* images, we started our analysis at an eccentricity of 0.3 mm as we were not able to resolve the central-most foveal cones in all subjects. We then sampled the in vivo cone mosaics in 0.3 mm increments until reaching an eccentricity of 1.2 mm, where previous reports have shown that cone density values begin to level out. We also analyzed one more location, at an eccentricity of 2.4 mm, where the density change is much more gradual from the 1.2 mm eccentricity.

We analyzed the impact of different marking techniques on cone densities that were calculated from ROIs of different sizes, as a range of ROI sizes has been used in the literature. An ROI size that has been commonly used for computing cone density data has been a square

ROI with dimensions of 37 μm x 37 μm (or an area of 1,369 μm^2). The area of this ROI size is just slightly larger than the area of the small window size using by Curcio et al. (1990) of 45.4 μm x 29.3 μm (or an area of 1,330 μm^2). Due to the fact that a small ROI size of 37 μm x 37 μm would likely sample few cones when placed at more peripheral eccentricities, we also considered a larger ROI size of 100 μm x 100 μm that has been used as in previous studies (Abozaid et al., 2016; Tanna et al., 2017). Further studies could expand on this work by analyzing other ROI sizes and shapes to increase the breadth of the results found here.

Except for the lowest of simulated densities, measures of unbound cone density following the marking of all cones located fully within and partially along the borders of the ROI were significantly elevated relative to all other density values. A similar pattern was also observed for *in vivo* data, where unbound cone density was significantly higher than all other densities for both ROI sizes when marking all cones within and partially along the ROI borders. In addition, the calculated data was more variable for unbound densities regardless of the method used to mark cones. In general, the coefficient of variation increased with decreasing values of simulated cone density for both ROI sizes, likely due to the fact that the addition/removal of a single cone makes a larger change in the computed density for ROIs containing fewer samples (or lower densities) than for ROIs with a greater number of samples (or higher densities). The same concept can also contribute to the increased variability observed with mean percent error for lower simulated densities.

In conclusion, different cone marking methods have different impacts on the quantification of cone density. We found that computing bound cone density after marking all cones fully and partially within the ROI (ALL) or fully within and partially along 2 adjacent borders of the ROI (TR or BL methods) provides measurements with greatest accuracy and least variability. Based on these findings, we suggest calculating bound cone density after performing marking all cones fully and partially within the ROI (ALL) to provide maximum

sampling, particularly for analyses done at more peripheral eccentricities where cones have increased spacing.

3.5 Acknowledgements

This work was supported by Student Vision Research Support Grant (sVRSG) from the University of Houston College of Optometry and NIH Grant P30 EY007551. We thank Dr. Robert Cooper for providing the custom program to create simulated mosaics.

CHAPTER 4

Evaluating the impact of using different region of interest sizes for quantifying cone metrics from simulated and *in vivo* retinal images

Contributing Authors:

Hope M. Queener M.S., Gwen Musial Ph.D., Hanieh Mirhajianmoghadam M.S., Jason Porter Ph.D.

4.1 Introduction

Adaptive optics (AO) is a technique that measures and corrects for the eye's optical imperfections, thereby increasing the resolution that the eye can detect and the spatial resolution with which retinal features may be imaged. AO has been used to better understand cellular structure in healthy eyes, as well as structural changes in diseased eyes and in eyes following therapeutic interventions (Morgan et al., 2014; Scoles et al., 2014). Different metrics have been used to describe the distribution and arrangement of the photoreceptors. All of the many approaches used to quantify photoreceptor packing start by selecting a retinal area over which photoreceptors are analyzed, typically called the region of interest (ROI). The use of different ROI sizes for analyzing cones makes it challenging to know how to readily compare data between different studies, as changing the size of the ROI could potentially lead to different values of cone metrics.

Several approaches have been used to select an ROI size for analyzing cone packing in living eyes (Table 4-1), with many studies using a fixed ROI size equivalent to the sizes used by Curcio et al. (1990) when analyzing receptor packing in excised retina. While seemingly appealing, the use of a fixed ROI size for all eccentricities could result in variable and erroneous measurements in photoreceptor packing. For example, selecting a large, fixed ROI size that captures a sufficient number of widely spaced cones in the periphery could result in an oversampling of the mosaic near the fovea (i.e., include too many cones in a region where density changes very rapidly) and lead to erroneous measurements (Figure 4-1). Conversely, the selection of a small ROI size may work well to accurately quantify metrics near the fovea at the expense of potentially undersampling the mosaic in the periphery where cones are widely spaced and decreased in their relative numbers per unit area (Figure. 4-2).

Table 4-1. Different ROI sizes used in different studies to quantify cone mosaic geometry metrics

Study	ROI size	Eccentricities
Scoles et al. (2014)	37 × 37 µm	1° to 20°
Song et al. (2011)	50 × 50 µm	0.18 to 3.5 mm (~0.6° to 3.7°)
Morgan et al. (2014)	55 × 55 µm	0.5 and 1.5 mm (~1.6° and 5°)
Lombardo et al. (2013)	60 × 60 µm	1.2° and 1.7°
Jackson et al. (2019)	85 × 85 µm	0.19 to 1.5 mm (~0.6° to 5°)
Abozaid et al. (2016)	100 × 100 µm	0° to 20°
Dees et al. (2011)	0.16° × 0.1° (~48 µm x 30 µm)	0.5° to 3°
Chui et al. (2008)	150 × 150 Pixels (~120 µm x 120 µm)	1° to 10°
Li et al. (2010)	Variable – ROI must contain 150 cones	0° to just beyond 1°

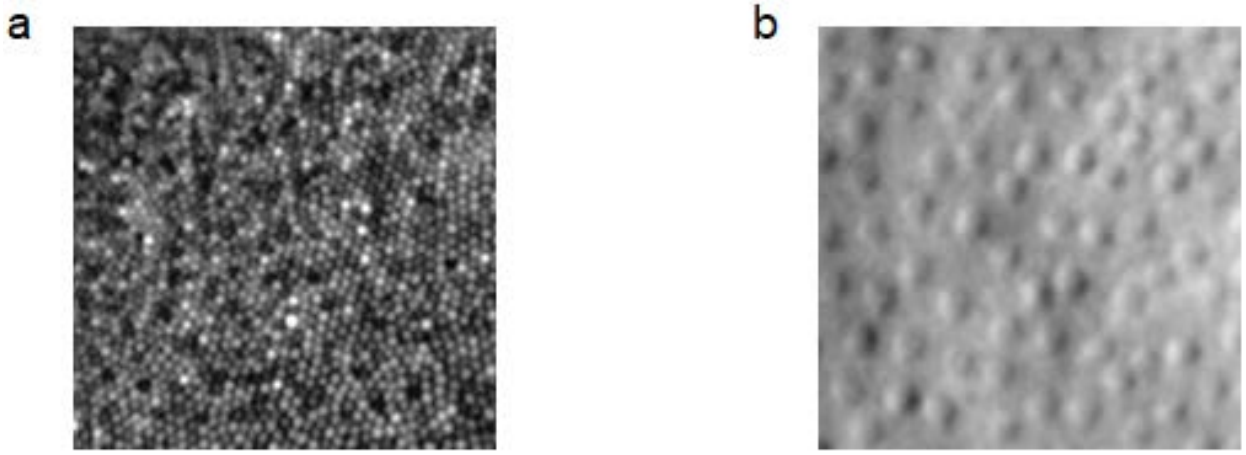

Figure 4-1. Large ROIs extracted from adaptive optics scanning laser ophthalmoscope (AOSLO) images of the cone mosaic from a representative healthy adult eye taken (a) near the foveal center (top left corner of the image) using a confocal imaging channel and (b) at an eccentricity of 10° using a split detector channel. The use of a large, fixed ROI samples a sufficient number of cones in the periphery, but potentially oversamples that number of cones near the foveal center, where density changes rapidly.

Figure 4-2. Small ROIs extracted from adaptive optics scanning laser ophthalmoscope (AOSLO) images of the cone mosaic from a representative healthy adult eye taken (a) near the foveal center (top left corner of the image) using a confocal imaging channel and (b) at an eccentricity of 10° using a split detector channel. The use of a small, fixed ROI size samples a sufficient number of cones near the foveal center, but can dramatically undersample the number of cones in the periphery, where density is lower (and spacing is higher).

Few published studies have examined the impact of changing the size of the region of interest (ROI) used to calculate cone metrics (Garrioch et al., 2012; Lombardo et al., 2014; Zhang et al., 2015). These studies have been limited in the packing metrics that were calculated and the retinal eccentricities examined. Lombardo et al. (2014) investigated the influence of various technical factors on the calculation of cone density at only two eccentricities (1.5° temporal and superior) and concluded that the sampling window (or ROI) size was one of the main factors impacting the quantification of density. Recent work by Zhang et al. (2015) provided a preliminary “optimal” ROI size for calculating cone density, but the method used to determine the “optimal” size was not detailed. Therefore, there is limited knowledge about whether an optimal ROI size exists for use at different eccentricities.

The purpose of this study was to investigate the impact of ROI size on photoreceptor packing measurements using simulated images and *in vivo* images from healthy eyes. We generated simulated images of cone mosaics with gradient densities based on histological reports and collected adaptive optics scanning laser ophthalmoscope (AOSLO) images in healthy eyes. Packing metrics were quantified in simulated and *in vivo* images using 5 ROI sizes, and compared across ROI sizes and with known densities or eccentricity. This experiment provides improved understanding of whether significant differences in metric values exist due to different ROI sizes and potentially provides recommendations on ROI sizes to be used in future studies.

4.2 Methods

The effect of changing ROI size was evaluated on simulated images of the cone mosaic and on in-vivo mosaics acquired from an AOSLO system.

4.2.1 Generating and evaluating simulated cone mosaics

Working with simulated data provides an opportunity to compare calculated data with known density values and minimizes the likelihood of misidentifying cones. For simulated mosaics, a custom program in MATLAB (MathWorks, Natick, MA) was used to generate and simulate a mosaic with a gradient density that was estimated from the data of Curcio et al. (1990) for different eccentricities along the temporal meridian. Density values were then converted to values of cone spacing using the following relationship:

$$s = \sqrt{\frac{1}{D \times \cos(30)}} \quad (1)$$

where 's' is cone spacing (in microns) and 'D' is cone density (in cones/mm^2).

Then, a model was fit to the Curcio data as: $y = a*\log_{10}(x+b)+c$, where y is cone spacing (in microns), x is retinal eccentricity (in mm), b shifts the $\log_{10}$ curve horizontally (so that the log function can cross x = 0), and c shifts the curve vertically (for a minimum cone spacing). Parameter a controls the steepness of the curve. The algorithm of this program then constructs the cone arrangement in expanding hexagonal bands starting from a central cone. As illustrated in Figure 4-3, cones are closely packed at the foveal center (bottom left corner of Figure 4-3) and increase in their spacing as one moves radially away from the center.

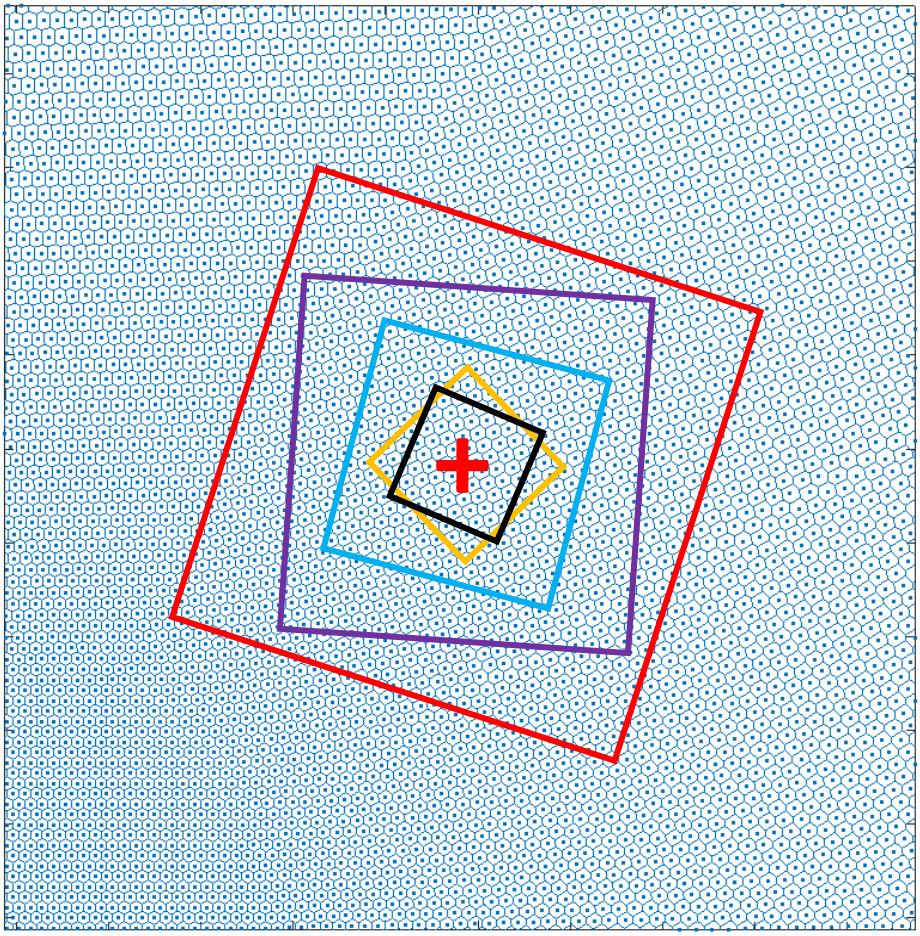

Figure 4-3. A schematic of the cone mosaic as simulated by the custom MATLAB algorithm. Blue dots represent the center of each simulated cone and the surrounding hexagonal structure represents the corresponding Voronoi cell. The foveal center is at the bottom left corner of the image and corresponds to a retinal coordinate of (0°, 0°). Cone density decreases and cone spacing increases with increasing eccentricity radially from the foveal center. The different colored squares overlaid on the simulated mosaic represent square ROIs that were centered at a given eccentricity (red cross) and used to calculate cone density: 25 x 25 µm (black), 37 µm x 37 µm (orange), 50 µm x 50 µm (blue), 75 µm x 75 µm (purple), 100 µm x 100 µm (red).

Large ROIs extracted from adaptive optics scanning laser ophthalmoscope (AOSLO) images of the cone mosaic from a representative healthy adult eye taken (a) near the foveal center (top left corner of the image) using a confocal imaging channel and (b) at an eccentricity of 10° using a split detector channel. The use of a large, fixed ROI samples a sufficient number of cones in the periphery, but potentially oversamples that number of cones near the foveal center, where density changes rapidly.

A hexagon lattice has 6 vertices at intervals of 60° (60°, 120°, 180°, 240°, 300°, and 360°). The first hexagon band constructed by this program has 6 cones; one at each vertex. Each pair of neighboring cones and the center of the lattice form 6 triangles. There are 6 interior band cones and 12 exterior band cones producing 18 vertices (and 18 triangles). Each band has 6 more cones than the prior band. Since the spacing increases with eccentricity, each band is spaced farther along the vertex. However, that increase in spacing along the vertex does not provide enough room for the desired increase in spacing of equilateral triangles along the band. Instead, the cone locations of the next band are calculated algebraically from the positions of the triangle vertices of the prior band and the expected triangle area. This approach results in triangles that tend to be more elongated radially, especially near the 30-degree line. The algorithm does not replicate natural cone arrangements, but rather provides cone density that varies with eccentricity. The hexagonal lattice is mirror symmetric after every 30°. So, instead of generating all of the cone coordinates from 0° to 360°, one can generate cone coordinates from 0° to 30° and reflect those for 30° to 60°. Then, coordinates from 0° to 60° can easily be rotated from 60° to 360° to get the remaining coordinates. The output results of the program are the coordinates of the cone locations.

For the simulated data, five differently sized, square ROIs (with side dimensions of 25 µm, 37 µm, 50 µm, 75 µm, and 100 µm) were centered at each of 21 different eccentricities along the temporal meridian (i.e., at eccentricities of 0.075 mm and from 0.1 mm to 2.0 mm in 0.1 mm increments) (Figure 4-3). Ten ROIs with random orientation were used for each ROI size at each eccentricity. The coordinates of all cones inside each ROI were extracted and used to calculate bound cone density (Cooper et al., 2016).

4.2.2 Evaluating in vivo cone mosaics

The impact of changing the size of the ROI was also evaluated using *in vivo* data acquired from 5 healthy adult eyes. The study was approved by the University of Houston's Institutional

Review Board and adhered to the tenets of the Declaration of Helsinki. Subjects provided informed consent prior to willingly participating in the study after learning about the experimental procedures. The best-corrected visual acuity of each subject was at least 20/20 and subjects had no history of ocular trauma or disease. As described in Chapter 2, measures of ocular biometry were acquired in all eyes (Lenstar; Haag-Streit, Koeniz, Switzerland) and incorporated into a 4-surface model eye to laterally scale adaptive optics scanning laser ophthalmoscope (AOSLO) images.

After being dilating with 1 drop of phenylephrine hydrochloride (2.5%) and 1 drop of tropicamide (1%), the right pupil of each subject was aligned with the optical axis of the adaptive optics scanning laser ophthalmoscope for imaging. A superluminescent diode with a central wavelength of 840 nm (S Series Broadlighter Superluminescent Diode, S-840-B-I-20, Superlum, Carrigtwohill, Ireland; Full Width at Half Maximum = 50 nm) was used for wavefront sensing and reflectance imaging. Aberrations were measured using a Shack-Hartmann wavefront sensor and corrected using a deformable mirror (Hi-Speed DM97-15, ALPAO, Montbonnot-Saint-Martin, France). Confocal and split detector videos of cone photoreceptors were then acquired from the right eyes of all the subjects at a frame rate of 25 Hz over a field size of 1.5°. Videos were acquired from the center of the retina (fovea) to approximately 10° from the fovea in all 4 major meridians (Superior, Inferior, Nasal, Temporal). A strip registration process (Stevenson & Roorda, 2005; Dubra & Harvey, 2010) was used to remove eye motion and create registered confocal and split detector images. Montages were constructed by manually stitching images together in Adobe Photoshop (Adobe Systems Inc., San Jose, CA USA).

Five square ROIs of random orientation for each of the same 5 ROI sizes (with side dimensions of 25 µm, 37 µm, 50 µm, 75 µm, and 100 µm) were placed on *in vivo* cone mosaics at eccentricities ranging from 0.3 - 2.1 mm (in 0.3 mm intervals) along the temporal meridian. Mosaic Analytics (Translational Imaging Innovations, Hickory, NC USA) was used to calculate multiple cone metrics, including density (of the bound Voronoi tessellation), nearest neighbor

spacing, farthest neighbor spacing, inter-cone spacing, number of neighbors' regularity, Voronoi area regularity, inter-cone regularity, and percent six-sided Voronoi (Cooper et al., 2016).

4.2.3 Statistical Analysis

For simulated data, a two-way ANOVA with the main effects of eccentricity and ROI size was preformed to determine whether any differences existed in density measurements between different ROI sizes at all the eccentricities. Mean percent error was calculated for all density measurements and a one-sample t-test was done to determine if the mean percent error values were significantly different from zero. A two-way ANOVA with the main effects of eccentricity and ROI size was performed on coefficient of variation (CV) values for density measurements to determine whether CV values were significantly different for different ROI sizes. Additionally, a linear regression was performed on CV values to investigate possible trends with ROI size.

For *in vivo* data, a two-way ANOVA with the main effects of eccentricity and ROI size was performed on all cone metrics to determine if there were any significant differences in each metric between different ROI sizes at all eccentricities. A two way ANOVA (with the main effects of eccentricity and ROI size was also performed on CV values for cone density determine if there's any difference in CV values between different ROI sizes. A linear regression was also done on CV values for density as a function of eccentricity. Finally, to better understand the relative contributions of the effects of different ROI sizes, eccentricities, and subjects on the total variability of the cone metrics, a variance components analysis was performed to study the random effects of ROI size, eccentricity, and subjects.

4.3 Results

4.3.1 Simulated mosaic density

Mean values of bound cone density computed from simulated data for all ROI sizes across all eccentricities are shown in Figure 4-4. The results of the two-way ANOVA showed a significant

effect of ROI size and eccentricity on cone density ($P < 0.001$ for each variable), with a significant interaction between ROI size and eccentricity ($P < 0.001$). A Tukey post-hoc test revealed that the square ROI with a side dimension of 25 µm yielded values that were significantly different from values calculated when using all other ROI sizes at eccentricities of 0.075 mm, 0.1 mm, and 0.2 mm. Values of bound cone density calculated using different ROI dimensions were not significantly different from each other for all other eccentricities.

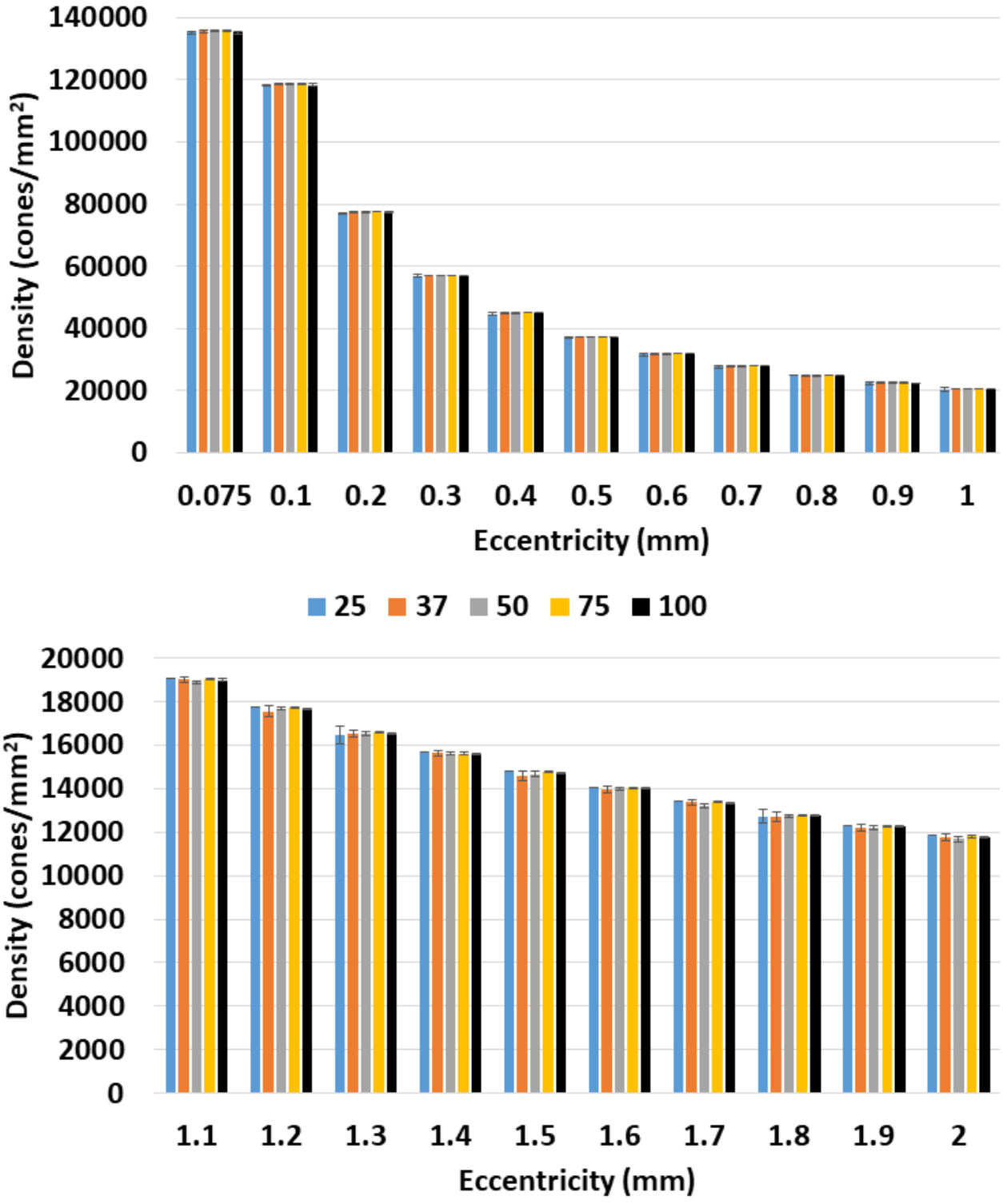

Figure 4-4. Mean values of bound cone density computed from simulated cone mosaics using square ROIs with different side dimensions (blue – 25 µm; orange – 37 µm; gray – 50 µm; yellow – 75 µm; black – 100 µm) as a function of eccentricity. Error bars represent ± 1 standard deviation. Cone density values calculated using the 25 x 25 µm square ROIs (orange) were significantly lower ($P<0.05$) than all other ROI sizes for eccentricities from 0.075 mm to 0.2 mm.

To find out how closely the calculated density values were from known, simulated values, mean percent error was calculated for all the density values using the following equation:

$$\text{Mean percent error} = \left(\frac{\text{true density} - \text{measured density}}{\text{true density}}\right) * 100 \quad (2)$$

Mean percent errors in bound cone density computed from simulated data for all ROI sizes at eccentricities of 0.075 mm, 0.1 mm and 0.2 mm are shown in Figure 4-5. A one sample t-test on the mean percent error data for eccentricities 0.075 mm, 0.1 mm and 0.2 mm showed that mean percent error values were significantly different from zero for all ROI sizes and eccentricities with the exception of the square ROI with a side dimension of 25 μm at eccentricities of 0.075 mm and 0.2 mm ($P = 0.307$ and $P = 0.376$, respectively). The mean percent errors for the ROI size of 25 μm x 25 μm at these two eccentricities were 0.18 ± 0.31% and 0.12 ± 0.40%, respectively.

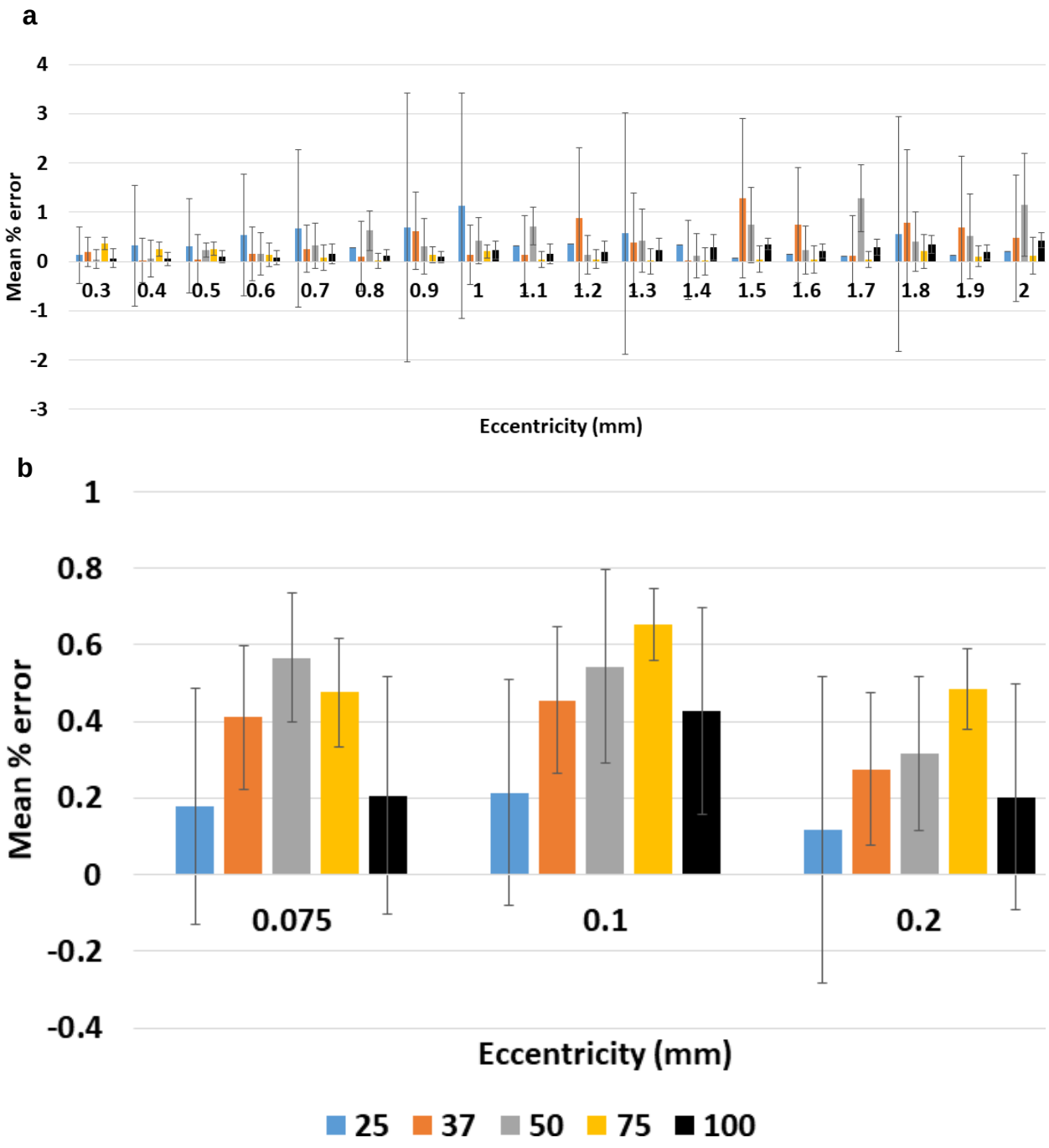

Figure 4-5. Mean percent errors in bound cone density computed from simulated cone mosaics using square ROIs with different side dimensions (blue – 25 μm; orange – 37 μm; gray – 50 μm; yellow – 75 μm; black – 100 μm) as a function of eccentricity. Error bars represent ± 1 standard deviation. (a) Mean percent errors across all eccentricities. (b) Mean percent errors only for 3 of the eccentricities presented in (a): 0.075 mm, 0.1 mm, and 0.2 mm. Mean percent errors were not significantly different from zero for an ROI size of 25 μm x 25 μm at eccentricities of 0.075 mm and 0.2 mm.

Coefficients of Variation (CVs) in bound cone density for simulated images are shown in Figure 4-6 for all 5 ROI sizes at each examined eccentricity. A two-way ANOVA with the main

effects of ROI size and eccentricity was performed on this CV data and showed no significant interaction ($P > 0.05$). The CVs of bound cone density measurements for ROIs with sizes of 25 µm x 25 µm and 37 µm x 37 µm were significantly greater than for ROIs with sizes of 75 µm x 75 µm and 100 µm x 100 µm ($P < 0.05$). Across eccentricities, mean CVs of cone density measurements for smaller ROIs were 0.9 ± 1.1% and 0.8 ± 0.5% for 25 and 37µm compared to 0.2 ± 0.1% and 0.2 ± 0.1% for 75 and 100µm.

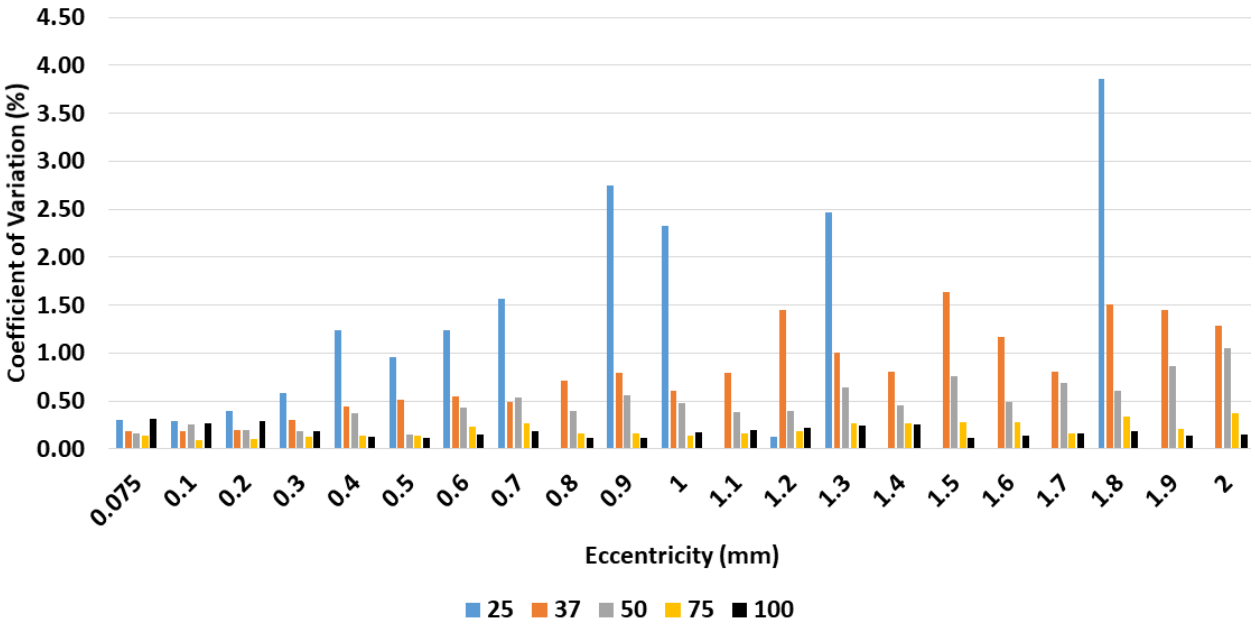

Figure 4-6. Coefficient of variation in bound cone density computed from simulated cone mosaics using square ROIs with different side dimensions (blue – 25 µm; orange – 37 µm; gray – 50 µm; yellow – 75 µm; black – 100 µm) as a function of eccentricity. CV values for ROIs with a side dimension of 25 µm and 37 µm were significantly greater than for ROIs with a side dimension of 75 µm and 100 µm ($P < 0.05$).

The CVs in bound cone density averaged across eccentricities for ROI sizes with side dimensions of 37 µm, 50 µm, 75 µm, and 100 µm are shown in Table 4-2. An ROI with a side dimension of 25 µm was not included as this ROI size yielded a value for CV of zero at multiple eccentricities (as seen in Figure 4-6), due to an insufficient sampling of cones at these more peripheral eccentricities. A linear regression performed on these CV values across different eccentricities showed that the CV increased significantly with an increase in eccentricity for

ROIs with a side dimension 37 μm (R^2 = 0.61), 50 μm (R^2 = 0.74), and 75 μm (R^2 = 0.55) ($P < 0.05$).

Table 4-2. Mean values for the Coefficients of Variation in bound cone density when averaged across all eccentricities from simulated images for different ROI sizes.

ROI Sizes	37 x 37 μm	50 x 50 μm	75 x 75 μm	100 x 100 μm
Average	0.77	0.48	0.20	0.18
SD	0.48	0.23	0.08	0.05

4.3.2 In vivo cone metrics

Mean values of bound cone density are presented in Figure 4-7 for each ROI size across all examined eccentricities. Consistent with previous reports, cone density decreased with increasing eccentricity. A two-way ANOVA performed on the *in vivo* density data showed that there was no significant interaction between ROI size and eccentricity (P = 0.99). In addition, there were no significant differences in density values calculated between different ROI sizes for any eccentricity (P = 0.33).

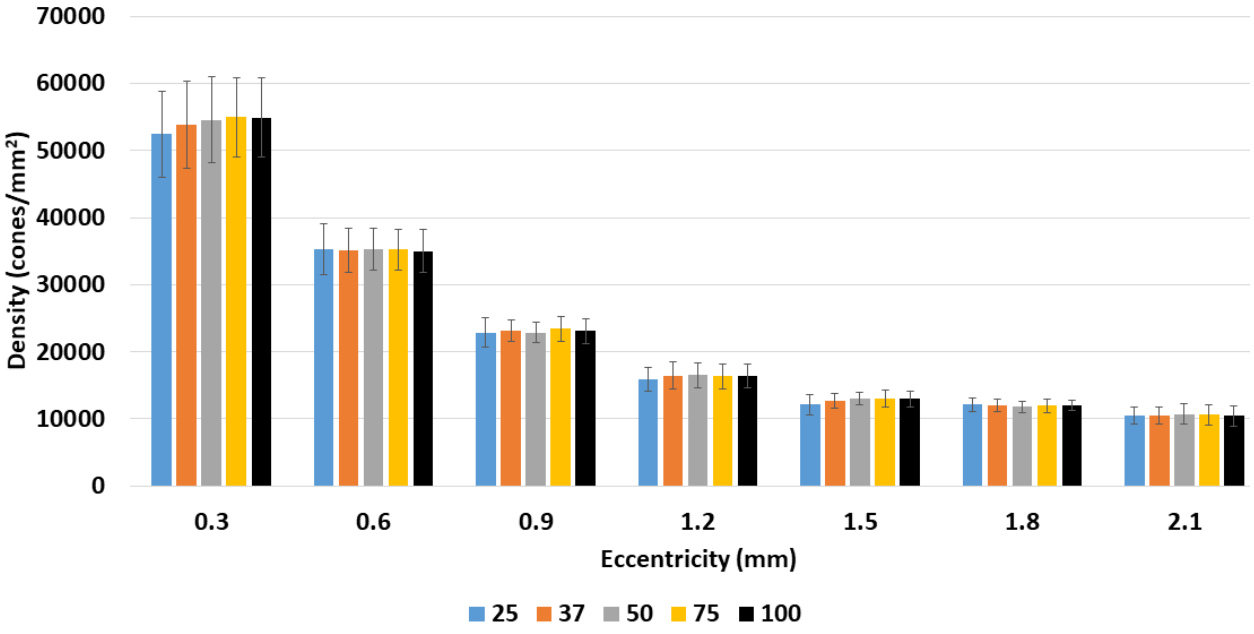

Figure 4-7. Mean values of bound cone density computed from *in vivo* cone mosaics using square ROIs with different side dimensions (blue – 25 μm; orange – 37 μm; gray – 50 μm; yellow – 75 μm; black – 100 μm) as a function of eccentricity. Error bars represent ± 1 standard deviation about the mean across subjects. Values of cone density calculated for each ROI size were not significantly different from each other at any eccentricity (P>0.05).

Mean CVs in bound cone density calculated across subjects are plotted in Figure 4-8 for all examined eccentricities. A linear regression performed on the CVs for density for different ROI sizes showed that CV tended to increase with an increase in eccentricity for the *in vivo* data, with significant trends for ROIs with a side dimension of 25 μm and 37 μm ($P < 0.05$). A two-way ANOVA performed on the CV data showed a significant effect of ROI size and eccentricity on cone density ($P < 0.001$ for each variable), with a significant interaction between ROI size and eccentricity ($P = 0.02$). The results of the subsequent post-hoc test (Table 4-3) showed that an ROI with a side dimension of 25 μm had significantly greater CVs relative to all other ROI sizes at eccentricities of 1.8 and 2.1 mm. ROIs with a side dimension of 25 μm also had significantly greater CVs relative to ROIs with side dimensions of 75 μm and 100 μm at an eccentricity of 1.2 mm, and with side dimensions of 50 μm, 75 μm, and 100 μm at an eccentricity of 1.5 mm. There were no significant differences in CV between ROI sizes for eccentricities closer than 1.2 mm. Mean CV values in cone density averaged across subjects and eccentricities for different ROI sizes are shown in Table 4-4.

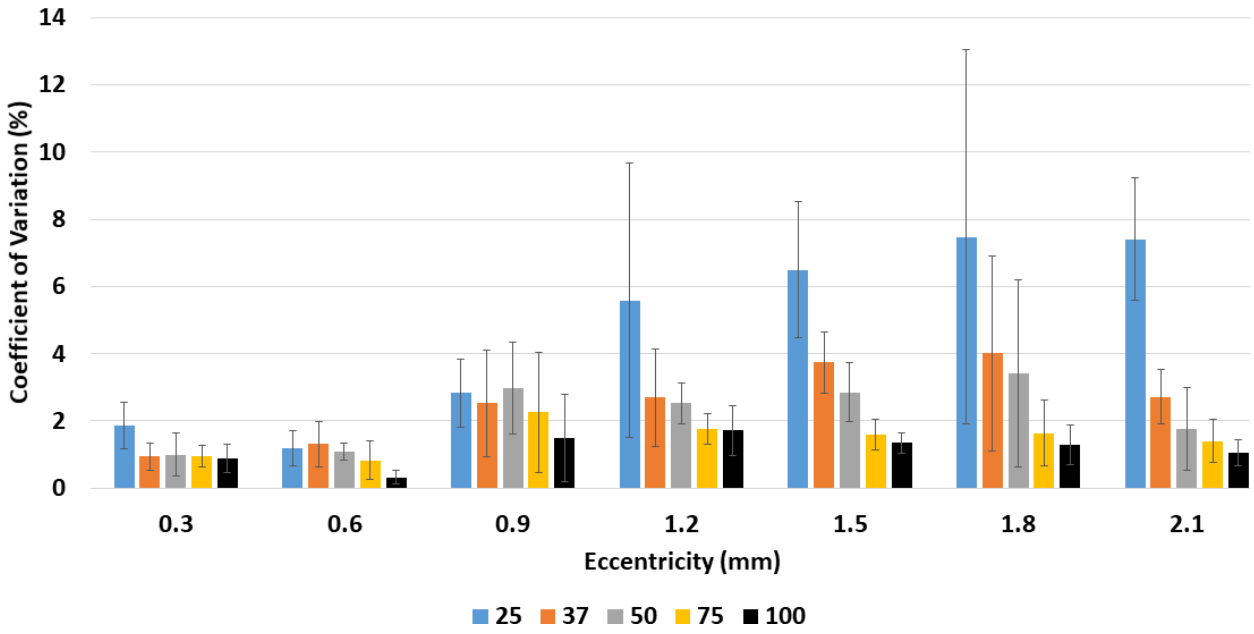

Figure 4-8. Mean CVs in bound cone density computed from *in vivo* cone mosaics across subjects using square ROIs with different side dimensions (blue – 25 µm; orange – 37 µm; gray – 50 µm; yellow – 75 µm; black – 100 µm) as a function of eccentricity. Error bars represent ± 1 standard deviation of the mean across subjects. There was a significant interaction between the ROI size and eccentricity ($P<0.05$). Values of CV calculated for smallest ROI size were significantly greater than larger ROI sizes for peripheral eccentricities ($P<0.05$).

Table 4-3. Post-hoc test result for the two-way ANOVA performed on the CVs of cone density comparing the main effects of eccentricity and ROI size.

Eccentricity	ROI side dimension (µm)	Significantly different than a side dimension of (µm)
1.2	25	75, 100
1.5	25	50, 75, 100
1.8	25	37, 50, 75, 100
2.1	25	37, 50, 75, 100

Table 4-4. Mean values for the Coefficients of Variation in bound cone density when averaged across all subjects and all eccentricities from in vivo images for different ROI sizes.

ROI Sizes	25 µm x 25 µm	37 µm x 37 µm	50 µm x 50 µm	75 µm x 75 µm	100 µm x 100 µm
Average	4.69	2.57	2.23	1.49	1.16
SD	2.47	1.05	0.89	0.45	0.42

Mean values of nearest neighbor distance (NND) are presented in Figure 4-9 for each ROI size across all examined eccentricities. The 2-way ANOVA analyses on the *in vivo* data

showed that there was a significant difference in NND values between different ROI sizes (P = 0.045) and there was no interaction between ROI size and Eccentricity (P=0.947). The post-hoc test revealed that NND values for ROIs with a side dimension of 25 μm were significantly larger than for ROIs with a side dimension of 100 μm across all eccentricities.

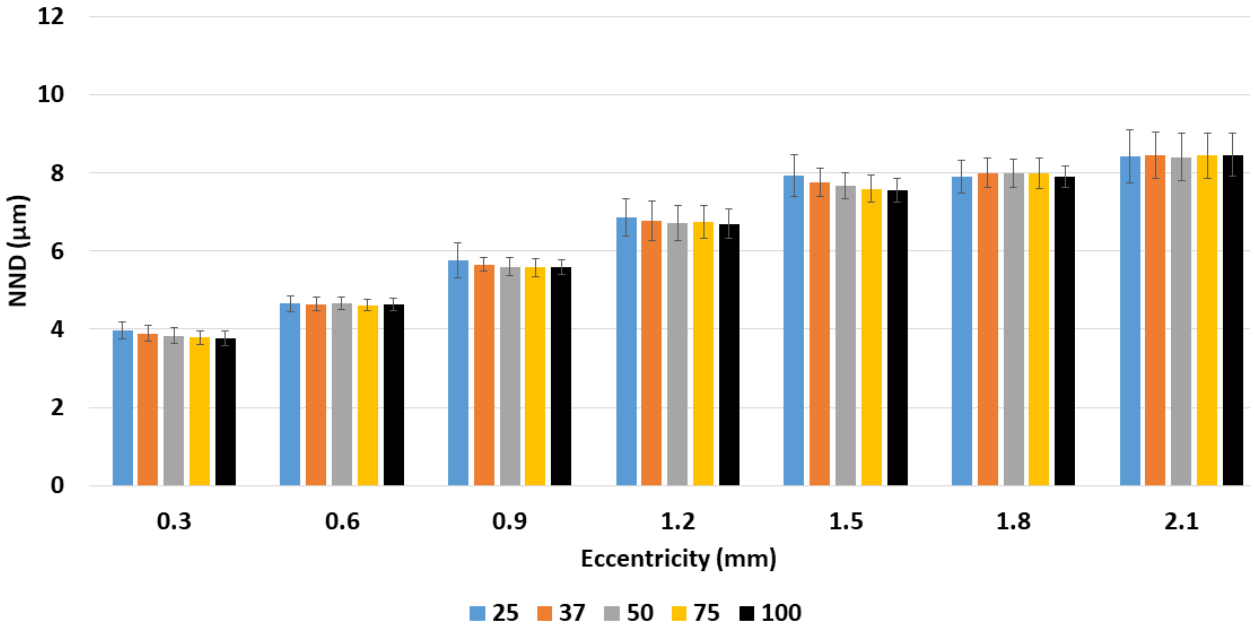

Figure 4-9. Mean values of nearest neighbor distance (NND) computed from *in vivo* cone mosaics using square ROIs with different side dimensions (blue – 25 μm; orange – 37 μm; gray – 50 μm; yellow – 75 μm; black – 100 μm) as a function of eccentricity. Error bars represent ± 1 standard deviation about the mean across subjects. Values of NND calculated for smallest ROI size were significantly different from largest ROI size across eccentricities (P<0.05).

Mean values of inter-cone distance (ICD) are presented in Figure 4-10 for each ROI size across all examined eccentricities. The 2-way ANOVA analyses on the *in vivo* data showed no significant difference in ICD values between different ROI sizes (P = 0.60) and no significant interaction between ROI size and eccentricity (P = 0.40).

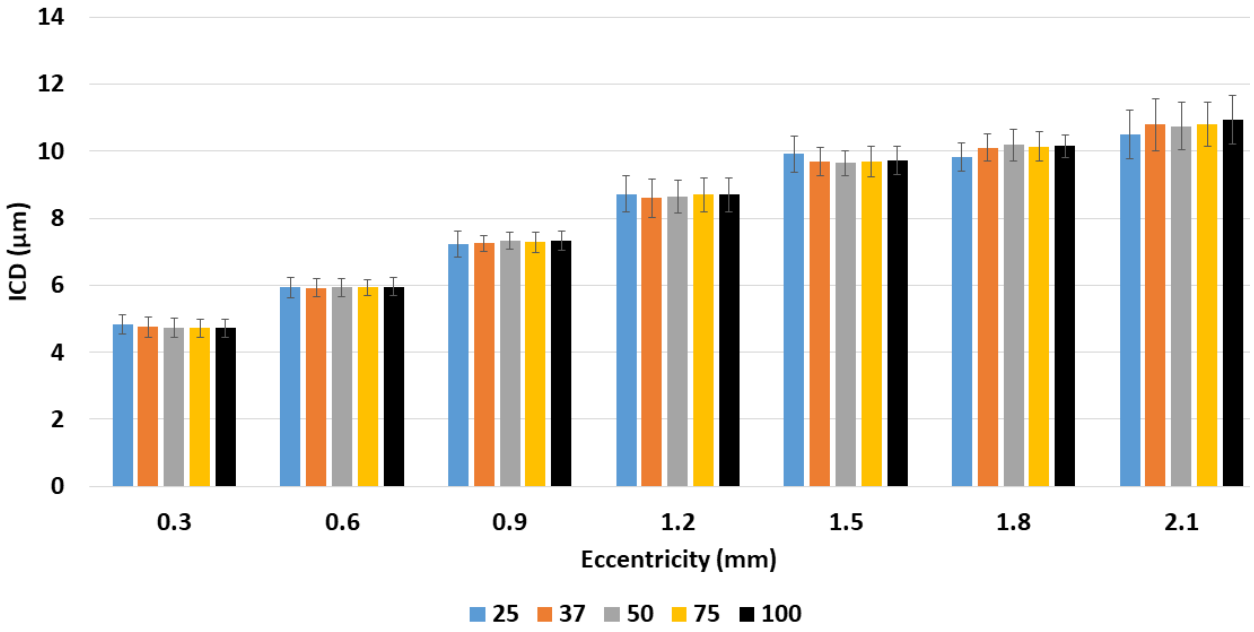

Figure 4-10. Mean values of inter-cone distance (ICD) computed from *in vivo* cone mosaics using square ROIs with different side dimensions (blue – 25 µm; orange – 37 µm; gray – 50 µm; yellow – 75 µm; black – 100 µm) as a function of eccentricity. Error bars represent ± 1 standard deviation about the mean across subjects. Values of ICD calculated for each ROI size were not significantly different from each other at any eccentricity (P>0.05).

Mean values of farthest neighbor distance (FND) are presented in Figure 4-11 for each ROI size across all examined eccentricities. The 2-way ANOVA analyses performed on the *in vivo* data showed that there was a significant difference in FND values between different ROI sizes ($P < 0.001$), but there was no interaction between ROI size and eccentricity ($P = 0.08$). A post-hoc test revealed that the FND values for ROIs with a side dimension of 25 µm were significantly smaller than FND values for ROIs with side dimensions of 50 µm, 75 µm, and 100 µm across all eccentricities. In addition, FND values for ROIs with a side dimension of 37 µm were significantly smaller than for ROIs with a side dimension of 100 µm.

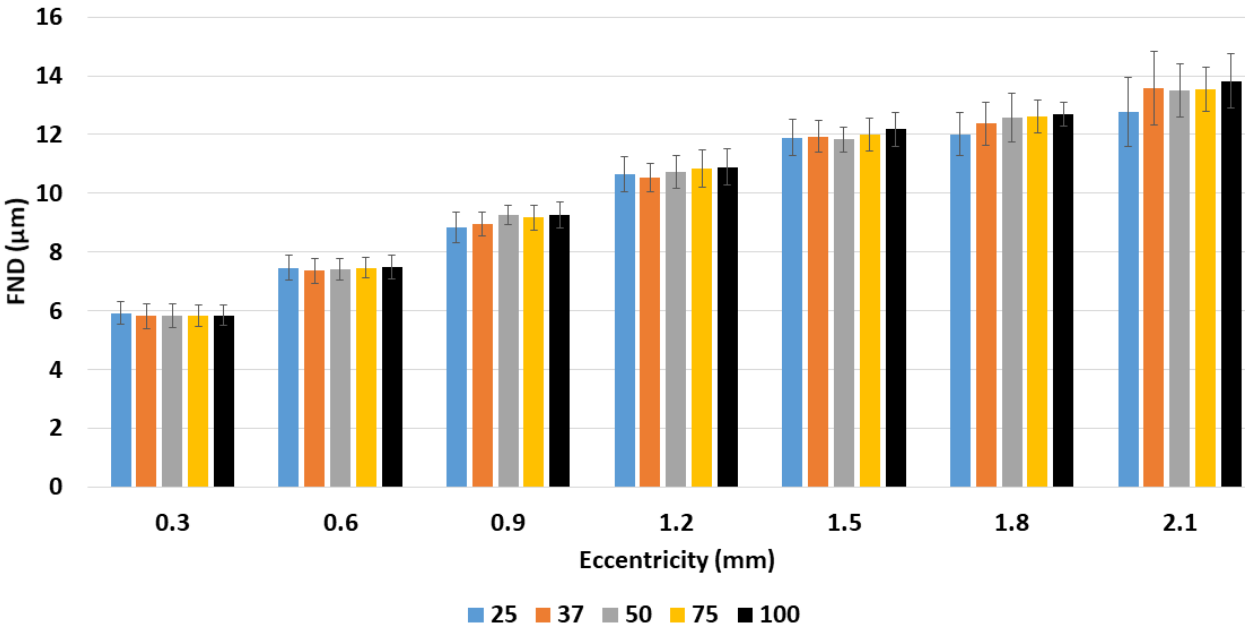

Figure 4-11. Mean values of farthest neighbor distance (FND) computed from *in vivo* cone mosaics using square ROIs with different side dimensions (blue – 25 µm; orange – 37 µm; gray – 50 µm; yellow – 75 µm; black – 100 µm) as a function of eccentricity. Error bars represent ± 1 standard deviation about the mean across subjects. Values of FND calculated for smaller ROI sizes were significantly different from larger ROI size across eccentricities ($P<0.05$).

Mean values of inter-cone regularity (ICR) are presented in Figure 4-12 for each ROI size across all examined eccentricities. For the regularity metric (and those that follow), we did not include data from the 25 x 25 µm ROI sizes because there were no standard deviations in cone metrics for some peripheral eccentricities (due to an undersampling of cones within the small ROI size). Given that the denominator of all examined regularity metrics is inversely proportional to the standard deviation (which sometimes did not exist), we omitted data from the 25 µm x 25 µm ROI size when analyzing the regularity metrics. The 2-way ANOVA analyses on the *in vivo* data showed that there was a significant difference in ICR values between different ROI sizes ($P < 0.001$) and there was no interaction between ROI size and eccentricity ($P = 0.12$). A post-hoc test revealed that the ICR values for ROIs with a side dimension of 37 µm were significantly greater than those ROIs with side dimension 50 µm, 75 µm, and 100 µm.

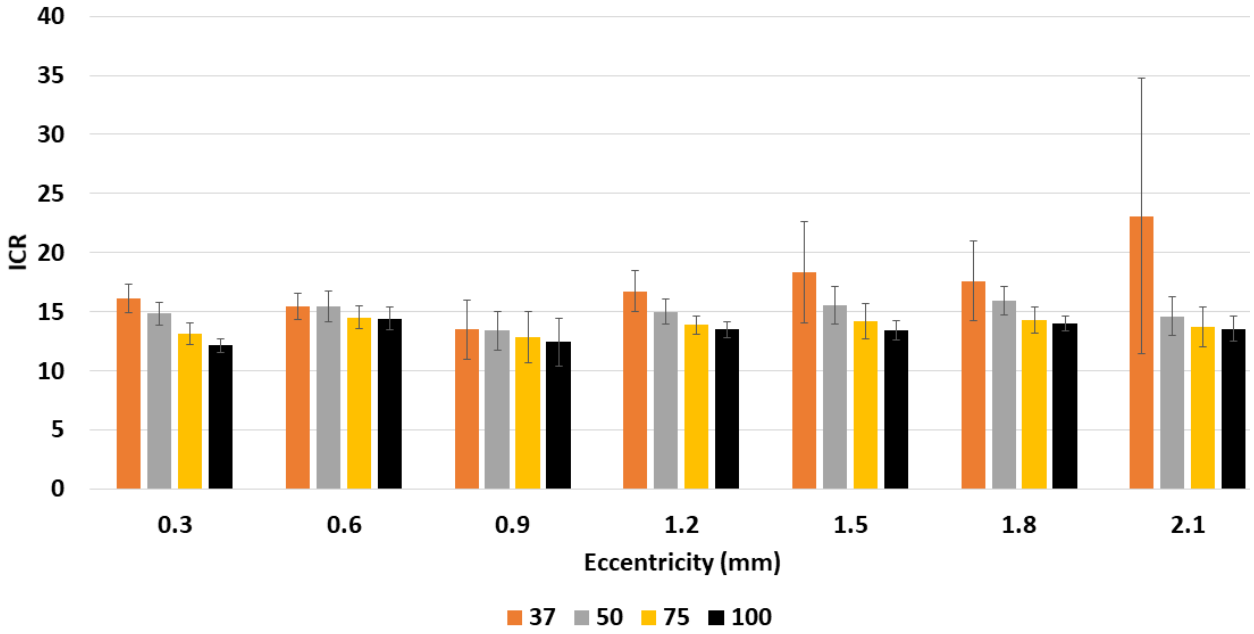

Figure 4-12. Mean values of inter-cone regularity (ICR) computed from *in vivo* cone mosaics using square ROIs with different side dimensions (orange – 37 µm; gray – 50 µm; yellow – 75 µm; black – 100 µm) as a function of eccentricity. Error bars represent ± 1 standard deviation about the mean across subjects. Values of ICR calculated for smallest ROI size were significantly different from larger ROI size across eccentricities ($P<0.05$).

Mean values of Voronoi area regularity (VAR) are presented in Figure 4-13 for each ROI size across all examined eccentricities. The 2-way ANOVA analyses on the *in vivo* data showed that there was a significant difference in VAR values between different ROI sizes ($P < 0.001$), but there was no significant interaction between ROI size and eccentricity ($P = 0.16$). A post-hoc test revealed that the VAR values for ROIs with a side dimension of 37 µm were significantly greater than those with side dimensions of 50 µm, 75 µm, and 100 µm across eccentricities, while ROIs with a side dimension of 50 µm were significantly different greater than ROIs with a side dimension of 100 µm.

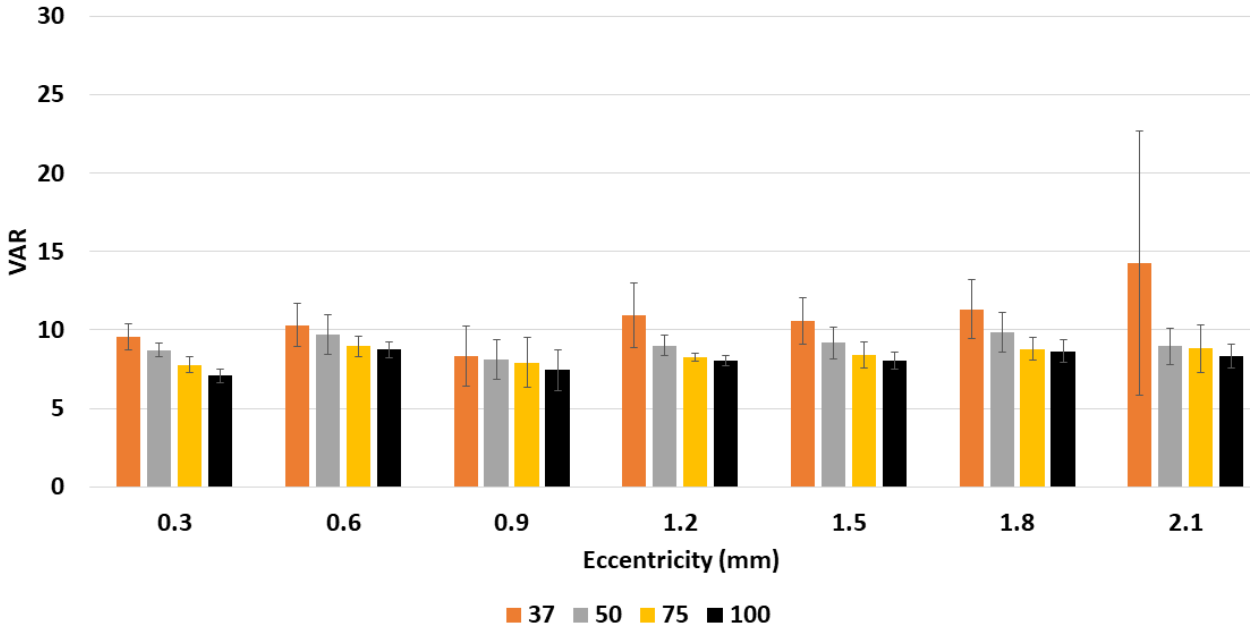

Figure 4-13. Mean values of Voronoi area regularity (VAR) computed from *in vivo* cone mosaics using square ROIs with different side dimensions (orange – 37 µm; gray – 50 µm; yellow – 75 µm; black – 100 µm) as a function of eccentricity. Error bars represent ± 1 standard deviation about the mean across subjects. Values of VAR calculated for smallest ROI size were significantly different from larger ROI size across eccentricities ($P<0.05$).

Mean values of number of neighbors regularity (NoNR) are presented in Figure 4-14 for each ROI size across all examined eccentricities. The 2-way ANOVA analyses on the *in vivo* data showed significant effects of ROI size and eccentricity on values of NoNR ($P < 0.001$ for both variables) with a significant interaction between ROI size and eccentricity ($P < 0.001$). A post-hoc test revealed that for eccentricities of 1.8 mm and 2.1 mm, ROIs with a side dimension of 37 µm were significantly greater across eccentricities than those ROIs with side dimensions of 50 µm, 75 µm, and 100 µm. There were no significant differences in NoNR values between the different ROI sizes for all other eccentricities.

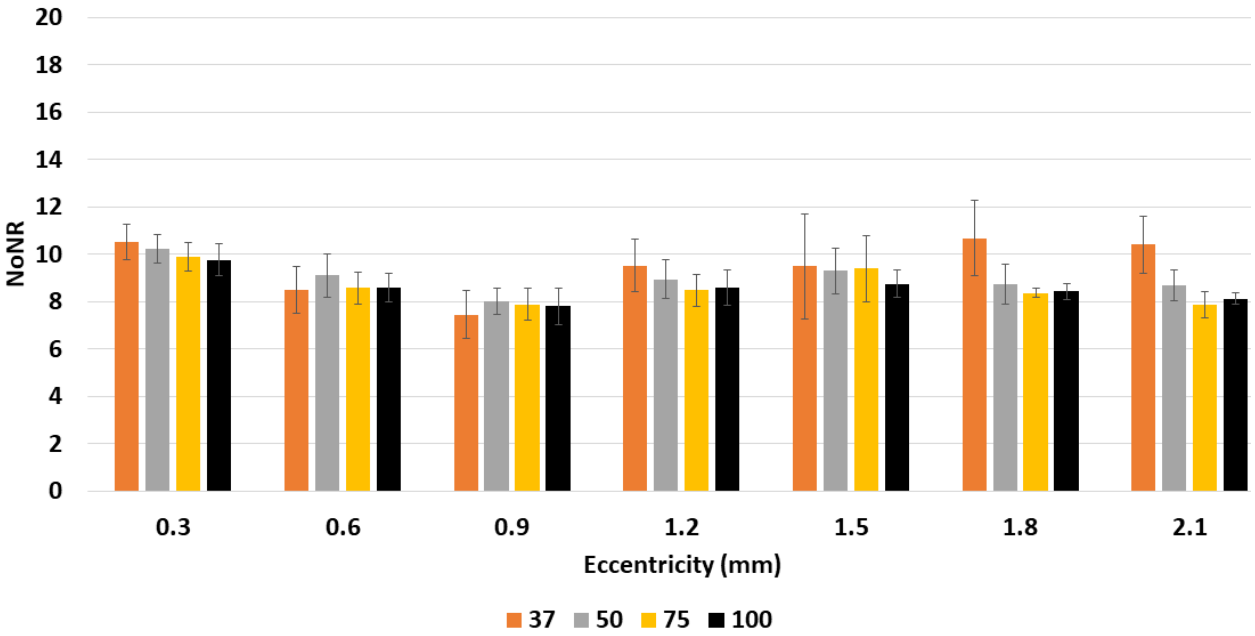

Figure 4-14. Mean values of number of neighbors regularity (NoNR) computed from *in vivo* cone mosaics using square ROIs with different side dimensions (orange – 37 µm; gray – 50 µm; yellow – 75 µm; black – 100 µm) as a function of eccentricity. Error bars represent ± 1 standard deviation about the mean across subjects. Values of NoNR calculated for smallest ROI size were significantly different from larger ROI sizes for peripheral eccentricities (P<0.05).

Mean values of the percent six-sided Voronoi (PSSV) are presented in Figure 4-15 for each ROI size across all examined eccentricities. The 2-way ANOVA analyses on the *in vivo* data showed that there were no significant differences in PSSV values between different ROI sizes (P = 0.48) and there was no significant interaction between ROI size and eccentricity (P = 0.06).

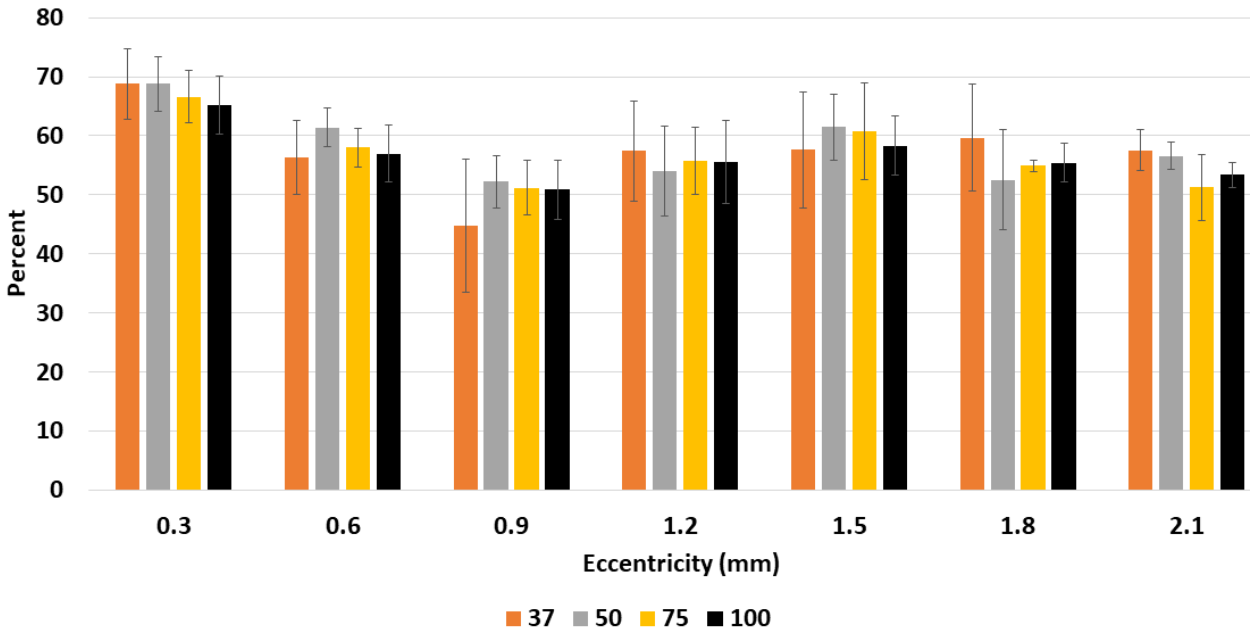

Figure 4-15. Mean values of percent six-sided Voronoi (PSSV) computed from *in vivo* cone mosaics using square ROIs with different side dimensions (orange – 37 µm; gray – 50 µm; yellow – 75 µm; black – 100 µm) as a function of eccentricity. Error bars represent ± 1 standard deviation about the mean across subjects. Values of PSSV calculated for each ROI size were not significantly different from each other at any eccentricity (P>0.05).

To better understand the relative contributions of different factors in the total variability of different metrics calculated from the *in vivo* data, a linear mixed model was fit to different sources of variance, including eccentricity, inter-subject variability, ROI size, and other errors (which could include components such as measurement error, biological noise, etc). The percentage that each of these potential sources of variation contributed to the total variance is presented in Table 4-5 for each cone metric. For the density and spacing metrics, the primary contributor to the total variability of these metrics is the eccentricity being analyzed. Other errors contributed the least to density, while ROI size contributed the least to spacing metrics. For the regularity metrics, the primary contributor was other errors. Subjects contributed the least for ICR and VAR, while ROI size contributed the least to NoNR and PSSV.

Table 4-5. Percentage of the total variance in different cone metrics accounted for by the effects of eccentricity, subject, ROI size, and other errors.

	Density	NND	ICD	FND	ICR	VAR	NoNR	PSSV
Eccentricity	62.82	95.05	95.5	94.42	4.51	5.2	25.07	37.47
Subject	18.36	1.70	1.99	2.27	1.49	1.97	9.71	9.50
ROI Size	17.56	0.02	0.06	0.15	20.93	20.45	9.02	0.82
Other Error	1.26	3.23	2.45	3.16	73.07	72.39	56.20	52.21

4.4 Discussion

The main purpose of this study was to explore one of the least discussed technical aspects of the quantification of AOSLO images of cone photoreceptors i.e. the effect of using different ROI sizes in the cone mosaic geometry metrics. Our data showed that the smallest ROI size yielded values significantly different than other ROI sizes at closer eccentricities and were closest to the simulated values. Across eccentricities, coefficient of variations in calculating cone density were most variable for smaller ROIs compared to the larger ROIs and increased with increasing eccentricity.

To make it possible to compare the data with a known mosaic, we developed a custom MATLAB program that gave us the desired cone coordinates from ROIs of different sizes at different random orientations from different eccentricities. To make this simulated cone mosaic behave similar to the *in vivo* cone mosaic, we incorporated the change in density as a function of eccentricity, using a log model fit to data from Curcio et al. (1990). Because of the limitation of the algorithm as explained in the methods, the simulated cones are arranged in a triangular pattern but those triangles are not constrained to be equilateral or isosceles. The area of these triangles is equal to the area of an equilateral triangle having each side equal to the spacing of cones at that particular eccentricity. This strategy provides the desired bound density, but the controlled locations of the cones produce a varying triangular arrangement. So, for the simulated data, it was appropriate to only analyze the density metric.

The result showed that for the closer eccentricities (0.075mm, 0.1mm and 0.2mm) the common finding was that the density value using smallest ROI size (25 × 25 μm) was significantly different than using the bigger ROI sizes and the one sample t-test also showed that for those eccentricities, the mean percent error using 25 × 25 μm ROI size was not significantly different than zero. These results mean that using smaller ROI sizes for eccentricities very close to the center of the retina where the cone density change is very rapid can give us accurate density rather than using bigger ROI sizes. The *in vivo* data was in agreement with the simulated data in that there was no significant difference in density values with different ROI sizes for the same eccentricity range.

Along the selected temporal meridian, when the ROI size increases, one side moves centrally and the other side moves temporally. The upper and lower sides do not move much relative to the center (fovea) of the retina. The side that is moving closer to the fovea is in a region where the density of cones is changing rapidly compared to the region where the opposite side is moving. This imbalance results in a slight increase in the density of the cones as the ROI size increases. This effect is more if the ROI is closer to the center and less if the ROI is further away. In our *in vivo* data, we could see this tendency at 0.3 mm but not at other eccentricities. This is because the contribution of ROI size to the total variability of data is less than the contribution of other factors like inter-subject variability and eccentricity as shown in Table 4-5.

The analysis of the variation of the density measurements showed that smaller ROI sizes gave significantly more variable density values compared to the large ROI sizes, which are in accordance with the study done by Lombardo et al. (2014). This can be because small ROIs will have a small number of samples (cones) so any deviations from the average will make a larger impact on the average itself whereas large ROIs will have a large number of samples where any deviation from average will be distributed over the large sample and won’t make a

bigger impact. This also explains the increase in variability with the increase in eccentricity for both the simulated and *in vivo* data.

Similar to the density data, the ICD was also not significantly different for different ROI sizes at all eccentricities examined. Increasing ROI size keeping the subject and eccentricity constant will include a region with smaller spacing between cones in a larger number on one side and with larger spacing between cones in a smaller number on the opposite side. This will decrease the average spacing between the cones but this effect will be smaller as we move away from the center of the retina. We can see this effect for the 0.3mm eccentricity in our data but not at eccentricities further away. NND and FND are the metrics that are looking for the nearest and furthest cones to all the bound cones in the ROI, so the effect of ROI size change can be significant between smaller and larger ROI sizes as seen in our data though the spacing metrics variability is mainly driven by the eccentricity change.

Our data show that regularity metrics are affected most by other errors, which could include factors such as global changes in the mosaic (e.g., an overall compression of the Voronoi tiles in one meridian, biological noise, measurement errors). One difference among the regularity metrics in our data was that a change in ROI size contributed to the total variability more for ICR and VAR than to NoNR and PSSV. This makes sense because when one increases or decreases the ROI size at the same eccentricity for the same subject, then ICR and VAR change as the standard deviation of the ICD, while Voronoi area changes because of the introduction or deletion of areas with different ICD and Voronoi area. The standard deviation of the ICD and Voronoi area doesn't change much when ROI size remains the same and one changes the eccentricity which results in small ICR and VAR variability. Whereas change in eccentricity keeping the ROI size and subject same affects NoNR and PSSV more than it affects ICR and VAR as a change in eccentricity is either moving the ROI towards the center of the retina where the cones are more regularly arranged and most of the cones are surrounded

by 6 other cones or away from where the cones are less regularly arranged and more cones are surrounded by less than 6 other cones.

In conclusion, a change in ROI size affects the different cone mosaic geometry metrics differently. Smaller ROI sizes give accurate density values for eccentricities very close to the center of the retina whereas larger ROI sizes will have less variability in the data. The variability also increases with an increase in eccentricity. For spacing metrics, a large percent of the total variability is driven by the eccentricity compared to the other factors. The regularity of the cone mosaic decreases when the ROI size is increased, mainly for the peripheral eccentricities. The regularity metrics are more sensitive to the measurement errors compared to the eccentricity and ROI size changes.

4.5 Acknowledgements

This work was supported by Student Vision Research Support Grant (sVRSG) from the University of Houston College of Optometry and NIH Grant P30 EY007551. We would like to acknowledge Dr. Joseph Carroll for his valuable suggestions in the data analysis.

CHAPTER 5

General Conclusions

5.1 General Conclusions

Different cone photoreceptor metrics have been calculated from confocal and split-detector adaptive optics scanning laser ophthalmoscope (AOSLO) images to study the normal and diseased retina (Chui et al., 2008; Gill et al., 2019; Randerson et al., 2015; Scoles et al., 2014; Song et al., 2011; Sun et al., 2016; Talcott et al., 2011). Despite their increasing use, there remains a general lack of normative data in the literature comparing cone properties between these two imaging modalities and the repeatability with which cone metrics can be quantified using these techniques. Moreover, there is limited published data that explains the effects of certain factors that can potentially impact the quantification of cone metrics from *in vivo* AOSLO images. The projects performed for this work were designed to develop a set of normative data that could be used to explore the degree of similarity in measurements of cone packing made between confocal and split detector imaging modalities and their repeatability over time (Chapter 2), and to offer insights on methods that could be used when quantifying cone metrics to provide the highest accuracy and the least variability (Chapters 3 and 4).

5.1.1 Specific Aim 1 (Chapter 2) - Determine the repeatability of quantifying cone photoreceptor packing metrics in confocal and split-detector AOSLO images from healthy eyes

Split-detector imaging is a relatively new modality that has been demonstrated in AOSLO systems and provides an alternative view of the cone mosaic relative to confocal AOSLO imaging. Prior to assessing whether changes in the photoreceptor mosaic have occurred over time (such as for diseased eyes or clinical trial-related applications), it is important to understand factors that can impact measurements of cone metrics in healthy eyes, such as the intrasession and intersession variabilities of the imaging and quantification techniques. While recent work has examined the intrasession variability in quantifying cone density and spacing (Garrioch et al., 2012) and the longitudinal variability in quantifying cone density (Jackson et al.,

2019) from *confocal* AOSLO images, there is a lack of data detailing the longitudinal variability in cone packing metrics (other than density) as measured from confocal and split detector images of the cone mosaic (particularly for peripheral retinal eccentricities), as well as the level of agreement between measurements obtained from the two modalities at the same retinal locations. To address these questions, we first calculated and compared different cone packing metrics derived from confocal and split-detector images from the same patches of retina imaged at different eccentricities in 10 healthy human eyes at a baseline time point. The same retinal areas from the same subjects were imaged again after 12 months and the intersession repeatability was calculated. The results of this work showed that there is very good correspondence between the confocal and split detector modalities of AOSLO imaging. Even though there are qualitative differences in the appearance of the cones between the two modalities, cone packing geometry metrics are not significantly different. This study also reported the repeatability values of quantifying confocal and split-detector images of cones in healthy eyes at different eccentricities. These data can be used as a reference for future studies that aim to examine similar metrics in diseased eyes over time.

5.1.2 Specific Aim 2 (Chapter 3) - Determine the impact of different cone marking techniques on the quantification of cone packing measurements in images of simulated and in vivo cone mosaics of healthy eyes

While working on Aim 1, we thought critically about methodological parameters we wished to use at different stages of our image processing and quantification process. After performing literature searches to investigate methods employed by other laboratories, we discovered that there was limited published data detailing the impact of different methodological choices on metrics of cone packing, such as methods by which cones are marked in an image. Consequently, different methods have been used to identify and mark cones in AO images from living eyes with little knowledge of whether different marking techniques can result in different

values of cone metrics. We calculated bound and unbound cone densities after marking cones using 3 different methods in simulated and *in vivo* cone mosaics. The mean percent error of calculating unbound cone density after marking all cones fully within and partially along the border of the region of interest (ROI) was significantly higher than the rest of the marking techniques. Regardless of the marking technique, the variation in density measurements was higher when calculating unbound density. Based on the results of this study, we recommend calculating bound density (to minimize variability) and marking all cones fully or partially within an ROI to increase the number of samples for the measurement, particularly for peripheral locations where the cone spacing is higher.

5.1.3 Specific Aim 3 (Chapter 4) - Determine the impact of different ROI sizes on the quantification of cone packing measurements in images of simulated and in vivo cone mosaics from healthy eyes at different eccentricities

While studies have used different techniques for marking cones, multiple studies have also used different approaches for selecting a region of interest (ROI) size for analyzing cone packing in living eyes. Studies that have examined the impact of changing the size of the ROI used to calculate cone metrics have been limited in the packing metrics that were calculated, the retinal eccentricities examined (Lombardo et al., 2014) or the range of ROI sizes included. Therefore, there is limited knowledge about whether an optimal ROI size exists for use at different eccentricities. We generated simulated images of cone mosaics with gradient densities based on histological reports and collected AOSLO images in healthy eyes. These simulated and *in vivo* mosaics were used to study whether cone metrics differed with a change in ROI size. Data presented in this study suggest that different metrics are affected differently by a change in ROI size. Small ROI sizes were more accurate for eccentricities close to the foveal center while large ROI sizes were less variable, particularly for more peripheral eccentricities. While our data show that bound cone density calculations for eccentricities greater than 0.2 mm are independent of

ROI size, we suggest using larger ROI sizes for these eccentricities due to their increased sampling (and, hence, lower variability) in healthy eyes.

Future directions

One of the reasons I initially joined the Porter laboratory was to have the opportunity to engage in a study that would examine changes in cone structure in eyes with retinal degenerations. While I was not able to accomplish this goal for my dissertation, I am pleased that the work detailed here will place the Porter lab in a better position to do so in the future. To this point, it would be interesting to study longitudinally changes in photoreceptor metrics in diseased eyes using confocal and split-detector modalities and compare these changes with the normative variability established in Chapter 2. With future developments in cone identification algorithms, it will also be interesting to investigate the repeatability of imaging rods using those algorithms, particularly for those inherited retinal degenerations in which rods are known to play a crucial role (such as retinitis pigmentosa).

The closest eccentricity we examined in this dissertation for *in vivo* data was 0.3 mm from the foveal center. It would be interesting to expand the work done for all chapters, but particularly for Chapters 3 and 4, to even closer eccentricities that also include peak cone densities. Further refinements could also be considered when generating our simulated data to better model the gradient densities and spacings measured in healthy eyes. For example, many AOSLO imaging studies now report cone density measurements for different eccentricities for different aged individuals. The algorithm used to generate the simulated cone data could be migrated from being based on histological data (performed in only a handful of eyes with a large range in age) to in vivo data that is more specific for the age of the subjects being analysed. It would also be desirable to have the ability to quantify metrics other than density using this custom program.

For the ROI size project detailed in Chapter 4, we examined the impact of changing the ROI size on cone metrics at different eccentricities. However, all ROIs possessed a square shape. It would be interesting to explore whether the shape of the ROI influences cone metrics. For example, examining ROIs that possess other shapes (such as rectangles and circles), but have the same area, could provide more insight into the effects of ROI shapes on cone metrics.

REFERENCES

Abozaid, M. A., Langlo, C. S., Dubis, A. M., Michaelides, M., Tarima, S., & Carroll, J. (2016). Reliability and Repeatability of Cone Density Measurements in Patients with Congenital Achromatopsia. *Advances in Experimental Medicine and Biology*, *854*, 277–283.

ANSI. (2014). *American National Standard for Safe Use of Lasers ANSI Z136.1-2014*.

Baden, T., & Osorio, D. (2019). The Retinal Basis of Vertebrate Color Vision. *Annual Review of Vision Science*, *5*, 177–200.

Baraas, R. C., Carroll, J., Gunther, K. L., Chung, M., Williams, D. R., Foster, D. H., & Neitz, M. (2007). Adaptive optics retinal imaging reveals S-cone dystrophy in tritan color-vision deficiency. *Journal of the Optical Society of America. A, Optics, Image Science, and Vision*, *24*(5), 1438–1447.

Baylor, D. A., Lamb, T. D., & Yau, K. W. (1979). Responses of retinal rods to single photons. *The Journal of Physiology*, *288*, 613–634.

Beckers, J. M. (1993). Adaptive Optics for Astronomy: Principles, Performance, and Applications. *Annual Review of Astronomy and Astrophysics*, *31*(1), 13–62.

Birch, D. G., Bennett, L. D., Duncan, J. L., Weleber, R. G., & Pennesi, M. E. (2016). Long-term Follow-up of Patients With Retinitis Pigmentosa Receiving Intraocular Ciliary Neurotrophic Factor Implants. *American Journal of Ophthalmology*, *170*, 10–14.

Bland, J. M., & Altman, D. G. (1999). Measuring agreement in method comparison studies. *Statistical Methods in Medical Research*, *8*(2), 135–160.

Chui, Toco Y P, Vannasdale, D. A., & Burns, S. A. (2012). The use of forward scatter to improve retinal vascular imaging with an adaptive optics scanning laser ophthalmoscope. *Biomedical Optics Express*, *3*(10), 2537–2549.

Chui, Toco Yuen Ping, Song, H. X., & Burns, S. A. (2008). Individual variations in human cone photoreceptor packing density: Variations with refractive error. *Investigative Ophthalmology and Visual Science*, *49*(10), 4679–4687.

Cooper, R. F., Langlo, C. S., Dubra, A., & Carroll, J. (2013). Automatic detection of modal spacing (Yellott's ring) in adaptive optics scanning light ophthalmoscope images. *Ophthalmic & Physiological Optics : The Journal of the British College of Ophthalmic Opticians (Optometrists)*, *33*(4), 540–549.

Cooper, R. F., Wilk, M. A., Tarima, S., & Carroll, J. (2016). Evaluating descriptive metrics of the human cone mosaic. *Investigative Ophthalmology and Visual Science*, *57*(7), 2992–3001.

Curcio, C A, Millican, C. L., Allen, K. A., & Kalina, R. E. (1993). Aging of the human photoreceptor mosaic: evidence for selective vulnerability of rods in central retina. *Investigative Ophthalmology & Visual Science*, *34*(12), 3278–3296.

Curcio, Christine A, Sloan, K. R., Kalina, R. E., & Hendrickson, A. E. (1990). Human

Photoreceptor Topography. *The journal of comparative neurology*, *523*, 497–523.

De Rojas, J. O., Schuerch, K., Mathews, P. M., Cabral, T., Hazan, A., Sparrow, J., Tsang, S. H., & Suh, L. H. (2017). Evaluating Structural Progression of Retinitis Pigmentosa After Cataract Surgery. *American Journal of Ophthalmology*, *180*, 117–123.

Dees, E. W., Dubra, A., & Baraas, R. C. (2011). Variability in parafoveal cone mosaic in normal trichromatic individuals. *Biomedical Optics Express*, *2*(5), 1351–1358.

Delori, F. C., Webb, R. H., & Sliney, D. H. (2007). Maximum permissible exposures for ocular safety (ANSI 2000), with emphasis on ophthalmic devices. *Journal of the Optical Society of America A*, *24*(5), 1250.

Domenic V, C. (1994). Guidlines, Criteria, and Rules of Thumb for Evalauting Normed and Standardized Assessment Instruments in Psychology. *Psychological Assessment*, *6*(4), 284–290.

Dubra, A., & Harvey, Z. (2010). Registration of 2D Images from Fast Scanning Ophthalmic Instruments. In B. Fischer, B. M. Dawant, & C. Lorenz (Eds.), *Biomedical Image Registration* (pp. 60–71). Springer Berlin Heidelberg.

Dubra, A., Sulai, Y., Norris, J. L., Cooper, R. F., Dubis, A. M., Williams, D. R., & Carroll, J. (2011). Noninvasive imaging of the human rod photoreceptor mosaic using a confocal adaptive optics scanning ophthalmoscope. *Biomedical Optics Express*, *2*(7), 1864–1876.

Feng, S., Gale, M. J., Fay, J. D., Faridi, A., Titus, H. E., Garg, A. K., Michaels, K. V, Erker, L. R., Peters, D., Smith, T. B., & Pennesi, M. E. (2015). Assessment of Different Sampling Methods for Measuring and Representing Macular Cone Density Using Flood-Illuminated Adaptive Optics. *Investigative Ophthalmology & Visual Science*, *56*(10), 5751–5763.

Garrioch, R., Langlo, C., Dubis, A. M., Cooper, R. F., Dubra, A., & Carroll, J. (2012). Repeatability of in vivo parafoveal cone density and spacing measurements. *Optometry and Vision Science*, *89*(5), 632–643.

Genead, M. A., Fishman, G. A., Rha, J., Dubis, A. M., Bonci, D. M. O., Dubra, A., Stone, E. M., Neitz, M., & Carroll, J. (2011). Photoreceptor structure and function in patients with congenital achromatopsia. *Investigative Ophthalmology & Visual Science*, *52*(10), 7298–7308.

Gill, J. S., Georgiou, M., Kalitzeos, A., Moore, A. T., & Michaelides, M. (2019). Progressive cone and cone-rod dystrophies: clinical features, molecular genetics and prospects for therapy. *British Journal of Ophthalmology*, *103*(5), 711–720.

Hofer, H., Carroll, J., Neitz, J., Neitz, M., & Williams, D. R. (2005). Organization of the human trichromatic cone mosaic. *Journal of Neuroscience*, *25*(42), 9669–9679.

Jackson, K., Vergilio, G. K., Cooper, R. F., Ying, G. S., & Morgan, J. I. W. (2019). A 2-year longitudinal study of normal cone photoreceptor density. *Investigative Ophthalmology and Visual Science*, *60*(5), 1420–1430.

Jacob, J., Paques, M., Krivosic, V., Dupas, B., Erginay, A., Tadayoni, R., & Gaudric, A. (2017).

Comparing Parafoveal Cone Photoreceptor Mosaic Metrics in Younger and Older Age Groups Using an Adaptive Optics Retinal Camera. *Ophthalmic Surgery, Lasers & Imaging Retina*, *48*(1), 45–50.

Jonnal, R. S., Besecker, J. R., Derby, J. C., Kocaoglu, O. P., Cense, B., Gao, W., Wang, Q., & Miller, D. T. (2010). Imaging outer segment renewal in living human cone photoreceptors. *Optics Express*, *18*(5), 5257–5270.

Koo, T. K., & Li, M. Y. (2016). A Guideline of Selecting and Reporting Intraclass Correlation Coefficients for Reliability Research. *Journal of Chiropractic Medicine*, *15*(2), 155–163.

Legras, R., Gaudric, A., & Woog, K. (2018). Distribution of cone density, spacing and arrangement in adult healthy retinas with adaptive optics flood illumination. *PLOS ONE*, *13*(1).

Li, K. Y., & Roorda, A. (2007). Automated identification of cone photoreceptors in adaptive optics retinal images. *Journal of the Optical Society of America A*, *24*(5), 1358.

Li, K. Y., Tiruveedhula, P., & Roorda, A. (2010). Intersubject variability of foveal cone photoreceptor density in relation to eye length. *Investigative Ophthalmology and Visual Science*, *51*(12), 6858–6867.

Liang, J., Grimm, B., Goelz, S., & Bille, J. F. (1994). Objective measurement of wave aberrations of the human eye with the use of a Hartmann-Shack wave-front sensor. *Journal of the Optical Society of America. A, Optics, Image Science, and Vision*, *11*(7), 1949–1957.

Liang, J., Williams, D. R., & Miller, D. T. (1997). Supernormal vision and high-resolution retinal imaging through adaptive optics. *Journal of the Optical Society of America. A, Optics, Image Science, and Vision*, *14*(11), 2884–2892.

Liu, B. S., Tarima, S., Visotcky, A., Pechauer, A., Cooper, R. F., Landsem, L., Wilk, M. A., Godara, P., Makhijani, V., Sulai, Y. N., Syed, N., Yasumura, G., Garg, A. K., Pennesi, M. E., Lujan, B. J., Dubra, A., Duncan, J. L., & Carroll, J. (2014). The reliability of parafoveal cone density measurements. *British Journal of Ophthalmology*, *98*(8), 1126.

Lombardo, M., Lombardo, G., Lomoriello, D. S., Ducoli, P., Stirpe, M., & Serrao, S. (2013). Interocular symmetry of parafoveal photoreceptor cone density distribution. *Retina*, *33*(8), 1640–1649.

Lombardo, M., Serrao, S., Ducoli, P., & Lombardo, G. (2013). Influence of sampling window size and orientation on parafoveal cone packing density. *Biomedical Optics Express*, *4*(8), 1318–1331.

Lombardo, M., Serrao, S., & Lombardo, G. (2014). Technical Factors Influencing Cone Packing Density Estimates in Adaptive Optics Flood Illuminated Retinal Images. *PLOS ONE*, *9*(9), 1–11.

Mallen, E. A. H., & Kashyap, P. (2007). Technical Note: Measurement of retinal contour and supine axial length using the Zeiss IOLMaster. *Ophthalmic and Physiological Optics*, *27*(4), 404–411.

Merino, D., Duncan, J. L., Tiruveedhula, P., & Roorda, A. (2011). Observation of cone and rod photoreceptors in normal subjects and patients using a new generation adaptive optics scanning laser ophthalmoscope. *Biomedical Optics Express*, *2*(8), 2189–2201.

Miao, I., Bhakta, A. S., Sredar, N., Ivers, K. M., Patel, N. B., Queener, H. M., Locke, K. G., Birch, D. G., & Porter, J. (2014). In vivo examination of cone photoreceptors in patients with Retinitis Pigmentosa implanted over five years ago with encapsulated Ciliary Neurotrophic Factor. *Investigative Ophthalmology & Visual Science*, *55*(13), 2619.

Miller, D. T., Williams, D. R., Morris, G. M., & Liang, J. (1996). Images of cone photoreceptors in the living human eye. *Vision Research*, *36*(8), 1067–1079.

Morgan, J. I. W., Han, G., Klinman, E., Maguire, W. M., Chung, D. C., Maguire, A. M., & Bennett, J. (2014). High-resolution adaptive optics retinal imaging of cellular structure in choroideremia. *Investigative Ophthalmology and Visual Science*, *55*(10), 6381–6397.

Osterberg G. (1935). No Title. *Acta Ophthal Suppl.*, *65*, 1–103.

Pallikaris, A., Williams, D. R., & Hofer, H. (2003). The reflectance of single cones in the living human eye. *Investigative Ophthalmology and Visual Science*, *44*(10), 4580–4592.

Park, S. P., Chung, J. K., Greenstein, V., Tsang, S. H., & Chang, S. (2013). A study of factors affecting the human cone photoreceptor density measured by adaptive optics scanning laser ophthalmoscope. *Experimental Eye Research*, *108*, 1–9.

Patterson, E. J., Kalitzeos, A., Kasilian, M., Gardner, J. C., Neitz, J., Hardcastle, A. J., Neitz, M., Carroll, J., & Michaelides, M. (2018). Residual Cone Structure in Patients With X-Linked Cone Opsin Mutations. *Investigative Ophthalmology & Visual Science*, *59*(10), 4238–4248.

Pircher, M., Kroisamer, J. S., Felberer, F., Sattmann, H., Götzinger, E., & Hitzenberger, C. K. (2011). Temporal changes of human cone photoreceptors observed in vivo with SLO/OCT. *Biomed. Opt. Express*, *2*(1), 100–112.

Putnam, N. M., Hofer, H. J., Doble, N., Chen, L., Carroll, J., & Williams, D. R. (2005). The locus of fixation and the foveal cone mosaic. *Journal of Vision*, *5*(7), 632–939.

Randerson, E. L., Davis, D., Higgins, B., Kim, J. E., Han, D. P., Connor, T. B., Wirostko, W. J., & Carroll, J. (2015). Assessing Photoreceptor Structure in Macular Hole using Split-detector Adaptive Optics Scanning Light Ophthalmoscopy. *European Ophthalmic Review*, *09*(01), 59.

Roorda, A., & Williams, D. R. (1999). The arrangement of the three cone classes in the living human eye. *Nature*, *397*(6719), 520–522.

Rossi, E. A., Granger, C. E., Sharma, R., Yang, Q., Saito, K., Schwarz, C., Walters, S., Nozato, K., Zhang, J., Kawakami, T., Fischer, W., Latchney, L. R., Hunter, J. J., Chung, M. M., & Williams, D. R. (2017). Imaging individual neurons in the retinal ganglion cell layer of the living eye. *Proceedings of the National Academy of Sciences*, *114*(3), 586–591.

Rossi, E. A., & Roorda, A. (2010). The relationship between visual resolution and cone spacing in the human fovea. *Nature Neuroscience*, *13*(2), 156–157.

Scarinci, F., Jampol, L. M., Linsenmeier, R. A., & Fawzi, A. A. (2015). Association of Diabetic Macular Nonperfusion With Outer Retinal Disruption on Optical Coherence Tomography. *JAMA Ophthalmology*, *133*(9), 1036–1044.

Scoles, D., Sulai, Y. N., Cooper, R. F., Higgins, B. P., Johnson, R. D., Carroll, J., Dubra, A., & Stepien, K. E. (2017). Photoreceptor inner segment morphology in best vitelliform macular dystrophy. *Retina (Philadelphia, Pa.)*, *37*(4), 741–748.

Scoles, D., Sulai, Y. N., Langlo, C. S., Fishman, G. A., Curcio, C. A., Carroll, J., & Dubra, A. (2014). In Vivo Imaging of Human Cone Photoreceptor Inner Segments. *Investigative Ophthalmology and Visual Science*, *55*(7), 4244–4251.

Song, H., Chui, T. Y. P., Zhong, Z., Elsner, A. E., & Burns, S. A. (2011). Variation of cone photoreceptor packing density with retinal eccentricity and age. *Investigative Ophthalmology and Visual Science*, *52*(10), 7376–7384.

Song, H., Rossi, E. A., Latchney, L., Bessette, A., Stone, E., Hunter, J. J., Williams, D. R., & Chung, M. (2015). Cone and rod loss in Stargardt disease revealed by adaptive optics scanning light ophthalmoscopy. *JAMA Ophthalmology*, *133*(10), 1198–1203.

Stevenson, S. B., & Roorda, A. (2005). Correcting for miniature eye movements in high resolution scanning laser ophthalmoscopy. In F. Manns, P. G. Soederberg, A. Ho, B. E. Stuck, & M. Belkin (Eds.), *procspie* (Vol. 5688, pp. 145–151).

Sun, L. W., Johnson, R. D., Langlo, C. S., Cooper, R. F., Razeen, M. M., Russillo, M. C., Dubra, A., Connor, T. B. J., Han, D. P., Pennesi, M. E., Kay, C. N., Weinberg, D. V, Stepien, K. E., & Carroll, J. (2016). Assessing Photoreceptor Structure in Retinitis Pigmentosa and Usher Syndrome. *Investigative Ophthalmology & Visual Science*, *57*(6), 2428–2442.

Supriya, D., Shwetha, M., Kiran Anupama, K., Kummelil Mathew, K., Berendschot, T. T. J. M., Schouten, J. S. A. G., Bharamshetter, R., Naresh, Y. K., Rohit, S., & Hegde, B. (2015). Structural and Function Correlation of Cone Packing Utilizing Adaptive Optics and Microperimetry. *BioMed Research International*, *2015*, 968672.

Takayama, K., Ooto, S., Hangai, M., Ueda-Arakawa, N., Yoshida, S., Akagi, T., Ikeda, H. O., Nonaka, A., Hanebuchi, M., Inoue, T., & Yoshimura, N. (2013). High-resolution imaging of retinal nerve fiber bundles in glaucoma using adaptive optics scanning laser ophthalmoscopy. *American Journal of Ophthalmology*, *155*(5), 870–881.

Talcott, K. E., Ratnam, K., Sundquist, S. M., Lucero, A. S., Lujan, B. J., Tao, W., Porco, T. C., Roorda, A., & Duncan, J. L. (2011). Longitudinal study of cone photoreceptors during retinal degeneration and in response to ciliary neurotrophic factor treatment. *Investigative Ophthalmology and Visual Science*, *52*(5), 2219–2226.

Tam, J., Martin, J. A., & Roorda, A. (2010). Noninvasive visualization and analysis of parafoveal capillaries in humans. *Investigative Ophthalmology & Visual Science*, *51*(3), 1691–1698.

Tanna, P., Kasilian, M., Strauss, R., Tee, J., Kalitzeos, A., Tarima, S., Visotcky, A., Dubra, A., Carroll, J., & Michaelides, M. (2017). Reliability and Repeatability of Cone Density Measurements in Patients With Stargardt Disease and RPGR-Associated Retinopathy. *Investigative Ophthalmology & Visual Science*, *58*(9), 3608–3615.

Vilupuru, A. S., Rangaswamy, N. V, Frishman, L. J., Smith, E. L. 3rd, Harwerth, R. S., & Roorda, A. (2007). Adaptive optics scanning laser ophthalmoscopy for in vivo imaging of lamina cribrosa. *Journal of the Optical Society of America. A, Optics, Image Science, and Vision*, *24*(5), 1417–1425.

Wang, Y., Bensaid, N., Tiruveedhula, P., Ma, J., Ravikumar, S., & Roorda, A. (2019). Human foveal cone photoreceptor topography and its dependence on eye length. *ELife*, *8*.

Wells-Gray, E. M., Choi, S. S., Bries, A., & Doble, N. (2016). Variation in rod and cone density from the fovea to the mid-periphery in healthy human retinas using adaptive optics scanning laser ophthalmoscopy. *Eye (London, England)*, *30*(8), 1135–1143.

Xue, B., Choi, S. S., Doble, N., & Werner, J. S. (2007). Photoreceptor counting and montaging of en-face retinal images from an adaptive optics fundus camera. *J. Opt. Soc. Am. A*, *24*(5), 1364–1372.

Zayit-Soudry, S., Duncan, J. L., Syed, R., Menghini, M., & Roorda, A. J. (2013). Cone structure imaged with adaptive optics scanning laser ophthalmoscopy in eyes with nonneovascular age-related macular degeneration. *Investigative Ophthalmology and Visual Science*, *54*(12), 7498–7509.

Zayit-Soudry, S., Sippl-Swezey, N., Porco, T. C., Lynch, S. K., Syed, R., Ratnam, K., Menghini, M., Roorda, A. J., & Duncan, J. L. (2015). Repeatability of Cone Spacing Measures in Eyes With Inherited Retinal Degenerations. *Investigative Ophthalmology & Visual Science*, *56*(10), 6179–6189.

Zhang, T., Godara, P., Blanco, E. R., Griffin, R. L., Wang, X., Curcio, C. A., & Zhang, Y. (2015). Variability in Human Cone Topography Assessed by Adaptive Optics Scanning Laser Ophthalmoscopy. *American Journal of Ophthalmology*, *160*(2), 290-300.